

Injection and Ignition Characteristics of Gaseous Fuel Jets for Low-emission Engines

by
Hengameh Delbari

M.Sc., University of Tehran, 2013
B.Sc., University of Tehran, 2009

Thesis Submitted in Partial Fulfillment of the
Requirements for the Degree of
Master of Applied Science

in the
School of Sustainable Energy Engineering
Faculty of Applied Sciences

© Hengameh Delbari 2022
SIMON FRASER UNIVERSITY
Fall 2022

Copyright in this work is held by the author. Please ensure that any reproduction or re-use is done in accordance with the relevant national copyright legislation.

Declaration of Committee

Name: Hengameh Delbari
Degree: Master of Applied Science
Title: Injection and Ignition Characteristics of Gaseous Fuel Jets for Low-emission Engines

Committee: **Chair: Mina Xu**
Lecturer, Sustainable Energy Engineering

Gordon McTaggart-Cowan
Supervisor
Associate Professor, Sustainable Energy Engineering

Colin Copeland
Committee Member
Associate Professor, Sustainable Energy Engineering

Amir Shabani
Committee Member
Lecturer, Sustainable Energy Engineering

Mehran Ahmadi
Examiner
Lecturer, Sustainable Energy Engineering

Abstract

Application of renewable natural gas (RNG) and hydrogen (H₂) in internal combustion engines with a direct injection (DI) configuration leads to improved thermal efficiency and reduced CO₂. Because of the high nozzle pressure ratios (NPR) relevant to DI, typically an under-expanded jet is formed past the nozzle exit. Transient jet development affects ignition and combustion properties, and consequently performance and emissions of the engines significantly. In this research, the effects of parameters including injection pressure, gas type and composition, and back pressure on the characteristics of the gaseous jets have been experimentally investigated. The ignition properties of these jets have been studied using a hot surface. Results indicate that the NPR has the most significant effect on the jets' penetration rate. Additionally, adding H₂ to natural gas contributes considerably to improve ignition properties of the gaseous mixture. The results are of value to support future modeling and engine development.

Keywords: Clean Transportation, Renewable Natural Gas, Hydrogen, Direct Injection

Dedication

I would like to dedicate this work to my beloved husband, Soroush, for his love and support, and to my dear parents for tolerating our distance for my success and for all the sacrifices they have made, and to the brave women of Iran for their fights for freedom..

Acknowledgements

I would like to express my special gratitude to my supervisor, Dr. Gordon McTaggart-Cowan who was always supportive and provided invaluable supervision and feedback. I was honored to be his first graduate student and I truly enjoyed this journey with his generous provision of time and knowledge. I am also thankful for all the industrial exposure opportunities that my supervisor helped to occur through internships and within this project which provided me with valuable experiences.

I also have many thanks to my committee members, Dr. Amir Shabani, and Dr. Colin Copeland for sharing their knowledge, expertise, and support during this project.

I am also grateful to my lab mates for all their support throughout my research work. We have been developing a great team at the Vehicle and Engine Systems for Sustainable Transportation (VESST) research group at SFU that I am genuinely happy to be a member of.

During this project I had the pleasure of working with two co-op students, Jake and Harshaun, who helped to develop the experimental set-up. I also would like to acknowledge Mehdi's contribution in FE analysis of the optical chamber to ensure safe operation. I am grateful to Daneil, at SFU's machine shop for doing a great job in manufacturing the chamber, and Marius and Yifeng, the lab engineers who are always available to help students.

Table of Contents

Declaration of Committee	ii
Abstract.....	iii
Dedication	iv
Acknowledgements	v
Table of Contents.....	vi
List of Tables.....	viii
List of Figures.....	ix
Chapter 1. Introduction	1
1.1. Alternative Fuels for Cleaner Transportation.....	2
1.2. Direct Injection of Gaseous Fuels in IC Engines	4
1.3. Ignition of Gaseous Fuels with a Hot Surface Ignitor	5
1.4. Research Questions, Aim and Objectives.....	6
1.5. Thesis Structure	8
Chapter 2. Literature Review	10
2.1. Near-field Characteristics of the Jet.....	11
2.1.1. Mach Disk Location.....	13
2.2. Far-field Characteristics of the Jet	14
2.2.1. Axial Penetration.....	16
2.2.2. Radial Penetration and Cone Angle	19
2.3. Ignition of Gaseous Jets	21
Chapter 3. Experimental Methodology.....	30
3.1. Testing System Overview	30
3.2. Experimental Apparatus: Mechanical Set-up	32
3.2.1. Mechanical Components.....	34
3.2.2. Optical Chamber	37
3.3. Instrumentation, Data Acquisition and Control System	39
3.3.1. Instrumentations.....	40
3.3.2. Injection Drive System.....	41
3.4. Measurement Techniques	42
3.4.1. Visualization System: Schlieren Imaging Technique	42
3.4.2. Axial Penetration and Spread Angle Measurement	44
3.4.3. Mass Flow Rate Measurements	47
3.4.4. Nozzle Pressure Ratio Calculations	48
3.4.5. Velocity and Momentum Rate Calculations	50
3.5. Gas Blending Systems	51
3.6. Measurement Uncertainties.....	52
Chapter 4. Results and Discussions.....	53

4.1.	Argon-Helium injection Characteristics	55
4.1.1.	Injection Flow Characteristics.....	55
4.1.2.	Formation of Jets and Penetration Rate (Z_t).....	57
4.1.3.	Spread Angle	62
4.2.	Hydrogen-Methane Injection Characteristics	65
4.2.1.	Injection Flow Characteristics.....	65
4.2.2.	Formation of Jets and Penetration Rate (Z_t).....	68
4.2.3.	Effect of Back Pressure.....	75
4.2.4.	Spread Angle	78
4.3.	Characteristics of Jets Regarding NPR.....	81
4.4.	Gas Jets Momentum Rate Characteristics.....	82
4.5.	Ignition Characteristics of Hydrogen and Methane Jets	83
4.5.1.	Ignition of H_2 Jets	85
4.5.2.	Ignition of CH_4 Jets- Effect of Adding H_2 to Methane on Ignition.....	91
Chapter 5.	Conclusions, Limitations, and Future Work Recommendations	97
5.1.	Summary of the Research	97
5.2.	Conclusions and Implications	97
5.2.1.	Conclusions on Injection Characteristics	98
5.2.2.	Conclusions on Ignition Characteristics	99
5.2.3.	Implications for Engine Applications	100
5.3.	Research Limitations	101
5.4.	Future Work Recommendations	102
References.....	103
Appendix A: P&ID of the system.....	109
Appendix B: Electrical Drawing	110
Appendix C: MATLAB Code	111

List of Tables

Table 1-1- Hydrogen and Methane Properties	3
Table 2-1- summary and highlights of some of the research on gaseous injection characteristics	25
Table 3-1- Bosch NGI-2 injector technical specificatios	36
Table 3-2- Pressure sensors used in the system.....	40
Table 3-3- summary of calculated uncertainties	52
Table 4-1- Gas properties at different injection pressures	56
Table 4-2- Calculated parameters for different injection conditions.....	57
Table 4-3- specifications and calculated properties of H ₂ , CH ₄ and 46% blend (based on molar fraction of hydrogen)	66
Table 4-4- Calculated parameters for different injection conditions.....	67

List of Figures

Figure 1-1- Flow chart of the studied parameters	8
Figure 2-1- Under-expanded jet structure in the near field.....	12
Figure 2-2- Turbulent transient gas jet model.....	15
Figure 2-3- Definition of jets' measured parameters	16
Figure 3-1- Near-field and far-field structure of the jet obtained from the images.....	31
Figure 3-2- a) Air entrainment and mixing b) Ignition and flame propagation.....	32
Figure 3-3- Schematic drawing of the injection system.....	34
Figure 3-4- Injector and nozzle assembly a) injector connection to the nozzle b)the nozzle with 1mm hole diameter c) the injector connection to the nozzle through the injector block d) the injector block used in atmospheric tests e) the chamber used in tests with increased back pressure (and atmospheric back pressure)	37
Figure 3-5- injector, optical chamber, the ignitor (glow plug).....	39
Figure 3-6- Typical layout of a z-type Schlieren system.....	43
Figure 3-7- Concave mirror, camera, and the chamber	44
Figure 3-8- Detection of the front edge of the jet and measuring the distance from the nozzle tip for jets in different sizes.....	45
Figure 3-9- Measurement of the jet penetration using the camera software	46
Figure 3-10- Injector and nozzle assembly	48
Figure 4-1- Drawing of injector nozzle assembly	54
Figure 4-2- Development of He jet at 800 kPa(g) injection pressure.....	58
Figure 4-3- Ar penetration vs time	58
Figure 4-4- He penetration vs time	59
Figure 4-5- Ar-He blend (50% molar) penetration vs time.....	59
Figure 4-6- Penetration of Ar, He, and the 50% molar blend at 800 kPa (g) injection pressure.....	60
Figure 4-7- Plotting experimental data according to Equation 4-2 (Ar-He).....	62
Figure 4-8- Excluding the developing phase (the first 0.4 ms from the plotted data of Figure 4-7)	62
Figure 4-9- Spread angle of Ar, He and 50% on molar basis blend, obtained from the images	64
Figure 4-10- Spread angle of Ar, He and 50% molar blend at different injection pressures into the atmosphere at 90 mm penetration	64
Figure 4-11- Development of H ₂ jets at different injection pressures into the ambient pressure. The time intervals are after start of injection (ASOI).....	68
Figure 4-12- Methane jets at 2 ms after injection at 300, 500, and 800 kPa(g) injection pressure (numbers refer to the injection pressure)	69
Figure 4-13- H ₂ and CH ₄ jets evolution at 800 kPa(g) injection pressure	70

Figure 4-14- Size of the shock cells increasing in the developing phase (methane jets at 800 kPa(g) injection pressure)- the red labels show the observed length of expansion zone	71
Figure 4-15- H ₂ penetration vs time	72
Figure 4-16- CH ₄ penetration vs time	72
Figure 4-17- Plotting experimental data according to Equation 4-2 (H ₂ -CH ₄).....	73
Figure 4-18- Excluding irregularity in the first 10 frames from the experimental data	74
Figure 4-19- Ar, He, H ₂ , CH ₄ penetration at 800 KPa(g) injection pressure at ambient receiver pressure	75
Figure 4-20- H ₂ jet evolution with atmospheric, and increased back pressure	76
Figure 4-21- Penetration rate of H ₂ at atmospheric and increased back pressure (250 kPa(abs))	77
Figure 4-22- Plotting experimental data according to Equation 4-2 (H ₂ with increased BP- 250 kPa(abs))	78
Figure 4-23- Excluding the irregularity in the first 10 frames of the jets' development from the Figure 4-22.....	78
Figure 4-24- Spread angle of H ₂ , CH ₄ , and their blend with increased BP (250kPa(abs))	79
Figure 4-25- Spread angle of methane and hydrogen jets with (250 kPa(g)) and atmospheric BP.....	80
Figure 4-26- Effect of back pressure on the spread angle	81
Figure 4-27- Zt at 2 ms for all injection experiments versus NPR	82
Figure 4-28- Exit momentum rate of gases vs NPR in atmospheric and increased BP (250 kPa(g))	83
Figure 4-29- traveling jet and the position of the jet and the ignition source (a), traveling jet (b), start of combustion (c)- 10 frames after SOC (d).....	84
Figure 4-30- H ₂ jet traveling to the hot surface and sequences of the jet behaviour before ignition, at the start of combustion (SOC), and after ignition, for a jet injecting at 1000 kPa(g) and 250 kPa(g) back pressure	85
Figure 4-31- Ignition and flame propagation of hydrogen jets at 1200 kPa(g) injection pressure and atmospheric back pressure with 2.5 ms injection duration	86
Figure 4-32-H ₂ jet ignition with atmospheric and increased back pressure at 1200 kPa(g) injection pressure	88
Figure 4-33- Ignition delay of hydrogen over a range of injection pressures-atmospheric back pressure	89
Figure 4-34- Traveling time and chemical delay share in total ignition delay for hydrogen injection with atmospheric BP.....	90
Figure 4-35- Traveling time and chemical delay share in total ignition delay for hydrogen injection with BP.....	91
Figure 4-36- Methane jet impinging on the glow plug and not igniting	91
Figure 4-37- Ignition delay of hydrogen and the blend.....	92
Figure 4-38- Ignition delay of the blend with and without BP	93

Figure 4-39- Traveling time and chemical delay share in total ignition delay for H ₂ -CH ₄ blend injection with atmospheric BP	93
Figure 4-40- Traveling time and chemical delay share in total ignition delay for H ₂ -CH ₄ blend injection with increased BP	94
Figure 4-41- Ignition of the blend of hydrogen and methane with 1200 kPa(g) injection pressure and 250 kPa(g) back pressure.....	95
Figure 4-42- Mixing and chemical delay versus injection pressure for H ₂ and H ₂ -CH ₄ (20% E-46% molar) blend	96

Chapter 1. Introduction

Transportation, particularly freight transportation including heavy duty vehicles (HDV) class 2-7, and class 8, contributes significantly to greenhouse gas (GHG) emissions worldwide [1]. Despite substantial improvements in vehicles performance, inevitable expansion of transportation in the next decades and high dependency of transport freight vehicles on fossil fuels will likely result in increased GHG emissions from this sector in the near future.

Development of alternative fuels that have low greenhouse gas and other pollutants emissions are crucial to protect the environment and meet higher standards of air quality in this regard. Using gaseous fuels generated from renewable sources, including bio-derived renewable natural gas (RNG) and green hydrogen (hydrogen generated by renewable energy or from low-carbon power) offers significant near-term reductions in GHGs in the heavy-duty transportation sector using existing technology and available infrastructures. In some configurations such as high-pressure direct injection of natural gas, the generated GHG emissions can be reduced up to 20% compared to diesel engines while still using fossil natural gas. This amount can reach as high as 75% or more with renewable natural gas[2]. RNG is produced from organic materials or waste streams with lifecycle emissions lower than fossil natural gas. When burned in a vehicle, they produce similar emissions to NG, but the methane capture attributed to the upstream processes result in an overall reduction. Also, from an economic perspective, RNG is indicated as a low-carbon fuel which is commercially competitive with existing fossil fuel-based transportation fuels [3]. Hydrogen, on the other hand, not only has low or negative emissions depending on its production source, but also its addition to RNG in an internal combustion engine can boost its combustion characteristics [3].

Reducing carbon intensity of the transportation using gaseous fuels requires efficient combustion of such fuels in internal combustion engines. Studying the gaseous jet's physical properties including penetration and mixing, and their ignition properties play an important role in achieving higher efficiencies in using alternative fuels. The objectives of this study include injection and ignition characteristics of fuels comprising of hydrogen, natural gas, and their blends. In the current chapter, a brief introduction to the application of renewable gaseous fuels in internal combustion (IC) engines as the general context of

this study are given and the importance of studying gas jets in this regard is highlighted. Then, the goals and objectives of the research and the structure of the thesis are outlined.

1.1. Alternative Fuels for Cleaner Transportation

Compression ignition (CI) engines conventionally use diesel as their primary fuel. Although diesel engines have considerable advantages in terms of efficiency, adaptability, and reliability, their high GHG emissions and other pollutants including CO, and particulate matter (PM) cannot be overlooked [4]. Using natural gas (NG) as an alternative to diesel, results in considerably lower emissions. Natural gas, due to its high hydrogen to carbon ratio, offers 20-25% lower CO₂ per unit energy released, and low PM compared to diesel/gasoline if burned in an equally efficient engine[5]. Due to these benefits, numbers of vehicles operating on NG has been growing worldwide in the last decades. Natural gas powers more than 175,000 vehicles in the United States and roughly 23 million vehicles worldwide[6]. Although these numbers are not limited to the commercial vehicles, they show the significance of natural gas application in IC engines. This is specifically important in jurisdictions without access to low-cost clean electricity and high purity hydrogen.

On the other hand, application of H₂ (as a potentially zero-emission fuel) in internal combustion engines has been an interesting concept for decades [4]–[6]. Addition of H₂ to NG as a cleaner fuel alternative in the near term, can be considered as a bridge toward more usage of “Green hydrogen” in future [7][8][12]. Features of hydrogen can improve combustion properties, emission characteristics and thermal efficiencies of NG engines. For instance, H₂ has higher flame propagation speed, wider flammability range, and lower minimum ignition energy (MIE) which can improve natural gas ignition properties [11]. Some of the properties of hydrogen and methane are given in Table 1-1 [13].

Table 1-1- Hydrogen and Methane Properties

<i>Property</i>	<i>Hydrogen</i>	<i>Methane</i>
<i>Molecular weight (g/mol)</i>	2.016	16.043
<i>Density (kg/m³)</i>	0.08	0.65
<i>Minimum ignition energy (MJ)</i>	0.02	0.28
<i>Flammability limits in air (vol%)</i>	4-75	5-15
<i>Lower heating value (MJ/kg)</i>	120	50
<i>Auto ignition temperature (C)</i>	585	540
<i>Octane number</i>	≥130	125
<i>Flame speed (m/s)</i>	2.65–3.25	0.20-0.22

Another advantage of natural gas and hydrogen as fuels for IC engines relates to their excellent anti-knock properties. Knock in internal combustion engines is a term for inconsistent combustion of air fuel mixture in the unburned gases late in the combustion process which results in engine serious damages due to high frequency shocks in the cylinder. This abnormal combustion mode happens when combustion of the air/fuel mixture in the cylinder does not follow the propagation of the flame front. Fuels with lower octane numbers and lower auto ignition temperatures are more prone to knock in IC engines. Autoignition temperature of natural gas (585 °C) and hydrogen (540 °C) are high compared to diesel (210 °C) and gasoline (310 °C). Both natural gas and hydrogen, due to their high-octane number and high autoignition temperature have intrinsic resistance against knock. For hydrogen, very high flame speed gives it even higher resistance against inconsistent combustion and knock (Table 1-1). Although high auto-ignition temperature of natural gas gives it anti-knock properties, it creates the need for an ignition assist system to promote timely ignition and consistent combustion. Injection and ignition strategies of gaseous fuels vary in different engine designs. These strategies are briefly discussed in the following sections.

1.2. Direct Injection of Gaseous Fuels in IC Engines

Adopting a suitable injection strategy is important to prevent abnormal combustion modes and achieve higher efficiencies in engines. Direct injection of gaseous fuels is a promising approach that can improve the volumetric efficiency loss associated with port fuel injection (PFI). Reduced volumetric efficiency is a particular concern with H_2 due to its very low density (Table 1-1), where the displacement of air will lead directly to lower engine output power. In direct injection, the fuel is directly injected into the cylinder, either in early or late in the cycle. In DI, the volumetric efficiency is improved because the intake air is not displaced with fuel. Direct injection of gaseous fuels in the late cycle can offer similar or higher volume specific power compared to conventional diesel engines due to high compression ratio with fewer concerns about knock [14]. Direct injection in late cycle reduces the possibility of knock since there is not a premixed charge that to auto-ignite in the end gas during the combustion process. In summary, in late cycle DI of gaseous fuels including natural gas and hydrogen, knock, and abnormal combustion modes are reduced or removed [15], [16]. Therefore, the engine can operate on higher compression ratios (18:1 or higher) which results in higher thermal efficiency and higher power output.

In late-cycle direct injection, high injection pressures are required to overcome the elevated pressures in the cylinder. Higher injection pressures deliver more fuel in the same pulse width due to higher density of the injected fuel to provide enough energy for high load engine operations[17]. It also adds turbulent kinetic energy to the combustion chamber, increasing combustion rates. Applying high injection pressures leads to generation of turbulent under-expanded fuel jets past the nozzle exit [18]. The ratio of the injection pressure to the cylinder pressure is continuously changing but, in most cases, the range would be higher than the critical pressure ratio of gases to generate choked flow in all cases. These under-expanded jets travel within the cylinder and undergo mixing with the air. Depending on the ignition mechanism, they interact with the ignition source and get ignited. Characteristics of the discharged gas jets in terms of penetration and mixing, is really important for ensuring stable and repeatable ignition at the point of ignitor. Ignition needs to be stable and repeatable across an entire engine operating map, from idle (very short/low fuelling flow) to full load (long injection durations). Understanding gas jets at a basic level is critical to achieve this. Using alternative fuels in engines in this concept, requires deep understanding of the jet's physical characteristics and mixing properties in

various engine loads to design and configure the fueling and ignition systems. The different amounts of fuel contained in the jet are approximately from ~10 mg in cylinder for cycle at idle to as much as 340 mg in cylinder for cycle at full load for a typical commercial truck.

The characteristics will impact the quality of combustion, and consequently efficiency in the engines. Understanding the physical phenomena associated with the jets' structure, their penetration rate, and ignition properties are of crucial importance for optimizing fuel delivery and ignition processes in different engine working conditions[19].

1.3. Ignition of Gaseous Fuels with a Hot Surface Ignitor

Despite the benefits associated with alternative gaseous fuels, usage of these fuels in IC engines suffers from poor ignition properties. Following a successful fuel delivery process, there need to be a well-timed and rapid ignition event within the engine time scales. The injected fuel needs to be ignited and transitioned into a propagating burning jet leading to a consistent combustion. Although application of NG in IC engines can potentially reach diesel like efficiencies, achieving ignition in such engines is more challenging due to high resistance of natural gas to auto ignition in compression ignition engines [20]. Consequently, using NG as a fuel usually requires some form of ignition assist. There are a few approaches to ignite NG in a direct injection engine. These approaches include using a diesel pilot jet as an ignition assist (often termed as dual fuel) [21], spark plug[12], and hot surface ignitor [21]. A hot surface is usually a glow plug with the temperature range of 1200-1400 K to ignite natural gas. The required temperature for ignition of H₂ is less than NG due to lower minimum ignition energy required for hydrogen jets. Using a hot surface ignitor in a direct injection gaseous fueled engine provides the ignition energy to ignite the jet and transitioning the jet into a propagating flame. Using a hot surface with enough surface temperature provides continuous heat transfer to the injected fuel jet. Ignition assisted by a hot surface in a direct injection configuration of gaseous fueled engines can deliver equal or higher efficiencies compared to an equivalent diesel engine[21]. Hot surface removes the need for a second fuel in dual fuel systems and its advantage over the spark plug systems is that the careful optimization of the combustion system regarding the spark timing is not required. Only, the longevity and reliability of the hot surface materials needs to improve for holding high temperatures for extended periods.

1.4. Research Questions, Aim and Objectives

The aim of this research is to study the behaviour of gaseous jets in terms of injection and ignition processes. In this work, gas jet properties of non-combustible (Ar/He) and combustible gases (H₂/CH₄) as well as the ignition characteristics of the combustible fuels are studied with an experimental approach. The following questions are the research questions we are trying to answer:

- How do injection parameters including injection pressure and back pressure affect the gas jet characteristics?
- What would be the dependency of the jets' penetration rate on the gas properties?
- How ignition of the fuel will be affected by the gas type and composition and injection parameters?

To fulfill the aim of the research to investigate the injection and ignition properties of gaseous fuel jets, the following objectives are specified.

- *Testing system preparation, validation, and processing tools development to design and manufacture an experimental system to conduct injection and ignition assessments*
- *Characterization of the physical properties of free jets under various injection conditions through qualitative assessment of the injected gas jets by visualization and quantitative assessment of the jets' properties using the fundamental theories behind the jet movement*
- *Studying the effects of injection parameters on the ignitability of individual fuel jets of methane and hydrogen, and their mixture through qualitative and quantitative assessment of the ignition event and measuring the ignition delay under different conditions*

The first objective includes design, development and manufacturing an experimental facility and validation of the test system components and enhancements to the analysis and processing tools. The procedure involved automated processes and

employing high-speed recording to visualize and analyze injection and ignition events. The developed experimental facility enables injection and ignition characteristics of gas jets with different types and compositions. The second objective is to conduct characterizations based on visualization and imaging techniques at different injection pressures and different gas types and compositions with atmospheric or elevated back pressure. More specifically, the physical properties of interest include axial penetration rate, volumetric growth, jets flow rates, nozzle exit velocity, and jet force and momentum. To fulfill this objective, the model gases of argon (Ar), helium (He), and their blend, and combustible gases of methane (CH₄), hydrogen (H₂) and their blend are studied. Adapting model gases are used to ensure safe operation and to develop both measurement techniques and fundamental understanding of the injection process. The third objective includes studying the ignition properties of individual gas jets and their mixture in the tests conditions and defining the ignition delay dependency on injection and ignition parameters using a hot surface (glow plug). The dependency of the ignition delay on the injection pressure, and back pressure are defined in this step and the ignitability of the gas jets is investigated under various conditions with a focus on the effect of H₂ addition to methane on the ignition properties.

As discussed in the objectives, overall, the characterization of the gaseous jets in this project is divided into two parts: injection and ignition. The following flowchart (Figure 1-1) summarizes the parameters of the study to achieve the goals of the research:

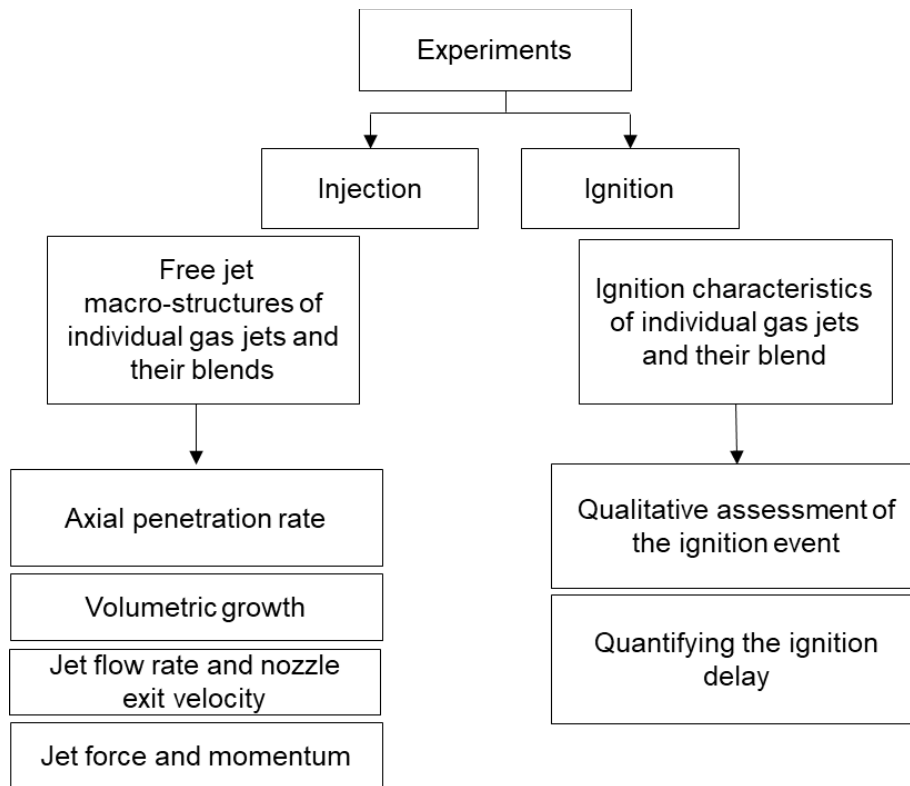


Figure 1-1- Flow chart of the studied parameters

1.5. Thesis Structure

This thesis is outlined in 5 chapters:

Chapter 1: Introduction

Chapter 2: Literature Review

Chapter 3: Experimental Methodology

Chapter 4: Results and Discussions

Chapter 5: Conclusion, Summary, and Future Work Recommendations

In the first chapter (the current chapter) an introduction is given to introduce the objectives, motivations, and the general context of the work to the reader. In the second chapter, related literature to the field of study is reviewed and the related theoretical background is discussed. In the third chapter, the experimental methodology detailing the systems and procedures is presented which includes systems development, measuring

techniques and characterization methods. The fourth chapter discusses injection and ignition characteristics evaluation; in particular, evaluation of the effects of the injection pressure, nozzle pressure ratio, and gas composition on the characteristics of the gas jets leaving the Injector using model gases (Ar and He) and combustible gases (H_2 and CH_4). Moreover, evaluation of the Ignitability of methane, hydrogen, and their blend as a function of defined injection and ignition parameters are discussed. Finally, the conclusions, summary, and future work recommendations are discussed in the fifth chapter.

Chapter 2. Literature Review

As stated in the Introduction chapter, gaseous-fueled vehicles can reduce the overall carbon footprint of the commercial freight significantly. Direct injection (DI) of gaseous fuels is particularly beneficial to increase the efficiency of such engines and reduce concerns regarding abnormal combustion. However, direct injection application of gaseous fuels including natural gas and hydrogen requires understanding the physical phenomena associated with the jets' structure, their penetration rate, and ignition properties for optimizing fuel delivery and ignition processes in different engine working conditions. In particular, hydrogen and the blends of hydrogen and renewable natural gas are concepts that require further investigations to use in internal combustion engines. Gas jets characteristics are associated with fundamental fluid mechanic and thermodynamic properties that help to interpret and understand the behaviour and structure of the gas jets. In addition to the fundamental studies that date back to decades ago, in numerous studies experimental and numerical approaches are taken to develop an understanding of jets' behaviour in various physical conditions. This chapter reviews the literature in the area of study with more focus on the fundamentals of the gas jet dynamics, supporting theories and gas jet characteristics.

Direct injection technology involves injection of gaseous fuels at high pressures to overcome elevated pressures inside the cylinder. In such high-pressure conditions, a compressible fluid flowing through a convergent nozzle can accelerate to supersonic velocity and reach choking conditions. The flow of the jet under such conditions become under-expanded and a series of shock waves appear on the after the nozzle exit. The structure and dynamics of the gaseous jets are typically categorized as near-field characteristics and far-field properties. Near-field characteristics include more complex phenomena in the areas closer to the nozzle where the jet is developing, and far-field properties include assessment of the macro-characteristics of the jet further downstream of the flow where the jet is fully developed. These properties are outlined in the next sections.

2.1. Near-field Characteristics of the Jet

To investigate the structure of the jet, its properties can be categorized as far-field characteristics and near-field properties. The near field will include complex phenomena taking place in the core area at distances equal to a few nozzle diameters downstream of the nozzle exit plane. In a typical multi-hole inward-opening direct injector, When the injector starts to open (In the internal geometry of a nozzle there is a needle that lifts up upon receiving current), a sac volume inside the injector starts to fill with the gas, leading the gas to the exit through its holes. The seat area in the injector is much larger than the nozzle hole diameter, and the pressure in the sac rapidly approaches the upstream pressure during the injection event. When the pressure ratio over the nozzle is greater than the critical pressure ratio, the gas reaches the speed of sound at the exit of the converging nozzle and a complex structure after the exit start to form (Figure 2-1). The Mach number (Equation 2-1) at this point equals 1 and the velocity of the gas equals the speed of sound.

$$Mach = \frac{V}{V_{(sound)}} \quad \text{Equation 2-1}$$

At the exit, the flow starts to expand and because of the sudden pressure drop, the velocity of the gas increases. However, the flow gets constrained at the edges in the form of expansion waves which prevent the local pressure in the gas jet from dropping immediately to the same pressure as the surroundings [19]. Resistance of the expansion waves to the boundary of the flow makes barrel-shaped compression waves followed by a Mach disk at the leading edges of the cell. The location of the Mach disk and its distance from the nozzle tip is called the Mach disk height. Another important parameter that affects the flow is the Mach disk width (W). Mach disk information provides significant knowledge of effective upstream pressure of the gas jet. The increase in Mach disk width provides stronger turbulence intensity in the jet and improves turbulent mixing effect in the downstream[22]. At the Mach disk the flow reaches sonic conditions but within the shock cells the flow will be supersonic. Multiple shock cells can form depending on the level of under-expansion. Higher pressure ratio results in higher number of shock cells which means the pressure is decreasing to the surrounding pressure in a series of steps. Under these conditions, Reynolds number is high enough to consider the flow fully turbulent. A schematic of the flow in the near nozzle area is shown in Figure 2-1 [23].

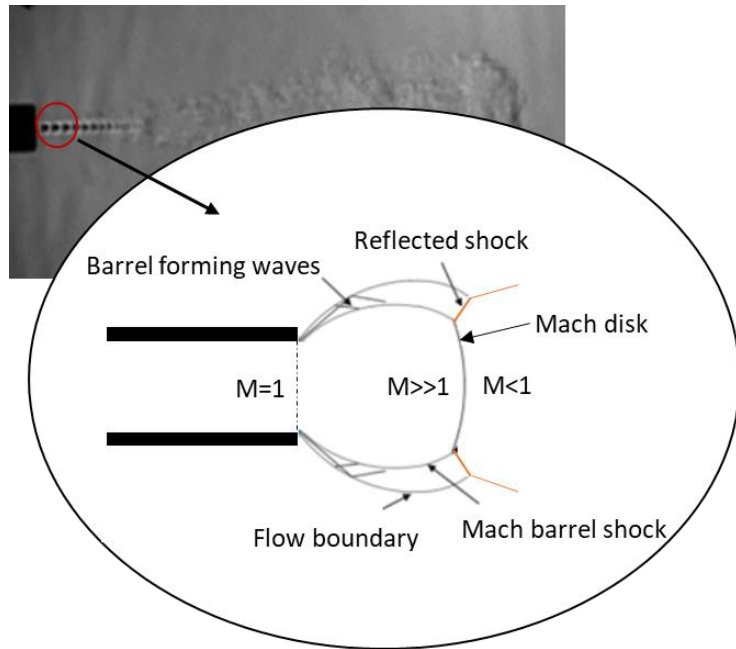


Figure 2-1- Under-expanded jet structure in the near field, the upper image is taken during the experimental measurement campaign and the lower image is reproduced from [23]

In the near field, length, and number of the shock cells, and location and dimensions of the Mach disk are among the important parameters affecting the far-field properties of the jet and its mixing with the surrounding air [24]. For example, an increase in the Mach disk width leads to a larger spread angle that promotes the spatial spread and turbulent mixing of the jet[18].

In direct injection of gaseous fuels, especially in direct injection late in the cycle, the injection pressures should be quite high to overcome the high in-cylinder pressure and to deliver sufficient amounts of fuel into the cylinder for every engine condition. For direct injection of natural gas in compression ignition (CI) engines, injection pressures between 20-30 MPa are typically required to overcome elevated pressures in the chamber and to ensure enough fuel injection in each load[1] [2]. The in-cylinder pressure during the injection process can exceed 10 MPa at high loads in a boosted high compression ratio engine. In such engines, natural gas is injected late during the compression stroke through multi-hole nozzles. High injection pressures in direct injection of NG most likely leads to nozzle pressure ratios greater than the critical pressure ratio which result in generation of under-expanded jets. Under most conditions, the flow of the gas jet will be choked with

sonic conditions at the nozzle exit. For development of gaseous fuel DI engines, accurate understanding of the dynamics of the fuel jet flow and its effect on the air/fuel mixing processes in each injection and in-cylinder thermodynamic conditions are required.

Supersonic jets are generally classified as moderately under-expanded jets and strongly under-expanded jets depending on the value of their nozzle pressure ratio (NPR). For $NPR \geq 2$, the jets are classified as moderately under-expanded. Due to the large differential in pressure, velocity and density between the injected gas and surrounding media, the formation of oblique shock cells occurs, and the shock lines converge toward the jet's axis. Combination of these shock waves forms a barrel-shaped region of supersonic flow, with a Mach disc at the leading edge. For strongly under-expanded jets ($NPR \geq 4$), the same phenomenon exist with more severity with higher number of shock cells and longer core of the jet [19].

2.1.1. Mach Disk Location

Reflection of the expansion fans from the jet boundary creates intercepting shocks which are completed by the Mach disk making the first shock cell. high complexity of the near-nozzle area can be governed by the gas dynamics conservation equations that connect the upstream conditions to the downstream of the jet. Basically, each cell acts as a diverging-converging nozzle (velocity drops and then increases again, until it reaches $Ma = 1$). Understanding these structures and their characteristics, such as the dimensions and the location of the Mach disk, have been the subject of many studies [18], [19], [23], [27], [28]. The dimensions of a Mach disk in under-expanded jets are known as Mach disk height (H_{disk}) and Mach disk width (W_{disk}) which are the distance from the nozzle exit to the disk and the distance of the two triple points respectively [18]. These information in the near field region of an under-expanded jet can be utilized to estimate the mixing and flow characteristics of the jet.

The location and dimensions of the Mach disk can be estimated by numerical and experimental methods[29]. In a study by Yu et al.[30] dimensions of the Mach disk has been calculated numerically and experimentally. In another study by Allocca [19], the location of the Mach disk has been evaluated and compared by Schlieren visualization and large eddy simulation (LES) numerical method. Although there are some differences in the initial stage of forming the Mach disk, overall, the model agrees with the

experimental results on the location of the fully developed Mach disk. The reason that the height of the Mach disk increases in the beginning is that there are some delays regarding the needle lift in the injector and pressure build up in the nozzle. Once the flow is developed the location of the Mach disk is stabilized. In the early stages of developing the Mach disk, its location moves a bit further from the nozzle, but it stabilizes once the jet is developed. For a fully developed Mach disk, the location of the disk, or the barrel length, is given by the below equation, relating this parameter to the nozzle diameter (d), and the nozzle pressure ratio ($\frac{p_0}{p_a}$) [18]:

$$\frac{H_{disk}}{d} = C_x \sqrt{\frac{p_0}{p_a}} \quad \text{Equation 2-2}$$

Where the range for the constant C_x in the literature is about 0.60 to 0.67 [29]–[31]. In this correlation it is assumed that the flow is choked at the nozzle exit ($Ma=1$). Application of this equation has been validated in different pressure ratio ranges from round nozzles in different studies [14]. According to this equation, the location of the Mach disk is not dependent on the gas properties. However, nozzle pressure ratio and nozzle diameter are the main factors affecting this parameter. Multiple studies have shown that the Mach disk height can be used to determine the nozzle outlet pressure. Using Equation 5 and by measuring the Mach disk through experimental and numerical approaches, Allocca et al. [19] calculated the actual pressure of the nozzle upstream of the jet. In another study by Dong et al, also this approach is validated using numerical and experimental findings [22]. However, in case of using visualization techniques, the resolution of the images should be high enough to measure the Mach disk height with accuracy.

2.2. Far-field Characteristics of the Jet

As the jet penetrates further and starts developing, the air entrains into the body of the jet along the periphery. The entrained air mixes with the fuel as the gas jet injection ends and a combustible air/fuel mixture start to form. To describe the physical structure of the jet after it has expanded, Turner suggested a model in 1962 [32] for fully developed turbulent transient jets. This model has been widely accepted and used ever since [17]. In his model, Turner proposed that the jet is composed of two parts; a vortex head, and a steady state region which feeds mass and momentum to the head [33]. The traveling

vortex has spherical shape with internal rotational momentum in the head. The vortex head penetrates according to its momentum and decelerates due to frictional losses with the surrounding environment. The vortex head is continuously fed with mass and momentum from the jet and displays steady state behaviour within its region as long as the nozzle exit flow is steady. Mixing with the surrounding fluid mostly takes place in the quasi-steady part and not in the vortex region. As the jet travels, it slows down because of the friction and drag forces, entraining the surrounding fluid, and volumetric growth and radial penetration. A schematic of Turner model is shown in Figure 2-2 [34].

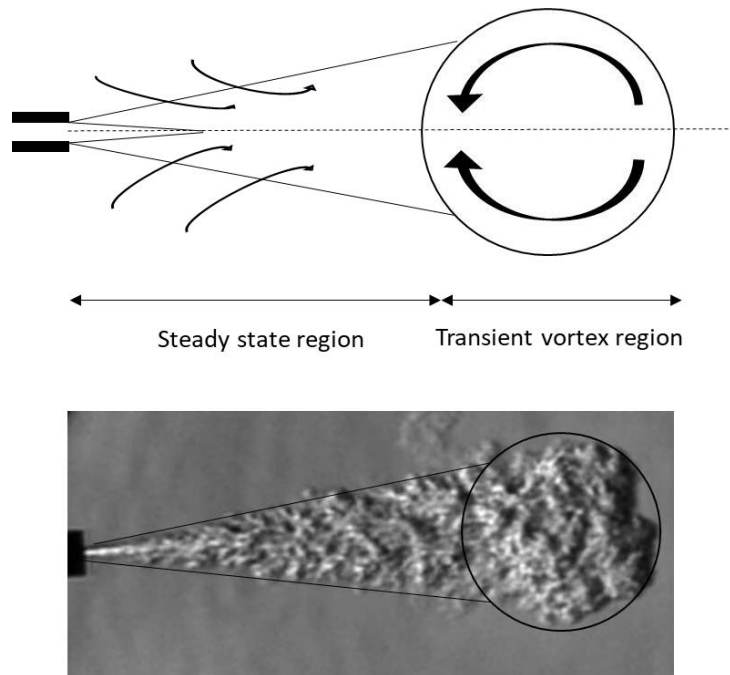


Figure 2-2- Turbulent transient gas jet model (upper image regenerated from the Turner's model [32], the lower image is taken during the experimental measurement campaign)

Far field characteristics include the axial and radial penetration and growth angle of the jet. A fundamental understanding of the under-expansion process and the characteristics of the jet at the exit and further away from the nozzle is necessary to design efficient injection and ignition systems. Several researchers have employed experimental and modeling methods to study the characteristics of under-expanded free jets. Some of the most relevant of these studies are reviewed in this section.

2.2.1. Axial Penetration

Jet tip penetration is one of the key parameters of the jet affecting air-fuel mixing in DI engines. Penetration of the jet defines how far it travels in a few milliseconds and how long it takes for the jet to reach the ignition source, piston, and chamber walls. Also, the penetration of the free jet and its behaviour as an impinging jet is relevant to its mixing and ignitability properties which are of significant importance when it comes to engine design and optimization. The tip penetration is defined as the position of the jet tip as it develops over the course of injection. In addition to the jet tip penetration, cone angle and Mach disk width are also among the parameters that are of interest to evaluate in jets' studies. Figure 2-3 shows these parameters on a jet structure [19].

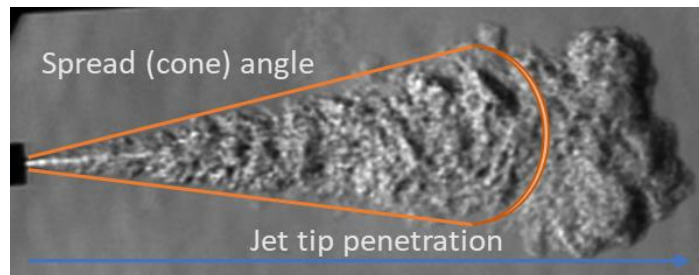


Figure 2-3- Definition of jets' measured parameters (image is taken during the experimental measurement campaign)

Penetration rate has been measured in different studies and its dependency on the injection parameters has been identified. Many experimental and numerical observations have established the linear dependency of the transient turbulent jets' penetration on the square root of time [18], [33], [35], [36]. Turbulent transient jets are typically under-expanded as their pressure ratio is normally greater than the critical pressure ratio and the flow velocity is sonic at the exit. Such jets also show self similarity with the ratio of their maximum width (D) to their penetration length (Z_i) at each point. This ratio is found to reach a constant value after distances greater than 10-15 nozzle diameters and after that the jet just scales up with the constant ratio of D/Z . This behaviour is called self similarity and is a useful concept in jets characterizations.

Similarity length scale (d_{eq}) and time scale (t_{eq}) are equal to:

$$d_{eq} = d_n (\rho_n / \rho_{ch})^{1/2} \quad \text{Equation 2-3}$$

$$t_{eq} = (t U_n / d_{eq})^{1/2} \quad \text{Equation 2-4}$$

Where ρ_n is the density of the gas, ρ_{ch} is the density of the chamber, U_n is the nozzle velocity, d_n is the nozzle diameter, and t is the time.

Hill and Ouellette [35] used the self-similarity observation along with the momentum conservation and established a relationship for the penetration of transient turbulent jets expressed by Equation 2-5. The total exit momentum flow rate of the jet is considered to be the only significant characteristics of the flow. Similarly, the chamber density is the only fluid specification of the chamber fluid.

$$z'_t = \Gamma \left(\frac{\dot{M}_n}{\rho_{ch}} \right)^{1/4} t^{1/2} \quad \text{Equation 2-5}$$

Where Γ is a constant with the approximate value of 2.8-3.1 for turbulent jets exiting from round nozzles [16]. \dot{M}_n is the injection momentum rate at the exit of the nozzle, and ρ_{ch} is the density of the surrounding fluid in the chamber. This Equation has a wide range of applicability and is valid for turbulent compressible or incompressible free jets (no wall contact) for distances greater than 20 d_{eq} and Reynolds numbers at the nozzle exit be greater than 5×10^4 . Some other conditions of this equation include constant injection mass flow rate, and the time intervals being smaller than the injection time.

Using the similarity length and time scales, Equation 3 can be transformed to the following form which is often cited in the literature [34], [36], [37].

$$\frac{z_t}{d_{eq}} = \Gamma \left(\frac{\pi}{4} \right)^{1/4} \left(\frac{t U_n}{d_{eq}} \right)^{1/2} \quad \text{Equation 2-6}$$

Where U_n is the velocity of the gas at the nozzle. Other parameters of this equation have been defined earlier.

Equation 2-5 expresses that the penetration is not directly dependent on the injection pressure, velocity, or nozzle diameter. But it has a direct dependency on the momentum rate at the exit of the nozzle. However, the momentum rate itself depends on the density and velocity of the jet discharging from the nozzle. It means higher nozzle exit density, higher velocity, and larger nozzle diameter leads to a higher penetration rate. If

the injection pressure remains unchanged and the density of the surrounding (the chamber pressure) increases, there would be more resistance against the jet propagation and the penetration rate decreases. As the chamber pressure increases while the injection pressure is constant, the nozzle pressure ratio (NPR; the ratio of the total upstream pressure to chamber pressure) decreases. If the nozzle pressure ratio eventually falls below the critical pressure ratio, the flow is not choked anymore, and the momentum will decrease. Until that point, the jet momentum rate stays constant.

To study the structure and dynamics of the jets, experimental and numerical approaches, or a combination of them have been taken in the literature. In a study by Allocca et al. [19] methane jets were studied using both numerical and experimental approaches. In this study, under-expanded jets were injected into an optically accessible constant volume chamber through a single-hole commercial injector at pressures up to 1.2 MPa. Schlieren imaging technique has been used to visualize the gas jets and evaluate gas jet penetration, Mach disk position, and the spread (cone) angle. The analysis of the schlieren images revealed that the jets' structure follows three patterns of subsonic, moderately under-expanded, and highly under-expanded depending on the nozzle pressure ratio. Also, it was shown that higher injection pressure led to an increase in penetration rate and an increase in the maximum Mach disk height. However, the jet cone angle did not seem to be affected much by the injection pressure. In another research employing schlieren imaging technique, Dong et al [22], investigated the evolution of shock wave structure in high-pressure injection of gases. Their experimental and numerical approach concluded that high gas injection pressure and large orifice diameter increases the mass flow rate of the fuel at the nozzle exit. Increased mass flow rate allows shorter pulse widths to deliver enough fuel and obtain a homogeneous mixture.

Overall, the geometry of the injector and the nozzle significantly impact the characteristics of the flow. In particular, the effects of the injector geometry and response of the injector needle can significantly impact the gas jet dynamics. Effects of the nozzle hole geometry on the gas development have been studied by Li et al. [27] using computational fluid dynamics (CFD) with large-eddy simulation (LES). In this study, nozzles with different geometries were used at the same injection conditions. Results indicate that the gas jets issued from square jets penetrate faster, although the penetration rate of the jets from four different geometries all follow the linear dependency on the square root of time. Moreover, jets issuing from different nozzles show different mixing

properties. In another study by Vera-Tudela et al [24], the needle dynamics of a prototype gas injector (a single hole axial injector) under different working conditions were evaluated. In two different sets of experiments, the effects of the injection pressure and duration, chamber pressure and pressure ratio were examined on the jet properties. In this study, Schlieren technique was employed using a high-speed camera to visualize the propagation of methane in a constant volume optical chamber. The results showed a strong dependency of the needle dynamics on the injection pressure. However, this dependency becomes less noticeable at higher injection pressures. The chamber pressure seemed to have small effect on the needle dynamics. Also, at constant pressure ratio, higher injection pressure resulted in faster needle opening time, while the penetration rate remained unchanged. This further indicates that the dominant factor affecting the penetration rate is the nozzle pressure ratio. In another study, Chitsaz et al. [16] investigated the effect of the pressure ratio and nozzle diameter on the penetration length and jet structure of injected helium at high pressure ratios. They found that higher pressure ratio and wider nozzle diameter, result in higher penetration rate. In this study, for the first millisecond of the jet propagation, the numerical results were not completely in agreement with the experimental data which could be due to the transient effects of the needle lift within the injector tip. In another study, on the effect of the nozzle diameter, Mansor et al. [38] concluded that higher injection pressure and larger nozzle diameter result in faster jet development and larger jet spread angle with tests on hydrogen jets in an Argon-oxygen environment.

To characterize the gaseous jets properties, there are several studies that employ numerical approaches[8], [10], [20], [23]–[25]. For instance, using a numerical approach consisting of a hybrid, pressure-based solver combined with a vapor-liquid equilibrium model, Banholzer et al [28] studied under-expanded methane jets by a moving mesh methodology. Lower chamber pressures led to faster jet penetrations due to the reduced densities which is consistent with Equation 1. Since the focus of this research is on the experimental approaches, the literature discussing numerical approaches is not reviewed in detail. However, some of such research are summarized in Table 2-1.

2.2.2. Radial Penetration and Cone Angle

Another important parameter that affects the air-fuel mixing and mixture formation is the volumetric growth or the cone angle. Gaseous jets issuing from round nozzles or

inward opening injectors (these injectors have nozzle-like holes that the gas comes out) spread in the form of a cone having a well-defined angle. Measured values of the jet angles have shown values between 14 to 40 degrees [41]. The jets' spread angles are dependent on the nozzle size and configuration and whether the jet is fully developed or is in the initial stages of development.

Cone angle has direct relevance to the radial penetration of the gas jets. The radial (or lateral) penetration is defined as the diameter of the jet or the jet radial penetration width (D). In a study by Hajjalimohammadi et al. [39] the ratio of the jets diameter to its penetration length (D/z) has been measured using Schlieren visualization technique and image processing for He issuing from nozzles with different diameters. Experimental and numerical findings showed that the nozzle pressure ratio did not have a distinctive effect on radial expansion when normalized by axial penetration. The value of D/z for transient jets decreased by time at the beginning of the jet evolution but reached a constant value of 0.33 ± 0.05 as the jet reaches its fully developed phase. This constant value in a study by Ouellette et al was obtained 0.25 ± 0.05 for the fully developed gaseous jets [33]. In the first millisecond of the jet development, the flow rate and axial penetration of the jet is affected by the motion of the needle, therefore the ratio of the radial to axial penetration is low [42]. Once the jet reaches the fully developed phase, the jet becomes self-similar, and the ratio of D/z becomes constant. From that point, the size of the jet just scales up with a consistent diameter to length ratio which is useful to predict its dimensions in further distances [39]). In another study by Rogers et al. [23] the average jet angle for CNG jets has been experimentally measured, and the jets angle on different phases of the jets development were defined. In the early development, the average angle of CNG jets is high but it gets narrower as it develops which originates from the relatively large size of the nozzle (3.8 mm). In this study also a comparison between the CNG and H_2 jets show that the hydrogen jets penetrate slightly wider than the methane jets. An important outcome of the spread angle evaluation in this research is that once the self-similar development is achieved, the jets reach a consistent spread angle.

To evaluate the effects of the elevated chamber pressure on the radial penetration (and therefore on the cone angle) Hamzehloo et al.[18] evaluated hydrogen jets with a numerical approach with the same NPR but different chamber pressures. The results showed slightly larger radial penetration in elevated pressures as a result of decreased axial penetration under choked flow conditions. In a study [43] , a numerical investigation

showed a wider cone angle and bulkier jet for hydrogen compared to methane at the same NPR. Deng et al.[44] studied the injection and mixing characteristics of high-pressure hydrogen and oxygen jets in an argon environment and determined that the dispersion angle of the jets increases slightly as the injection pressure increases which originates from the higher momentum at the nozzle exit due to higher upstream density. This enhances the entrainment of the surrounding gas into the jet and improves mixing properties. The cone angles of hydrogen jets were obtained between 31 to 36 degrees in their experiments. In the study by Hamzehloo [31] a comparison between hydrogen and methane jets through numerical investigation resulted that the hydrogen jets due to higher diffusivity, have wider spread angle compared to methane jets at the same NPR. Also, for hydrogen jets, mixing started earlier around the shock cells area, which is a result of the wider angle, while for methane jets, there was not much mixing with the air seen around the core area. However, for both methane and hydrogen jets, mixing started more after the Mach disk location, close to the boundaries of the jet.

2.3. Ignition of Gaseous Jets

Application of natural gas, as the main available gaseous fuel is well developed in spark ignition (SI) engines. However, gaseous fueled SI engines suffer from lower power output compared to their gasoline counterparts due to air displacement [45]. On the other hand, application of NG in compression ignition (CI) engines is still under development. Compared to diesel, NG is harder to use in a CI engine due to its high auto-ignition temperature (low cetane number). In order to auto-ignite NG, temperature needs to be greater than 1100-1200 K which requires much higher compression ratios in a CI engine, such as the ratio of 23:1 or higher [45]. This ultra high compression ratios lead to extremely high in-cylinder pressure which pushes the physical boundaries of the engine strength and limits maximum achievable power output from the engine. Also, the high temperature will affect the performance and emissions of the engine adversely. Consequently, an ignition assistance is usually required to ignite NG gas in a compression ignition engine.

There are three main methods to ignite natural gas in CI engines:

- 1- Dual fuel: in this approach natural gas is injected into the manifold and mix with the air to enter the cylinder. Then the mixture is ignited following the ignition of the injected diesel through the compression stroke[46], [47].

- 2- High Pressure Direct Injection (HPDI): in this approach NG is injected directly into the cylinder with high pressure late in the compression stroke. To assist with the ignition of natural gas in this case, a pilot diesel fuel jet is also injected into the cylinder. This system has been developed at the University of British Columbia and have been commercialized by Westport Fuel Systems Inc. [26], [48]. The Westport HPDI system injects both fuels directly into the cylinder late in the compression stroke from the custom two fuel high pressure injector.
- 3- Hot-surface Ignition Assist: in this method, a hot surface is located in the vicinity of the directly injected gas jet into the cylinder. The hot surface is a glow plug with the temperature range of 1100K to 1400K [49]–[51]. If implemented correctly, using a hot surface as an ignition assist can promote high performances and remove the complexity and cost of high-pressure dual fuel systems. Ignition delay is sensitive to the temperature of the plug and the position of the jet compared to the hot surface. The glow plug needs to have high enough temperatures for a timely ignition and the gaseous fuel jet should be in proper contact with the hot surface to initiate a consistent ignition event with low ignition delay [49].

Non-premixed combustion of directly injected NG can offer diesel like performance and efficiency. Using a hot surface as the ignition assist for NG ignition removes the limitations and requirements associated with dual fuel systems. Although approaches to ignite gaseous fuels are mentioned mostly for the injection and ignition of natural gas in the literature, this could be applied to hydrogen (or other gaseous fuels) in internal combustion engines as well. Similar to NG, hydrogen can be injected in the manifold or directly into the cylinder. However, the ignition characteristics of hydrogen are different with NG. Hydrogen is more ignitable than natural gas and is more resistant against knock. In fact, ignition properties of hydrogen are superior compared to NG and addition of hydrogen can improve ignition properties of natural gas in engines [17].

For a successful ignition event to happen using a hot surface, three consequent steps should be completed in a timely manner. First the gas needs to be transferred to the vicinity of the hot surface by its momentum as a free jet. It is important that the fuel get mixed with the air and make a combustible mixture at the right position against the hot surface. These two steps include the physical processes involved. Then at the final step,

the kinetic reactions need to take place to dissociate the fuel/ air molecules and initiate the exothermic reactions. Appropriate flame propagation is required to spread the flame for a complete and successful combustion event [51].

The ignition characteristics of gaseous fuels including natural gas and hydrogen have been studied in several researches[40], [46], [49], [51]. Effects of hydrogen addition on reducing ignition delay of natural gas have been shown in numerous studies[52]–[54]. In a study by Nguyen [55], the ignition characteristics of NG and H₂ jets in a direct injection diesel engine conditions using a high pressure solenoid-type single-shot gas injector have been studied. The experiments were conducted in a constant volume chamber with varying injection parameters and different pressures and temperatures. Results indicate that hydrogen shows shorter ignition delays and faster kinetics compared to NG. In addition, the nozzle hole diameter and injection pressure found to be affecting the ignition delay of hydrogen, however, their effect on the ignitability of NG jets were not significant. In this study, ignition delay is defined as the time from the start of injection until the net rate of pressure rise exceeds a certain threshold level in the chamber. Using hot surface for ignition of hydrogen, Mevel et al [56] characterized the ignition of hydrogen-air mixtures with regard to the surface temperature and the location of the ignitor. Results indicate that even the heating rate affect the mixing formation around the ignitor which affects the location in which the ignition starts around the hot surface. Therefore, a hot surface with well defined properties is required to enable precise characterization of ignition dynamics. In a study by McTaggart-Cowan [57], the effects of the gaseous fuel composition on non-premixed combustion of natural gas and hydrogen were experimentally investigated. The results concluded that the effects of hydrogen addition on ignition delay is varied according to the dominated ignition mechanism. When ignition is dominated by chemical kinetic concerns, the addition of hydrogen to natural gas reduces the ignition delay while when the ignition is limited by mixing, the effect of hydrogen addition is negligible.

The geometry of the injector and the glow plug is known to affect the ignition delay significantly. In a study by Gogolev [58], the direct injection of NG with glow plug ignition assist have been implemented in a single-cylinder compression-ignition optical research engine and the effects of the injector and glow plug geometry on the ignition quality have been examined. The results show the significant effect of the injector angle with the shield angle on the ignition delay. Ignition delay was measured to be in the range of 1.6–2.0 ms. Higher intake pressure seemed to increase ignition delay due to the effect of swirl

momentum on the fuel jet development and air entrainment. Aligned with these findings, a numerical study by Oprea et al. [59] shows that placing a shroud around the hot surface reduces the velocity of the impinging jet on the surface and increases the residence time which results in reducing the ignition delay. Regarding the contact of the jet with the hot surface, it is also important to avoid excessive impingement of the jet on the surface due to increased cooling of the surface which can increase the ignition delay and degrade the hot surface in a faster pace [51].

Table 2-1 summarizes some of the research studies in the field of injection of gaseous fuels in the recent years. From the discussed literature review, it is concluded that studying the structure of the jets is of great importance for further applications of the gaseous jets in engines. The structure of the jet in the beginning of its evolution defines the further behaviour of air/fuel mixing and ignition. On the basis of the literature and to answer the research questions regarding the effect of the injection parameters and gas type and composition on the injection and ignition characteristics, the research methodology is defined and detailed in the next chapter. This work's novelty is in linking the injection parameters to ignition properties in the same configuration. Studying the injection-ignition characteristics simultaneously enables direct connection between the physical properties of the jets including penetration length and spread angle to the ignition behaviour of the combustible gas jets. Extending this approach to various gas types and compositions brings a new perspective to investigate the physical properties, air mixing, and ignitability of the fuel jets. The impacts of the ratio of pressures between the upstream pressure of the gas in the nozzle and the receiver (nozzle pressure ratio, NPR), is a factor that would be expected to significantly impact jet dynamics and ignition which did not appear in the reviewed literature

Table 2-1- summary and highlights of some of the research on gaseous injection characteristics

No	Title	Year	Highlights	Ref
1	Under-Expanded Gaseous Jets Characterization for Application in Direct Injection Engines	2020	<p>The analysis of the schlieren images revealed three phases of subsonic, moderately under-expanded, and highly under-expanded characteristics for the jets with transient nature.</p> <p>Higher injection pressure increased the penetration and the Mach disk height of the jets</p> <p>The pressure in the upstream of the nozzle has an established relationship with the Mach disk height</p> <p>Numerical model provides more data in the near-field that is not obtainable from schlieren images</p>	[60]
2	An experimental and numerical study of natural gas jets for direct injection internal combustion engines	2020	<p>Experimental and numerical study was done on transient CNG jet flow from outward opening nozzles to predict the jet growth for different nozzle geometries and their effect on the jet characteristics such as mass flow rate, penetration and mixing</p> <p>Wider nozzle angle with a more diverging shape of the nozzle results in higher mass flow rate due to larger effective flow area</p>	[61]
3	Experimental study on jet ignition and combustion processes of natural gas	2020	<p>The impacts of pre-chamber geometric parameters and premixed gas parameters on ignition and the consequent combustion processes were investigated with optical diagnostics in combination with pressure acquisition in a constant volume chamber</p>	[62]

4	LES and RANS modelling of under-expanded jets with application to gaseous fuel direct injection for advanced propulsion systems	2019	An OpenFoam solver was developed with Runge-Kutta temporal discretization and was validated for the study of under-expanded jets The models were employed to study under-expanded jets issued through millimeter-size nozzles for applications in high-pressure direct-injection (DI) gaseous-fueled propulsion systems	[63] [63]
5	Numerical investigation of the flow characteristics of under-expanded methane jets	2019	Numerical simulations were carried out to investigate under-expanded methane jets with phase separation effects In order to predict the fuel injection and the mixture formation in the constant volume chamber, a hybrid, pressure-based solver was combined with a vapor-liquid equilibrium model and a moving mesh methodology	[64] [65]
6	Modeling and Analytical Solution of Near-Field Entrainment in Suddenly Started Turbulent Jets	2019		[66]
7	An experimental study on the effects of needle dynamics on the penetration of a high-pressure methane jet	2019	The aim of this work is to investigate the needle dynamics of a prototype gas injector under different working conditions Two experimental matrices were designed to Study of the consequences that these effects would have on the	[67]

			propagation of a high-pressure gas jet in a quiescent environment	
			To quantify the jet penetration, the Schlieren visualization technique was applied using a high-speed camera that allowed an acquisition rate of 40,000 frames per second.	
8	Flow characteristics of natural-gas from an outward-opening nozzle for direct injection engines	2018	High speed schlieren imaging is used to capture the growth of the highly turbulent transient gaseous jet Radial and axial penetration has been measured for 90-degree conical annular nozzle and round nozzle	[68]
9	Gas dynamics and flow characteristics of highly turbulent under-expanded hydrogen and methane jets under various nozzle pressure ratios and ambient pressures	2016	Large eddy simulations were used to investigate the sonic and mixing characteristics of turbulent under-expanded hydrogen and methane jets with various nozzle pressure ratios Based on the results of this study, correlations were proposed for the shock cell spacing and jet tip penetration of highly under-expanded jets issued from millimeter-size circular nozzles	[69]
10	Numerical modelling of transient under-expanded jets under different ambient thermodynamic conditions with	2016	High-resolution large eddy simulation in conjunction with an adaptive mesh refinement technique was used in order to investigate key mixing characteristics of under-expanded hydrogen and methane jets under various ambient thermodynamics. Penetration rate, volumetric growth and initial transient vortex ring behavior were investigated under near	[70]

	adaptive mesh refinement		atmospheric and elevated ambient pressures and temperatures	
11	A novel CFD approach for modelling the high-pressure direct injection and mixture formation in a spark ignition CNG engine	2016	<p>An URANS-based simulation strategy using the commercial code AVL Fire for the direct injection (DI) of CNG and the mixture formation for different nozzle geometries has been used</p> <p>A fine hexahedral mesh for the injector has been developed</p> <p>Turbulence is modelled using the k-epsilon model</p>	[71]
12	Free under-expanded jets in a quiescent medium: A review	2015		[72]
13	Large-eddy simulation on the effect of injection pressure and density on fuel jet mixing in gas engines	2014	<p>Penetration and mixing of non-reacting methane and nitrogen jets were simulated and compared</p> <p>Demonstration of the influence of the fuel molecular mass, and the injection pressure on turbulent mixture formation in highly under-expanded jets was carried out</p> <p>Understanding of the fuel air mixing dynamics for transient injection was gained</p>	[73]
14	Large-eddy simulation of highly	2013	The aim is to study the effect of nozzle pressure ratios on the characteristics of highly under-expanded jets	[74]

under-expanded
transient gas jets

- | | | | | |
|----|--|------|---|------|
| 15 | Visualization and analysis of the characteristics of transitional underexpanded jets | 2013 | The flow structure and turbulent mixing of pulsed jets issuing from a circular nozzle was investigated using acetone planar laser-induced fluorescence (PLIF) | [75] |
| | | | By monitoring axial and various radial cross-sections under different injection pressure conditions, different features of gaseous jets were visualized and interpreted | |
| 16 | Hydrogen-fueled internal combustion engines | 2009 | This paper is a comprehensive overview of H ₂ internal combustion engines and has a section for H ₂ jets | [76] |

Chapter 3. Experimental Methodology

3.1. Testing System Overview

To evaluate injection and ignition characteristics of gaseous fuels, an experimental facility was designed and developed at VESST research lab at SFU. Details of the methodology and systems being used in this research are discussed in this chapter. The objectives of testing system preparation included design, development and manufacturing an experimental facility and validation of the test system components and enhancements to the analysis and processing tools. The procedure involved automated processes and employing high-speed recording to visualize and analyze injection and ignition events. The developed experimental facility enables injection and ignition characteristics of gas jets with different injection conditions including gas composition, upstream and downstream pressure, and nozzle hole size. Initial parts of the testing were conducted at ambient pressure, and later phases of the work were conducted at elevated back pressures in a custom-designed chamber.

Fuel composition, injection pressure, and nozzle pressure ratio (NPR) are among the factors that affect the gas jets properties. As discussed in chapter 2, the dependency of gaseous jets structural characteristics on the injection parameters has been the subject of several experimental and numerical studies. In this study, physical characteristics of gaseous jets including axial and radial penetration, spread angle, velocity, mass flow rate, and momentum rate of free jets are experimentally investigated and calculated using the fluid mechanics fundamentals. After investigating the physical properties of model and combustible gases as free jets, the ignition properties of combustible gas jets composed of hydrogen, methane, and representative blends were evaluated quantitatively and qualitatively using a hot surface as an ignitor. The prepared testing system allows visualization of the ignition of the jets as the hot gases around the hot surface start to ignite and the flame start to propagate.

In this work, the schlieren imaging method is utilized to visualize the jets using a high-speed camera. For this purpose, gaseous jets are generated by injection into a test section through a nozzle with a circular hole. The creation of the gaseous jets is imaged using the Schlieren system and camera from the beginning at the exit of the nozzle to the developed phase of the jet with 25000 frame per second imaging. The high frame rate

imaging allows visualization of the structural properties of the jet within the few milliseconds of the jet transition and development. High resolution of the images displays the near-field structure of the jet in the distances equal to a few nozzle diameters from the nozzle exit. Formation of several shock cells due to under-expansion of jets are visible in the obtained images. The boundary of the jets at the front as it propagates is used to identify the jets penetration and quantify the penetration rate and the boundaries on the sides show the radial penetration and spread angle of the jet (Figure 3-1). These parameters will be described in more detail later in the chapter.

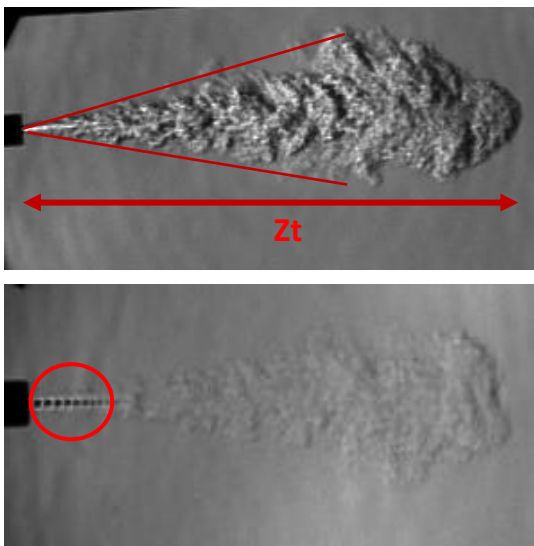


Figure 3-1- Near-field and far-field structure of the jet obtained from the images (He jet injected at 500 kPa(g) (image is taken during the experimental measurement campaign)

To evaluate the effects of higher back pressure on the characteristics of the jet, and to evaluate the injection and ignition properties of gaseous fuels in a more controlled environment, an optical chamber is used in part of the experiments. The optical chamber is a rectangular block made of steel with two quartz windows on the sides for visualization of injection and ignition inside the chamber. More specifications of the chamber are discussed later in this chapter.

To visualize and study the ignition event, an ignition source (glow plug) perpendicular to the jet is located through the upper plate of the chamber to enable studying the jets interacting with it. Before ignition happens, there need to be enough mixing of the air with the fuel jet to form a combustible mixture. Being in the vicinity of the

glow plug and having enough residence time, hot fuel gases around the ignitor find ample energy to ignite (Figure 3-2). Depending on the ignition timing, the mixture quality, and fuel properties, different proportions of the fuel/air mixture get ignited. Estimating the ignition delay, the time between the start of injection and the start of ignition, is a valuable outcome of ignition studies to evaluate and compare the ignition delay of fuel mixtures consisting of hydrogen and natural gas. Ignition delay is different for different compositions of the fuel mixture and various injection pressures and pulse widths. Dependency of the ignition delay on these parameters are investigated in this study.

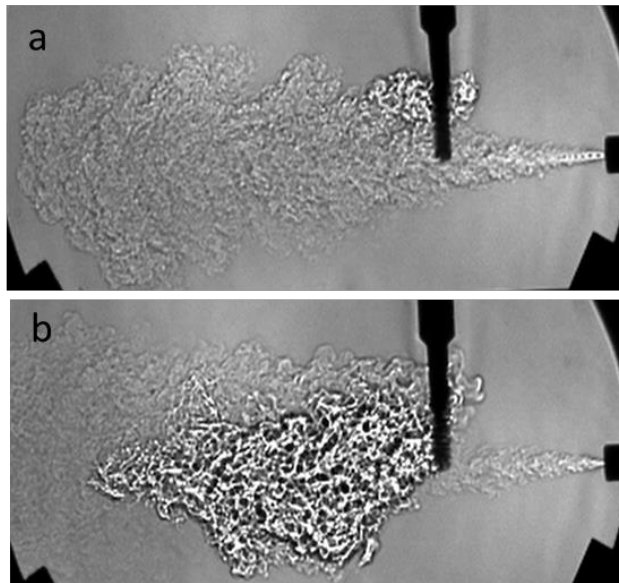


Figure 3-2- a) Air entrainment and mixing b) Ignition and flame propagation

The next sections of this chapter discuss the experimental hardware, the measurement approaches, the data processing, and analysis tools.

3.2. Experimental Apparatus: Mechanical Set-up

Injection System Parts and Components

The injection rig is composed of these main components:

- Fuel supply
- Injector and nozzle assembly

- Instrumentation and measuring systems
- Data acquisition and control systems
- Schlieren system and high-speed camera
- Optical chamber

The injection facility is equipped with a National Instruments data acquisition and control (DAQ) system which is connected to a computer running a custom-built MATLAB Simulink programming environment. A schematic of the experimental rig is shown in Figure 3-3.

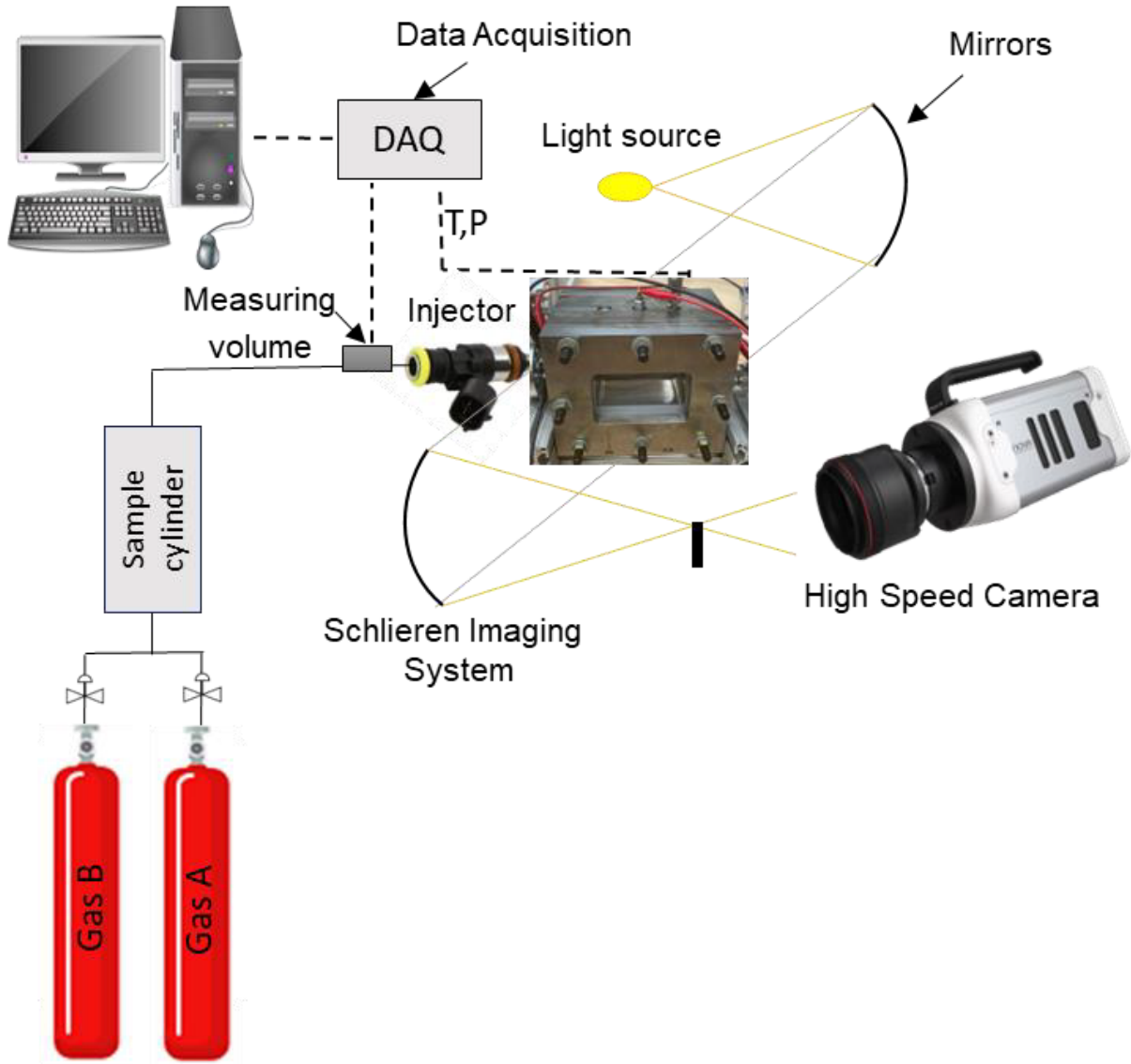


Figure 3-3- Schematic drawing of the injection system

3.2.1. Mechanical Components

Mechanical components of the system include:

- **Gas supply:** The gas supply sources are high purity industrial grade T size cylinders equipped with regulators. The pipes to supply gas from the cylinders to the test area are ¼" steel pipes. There is an in-line regulators to adjust the pressure on the upstream of the injector.

- **Sample Cylinder:** A 500 ml sample cylinder (rated for up to 5000 psi pressure) is used to store gas for flow measurement purposes. This cylinder is also employed to mix gases to function as a secondary gas supply containing gas mixtures with various compositions. Making mixtures in this container is based on partial pressure and ideal gas assumption. Using a secondary container is also beneficial in terms of safety where only small amount of combustible gas in the mixing cylinder is available in each experiment and the main T tank gas supplies are closed during the experiments.
- **Injector:** The Injector is a Bosch NGI-2 commercial injector clamped on a fixture (Figure 3-4 a) to inject gas directly into the atmosphere or into the pressurized chamber that was added to the system later in the project. This injector is an outward opening injector that does not create a jet upon injection. As a result, the jet dynamics are not obvious. So, a nozzle is placed on the injector tip to generate jets upon injection. The nozzle diameter is 1 mm. The injector, and its installment on the injector block for the ambient test facility and on the chamber for increased back pressure experiments are shown in Figure 3-4 (d) and (e). The manufacturer's technical specifications of the injector for natural gas is brought in Table 3-1.
- **Nozzle:** The nozzle is custom made with 1 mm exit diameter. The nozzle and its drawing are shown in Figure 3-4 b. The internal volume of the nozzle equals $4.9 \times 10^{-9} \text{ m}^3$.
- **Hot surface:** The hot surface ignitor is a commercial glow plug: *NGK CZ104, 7V, 6A*.

Table 3-1- Bosch NGI-2 injector technical specifications (obtained from Bosch datasheets)

<i>Property</i>	<i>Value</i>
<i>Coil Resistance</i>	9.1 Ohms / Low Impedance
<i>Dead Time</i>	0.45ms at 14 volts
<i>Static Flow Rate @ 43.5 PSI (300 kPa) w/Gas</i>	2200 cc/min = 210 lb/hr
<i>Static Flow Rate @ 58 PSI (400 kPa) w/Gas</i>	2550 cc/min = 240 lb/hr
<i>Connector</i>	Denso / Sumitomo
<i>Injector Length</i>	O-Ring to O-Ring: 1.5. / 37.5 mm
<i>Injector Body Diameter</i>	16mm
<i>O-Ring</i>	14.5mm Viton

In the injection configurations used in these experiments, the nozzle is installed on the injector connecting and holding in place through the body of the block (for the ambient pressure tests) and the body of the chamber (for the experiments conducted in the chamber). The injector, nozzle, and their installments are displayed in Figure 3-4.

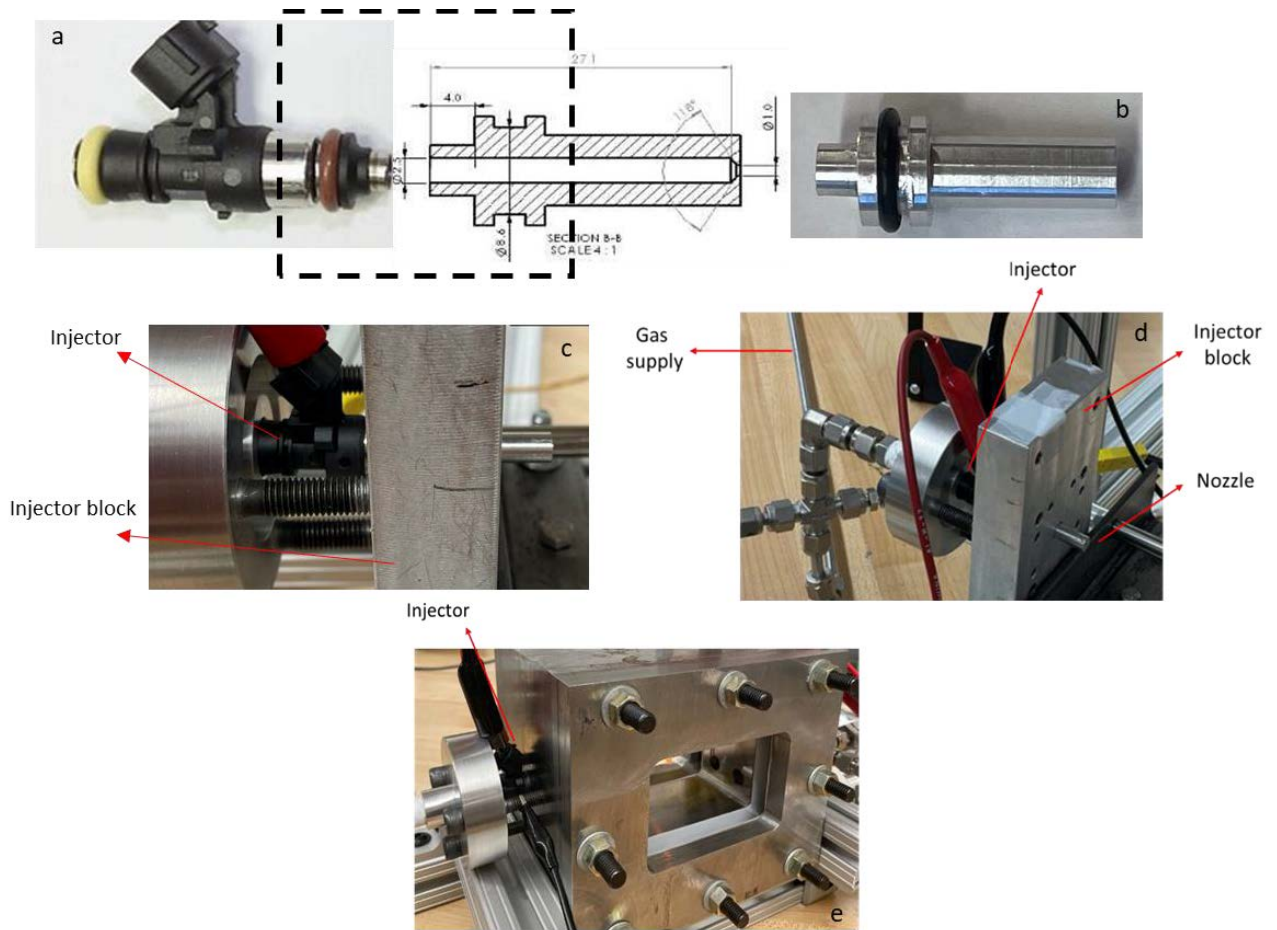


Figure 3-4- Injector and nozzle assembly a) injector connection to the nozzle b) the nozzle with 1mm hole diameter c) the injector connection to the nozzle through the injector block d) the injector block used in atmospheric tests e) the chamber used in tests with increased back pressure (and atmospheric back pressure)

3.2.2. Optical Chamber

In parts of the experiments that there is no back pressure, the gas was injected into the air, but to conduct the experiments with increased back pressure, an optical chamber was designed and built. The chamber was used to assess injection characteristics with increased back pressure and to provide a controlled environment for the ignition experiments. More details on the design and functionality of the chamber are brought in the following.

- **Size and material:** The chamber is made of 1018 Cold Rolled Steel with two fused quartz windows installed on the flanges on both sides. The internal dimensions of the chamber are:

Length: 4", width:3.5", height:2.5"

Internal volume: 35 in³ or 0.00058 m³

Optical window size: 4"×2.5", viewing area: 10 in² or 0.000163 m²

- **Pressure capability:** The chamber has been designed for 2.4 MPa pressure with safety factor of 4. The safety factor of 4 has been applied to both windows and the chamber body. An FEA analysis has been done following the design of the chamber which can be found in the VESST research group documentations. The CAD drawings of the chamber are brought in the appendix for more information.
- **Injector orientation:** The injector is clamped and sealed on the side of the chamber body attached to the nozzle. The nozzle tip is aligned with the field of view on the side windows.
- **Back pressure provision:** back pressure is provided using pressurized air from the lab. Installations for the air input are placed on the chamber body on the opposite side of the injector installation. The pressure inside the chamber is controlled using a back pressure regulator and is measured using a sensor installed on the chamber. The pressurized air is fed into the chamber while the outlet air stream from the chamber goes to the vent through the back pressure regulator.
- **Ignitor installment:** There are three counterbores on the top of the chamber body for placing the ignitor at different distances from the nozzle exit and to place a thermocouple probe inside the chamber. The remaining counterbore stays closed while the others are occupied by the glow plug and thermocouple. For the ignition experiments, the hot surface ignitor is placed on the middle counterbore which has 40 mm distance from the nozzle tip. Although the location of the ignitor can be changed to closer or further away from the nozzle tip, its not within the scope of this work.

- **Safety considerations:** Although the chamber is designed for high pressures and the thickness of the body and the windows have been selected accordingly, other safety considerations are also in place. A pressure burst disk (for 1700 kPa pressure) is connected to the chamber on one side and connected to the vent on the other side to provide an extra safety feature for the operation of chamber.

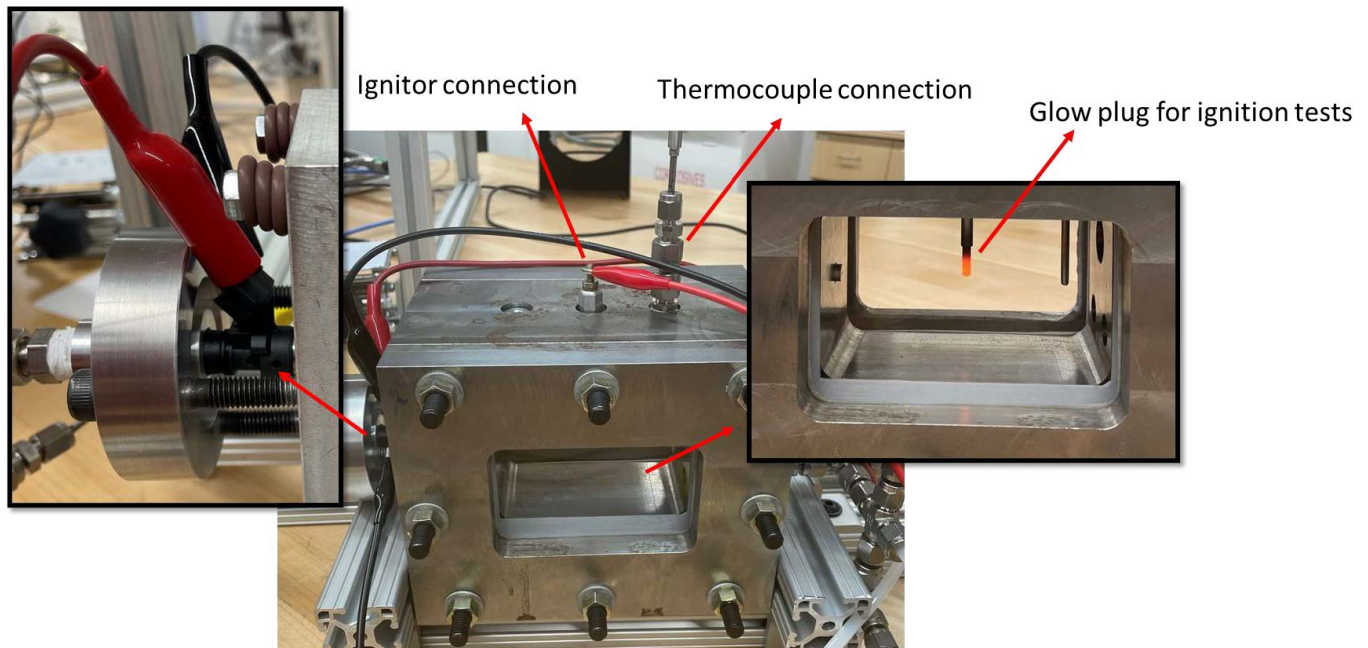


Figure 3-5- injector, optical chamber, the ignitor (glow plug)

3.3. Instrumentation, Data Acquisition and Control System

The injection facility is equipped with a National Instruments (NI) data acquisition and control (DAQ) system (model NI USB-6361). The DAQ is connected to a computer running a custom-developed control and data recording program built in the MATLAB programming environment. The DAQ is configured to control and measure high-speed data and to monitor changes in system's pressure and temperature to characterize injection and ignition events. A mass flow meter used to measure the volume of the system used for mass flow rate measurements. The DAQ has various inputs and outputs to control the parameters including three pressure sensors, and a thermocouple which are the DAQ

analog inputs, and the injector and camera command as the analog outputs. The scripts of the MATLAB program that was used as the software interface is provided in the appendix.

The DAQ is configured to:

- Command injection with different pulse widths
- Acquire high-speed data for pressure and temperature measurements
- Trigger the camera to start recording simultaneous to the start of injection

3.3.1. Instrumentations

The instrumentation used in this research include pressure sensors, mass flow controller, and a thermocouple.

- *Pressure sensors*

The pressure sensors used in these experiments in different parts of the system are presented in Table 4.

Table 3-2- Pressure sensors used in the system

<i>Sensor location</i>	<i>Brand/model</i>	<i>Range</i>	<i>Accuracy of full scale</i>
<i>On the sample cylinder</i>	OMEGA	0-1500 psi (0-10342 kPa)	0.5%
<i>Before the injector</i>	OMEGA	0-150 psi (0-1172 kPa)	0.5%
<i>Inside the chamber</i>	OMEGA	0-600 psi (0-4136 kPa)	0.5%

- *The Mass Flow Controller*

Type: micro motion mass flow sensor

Model: EMERSON CMFS015M323N0A2ECZZ

Accuracy: 0.25%

- *The Thermocouple*

Type: K

Model: 3871K29

Accuracy: $\pm 0.75\%$

3.3.2. Injection Drive System

Injection is commanded by the NI-DAQ with 1 MHz frequency capability, connected to a solid-state relay that triggers the injector power. Delays in the injection command signal has been measured using an oscilloscope. According to the oscilloscope the injection signal delay, the time from the commanded signal to the start of the voltage increase, is about 25-30 μs which is related to the injector drive signal. On the other hand, the injector voltage rise time, from the start of the voltage increase to reaching full voltage, is about 150 μs . This may be related to the required time to build up full voltage at the solenoid coil or it may be due to the details of the driver circuit, which are outside of the scope of this thesis. Moreover, the injection closing signal delay, time from the command end to the time that the injector voltage starts to fall, is about 100 μs . So, the sum of the electrical delay prior to injection is about 180 μs . This value was repeatable with small error.

However, with the employed measurement technique, the start of injection is referred as one frame before the first sign of appearance of the jet in the image. There is a delay from the injector opening to the start of injection due to the need to fill the nozzle itself. In fact, when the injection is commanded and the camera starts recording, it takes about 0.8 ms until the jet appears in the image according to the recordings. This delay is

attributed to both the injector needle lift time, and the gas filling up the nozzle. However, the timescale on the jet development is taken from one frame before this frame where the jet tip has appeared. The camera trigger activates as soon as the injection is commanded so the recording starts a bit earlier than the appearance of the jet in the image and the whole jet evolution is recorded.

The controls that are enabled using the MATLAB interface (provided in the appendix) to command the injection include the pulse width (the injection duration), the number of injections, and the possibility of consecutive injections with defined dwell times.

3.4. Measurement Techniques

In this section the methods and techniques that were employed for injection and ignition characteristics are discussed.

3.4.1. Visualization System: Schlieren Imaging Technique

Schlieren photography is a visualization technique that is widely used to visualize the fluid flows. In this technique, the parallel light rays passing through an observation region will be refracted due to changes in the properties of the fluid in the test region [77]. Schlieren technique provides qualitative assessment of density gradient in the test area. This technique has been used extensively for visualization and characterization of gas jets[30], [62], [75].

As the gas jet enters into the field of view, the momentum of the jet imposes a density gradient into the field. The density and refractive index of the injected gas is different from the density of the gas in the receiving chamber, and the light passing through the test area diverts because of the different refractive index of the gas jet and the surrounding area. This phenomenon will lead to appearance of the jet's image on the camera lens.

Components of a typical schlieren system include:

- Light source
- Concave mirrors
- Cutoffs (knife edge)

From the light source, light is passed through a slit so that the reflected light from a concave mirror forms parallel rays that pass through the test section. The parallel rays are collected by another mirror on the opposite side and focused on the focal point where a knife edge is placed. The rays continue to reflect on a screen or camera lens. If the parallel rays of light pass through a density gradient in the test section, the light ray is bent or refracted. Diverted ray of light does not pass through the focal point and gets blocked by the knife edge, resulting in appearance of darkened lines on the image. Consequently, density gradient causes image formation from the test area. One way to arrange the elements of schlieren system on the table is Z-shaped arrangement which is beneficial in terms of maximizing the viewing area and minimizing the total space required. A schematic of a typical Z-shaped Schlieren imaging system is shown on Figure 3-6 where the mirrors are placed on the two sides of the table collecting light that passes through the test area. The light source and the knife edge are positioned at the focal point accordingly.

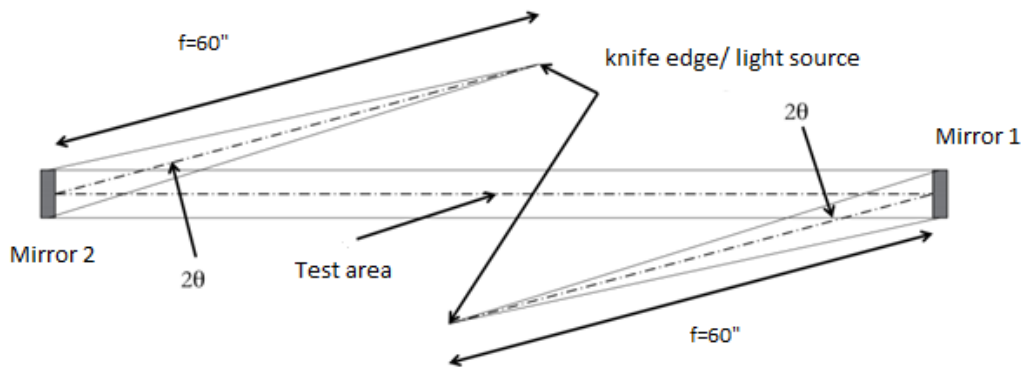


Figure 3-6- Typical layout of a z-type Schlieren system (60" focal point is attributed to the system used in this research)

In this work the schlieren system is composed of two concave mirrors with 6" diameters and 60" focal length, a knife edge, and a LED lamp with a slit with 150 μm diameter located at the focal point of mirror 1. Injection of a gaseous jet into the air creates

density gradient in the test area being reflected on the obtained images based on the described mechanism. The two mirrors were placed on the table on the opposite sides in an appropriate position against the test area. Adjusting and calibrating the system was required to find the right location for the mirrors, the knife edge, and the light source to optimize the space on the table to provide room for the gas supply and injection systems aligned with the visualization system. On the other hand, the high speed camera is located close to the knife edge to record the reflected image from the test area. This configuration allowed capturing the generation and development of the jet within a few milliseconds from the injection to the developed phase. A see-through shield is placed between the camera and the area in proximity of the mirror to avoid the air motion from the camera fan to interfere with the imaging region. Part of the Schlieren set-up and the camera used in this work is shown in Figure 3-7.

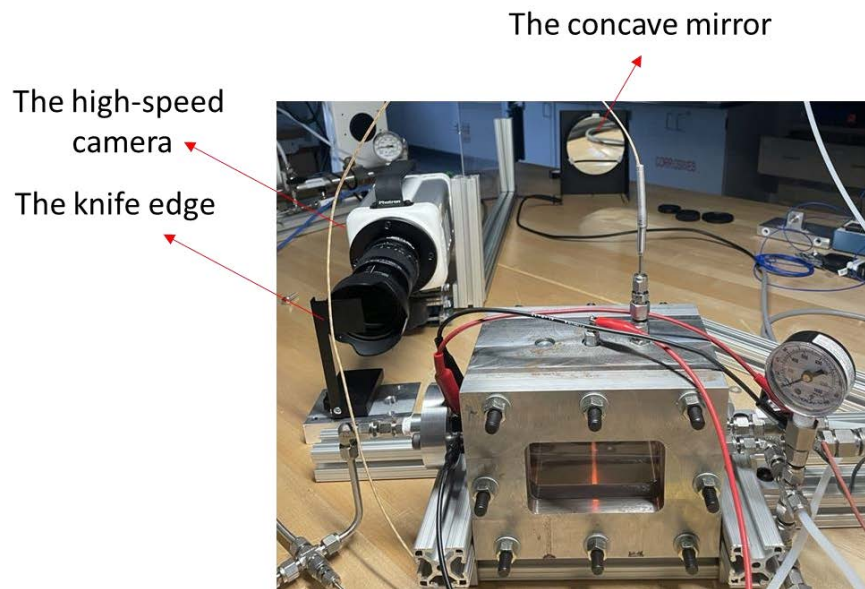


Figure 3-7- Concave mirror, camera, and the chamber (the second mirror is in the opposite side of the table)

3.4.2. Axial Penetration and Spread Angle Measurement

The high-speed camera used for the recordings is a Photron Fastcam Nova S9 with HIS 17-70mm F-mount Zoom lens. The frame rate in which the images were recorded in these experiments were 25000 frames/second which was chosen based on a trade-off between the quality of the images and the frame rate. Higher frame rates lead to limited

amount of light available (darker images) and also decreases the resolution. With the selected frame rate and shutter speed (1/70000 s), the obtained resolution is 680×480. The typical settings for recording were large aperture, high zoom with focus on the nozzle exit. The software interface of the camera enables calibration of the image size to actual size which is 0.4 mm/pixel for these experiments. Calibration of the pixel size was carried out by measuring an object with known length from its image on the camera software. When the injection is commanded, the camera gets triggered, and the recording starts. The recording always starts a few seconds before the actual appearance of the jet at the nozzle exit so the initial arrival is always caught in the videos. The videos in the camera software can be displayed like an image at every frame so the exact form and structure of the jet can be observed at every frame.

Manual measurement of the jets' penetration length was carried out using the camera software by detecting the front edge of the jet and measuring the length of the jet all the way from the tip of the nozzle to the tip of the jet. The tip of the jet is the last pixel of the image along the axis of the jet in the center (Figure 3-8). The manual process requires more effort and introduces potential for human error. However, the ability to reliably detect the individual leading pixel from each image was found to be very difficult for automated processing tools due to run-to-run variations in background noise and some cases of low contrast that made automatic threshold detection more difficult. For the images observed, the operator-induced accuracy was expected to be within +/- 2 pixels.

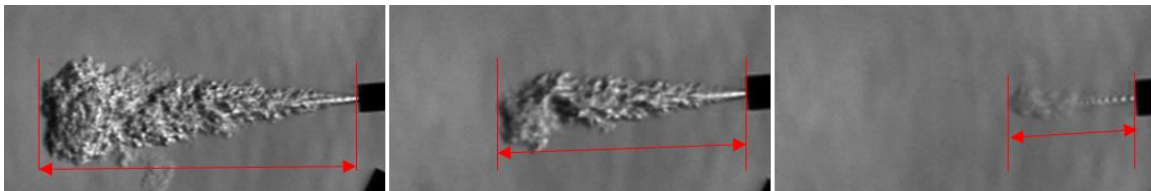


Figure 3-8- Detection of the front edge of the jet and measuring the distance from the nozzle tip for jets in different sizes

In most of the images, the tip of the jet is detectable, and the distance is measurable by the measurement's tools provided in the camera software. In some of the images for gases with closer densities to air, such as methane, the imaging has been repeated several times to catch a visible image from the tip of the jet and measure the length of the jet. More images from the camera software interface are shown in Figure 3-9.

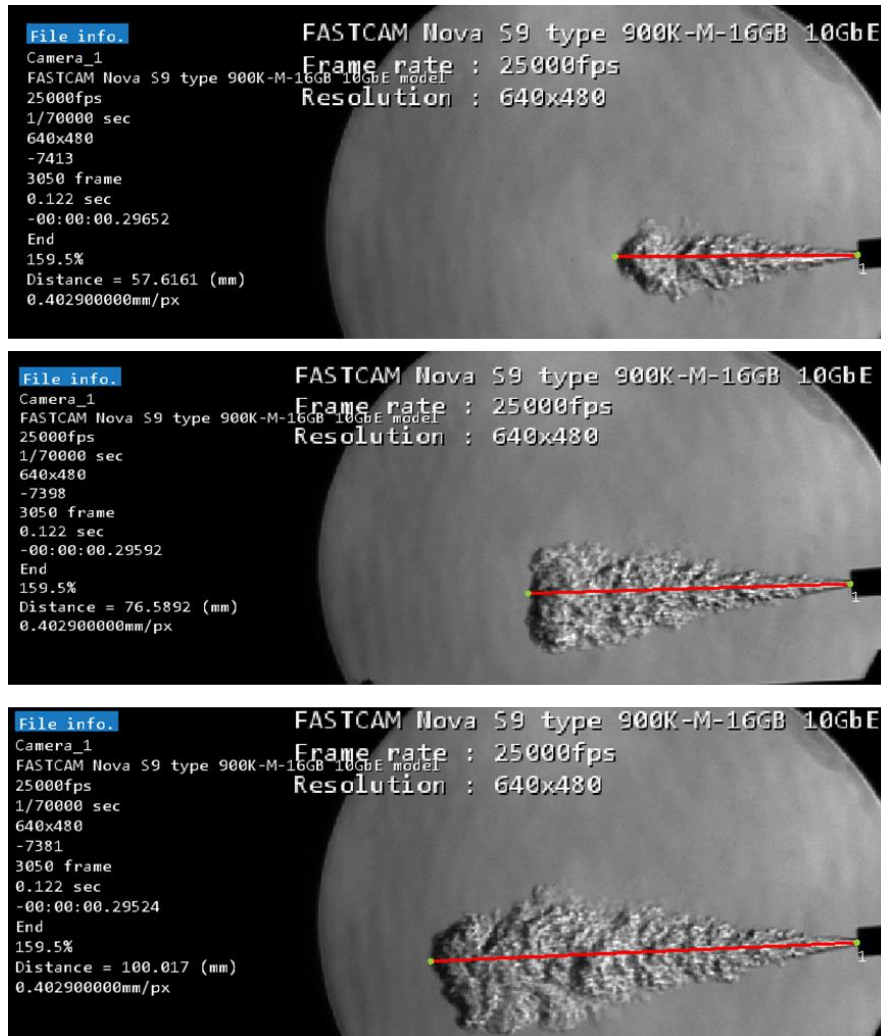


Figure 3-9- Measurement of the jet penetration using the camera software

Injections have been repeated three times and the average of the measured values have been introduced as the jet penetration length for each condition. This will be discussed in more details in the results chapter (Chapter 4).

To measure the spread angle, again using the camera software tool, the full angle of the jet has been measured. The angle has been specified at the 70% of the length of the jet at 90 mm distance from the nozzle tip.

3.4.3. Mass Flow Rate Measurements

One of the characterization parameters attributed to injection is the static mass flow rate. This parameter refers to the mass flow rate of the injected gas when the injector is wide open and injector opening and closing time is assumed to be negligible. To measure the injection static mass flow rate for different gases and various injection pressures, an experimental approach has been taken. For this purpose, the average injection rate was quantified by calibrated measurement of the pressure change in the upstream sample cylinder over several injections. First, the gas was stored in the sample cylinder with a certain pressure. Pressure immediately upstream of the injector (rail pressure) was regulated to the desired pressure using a regulator on the upstream of the injector. Rail pressure was set to 100, 300, 500, and 800 kPa for mass flow measurements. Then the injection was commanded with Injection duration of 10 ms for several times (50 in these experiments). The pressure change in the cylinder was measured using a pressure sensor connected to the sample cylinder. The difference in the pressure of the sample cylinder before and after injections determine the total amount of the injected gas. With real gas assumption considering the compressibility factor (z), equation 1 is used to calculate the injection mass flow rate.

$$\Delta P \cdot V = z \cdot \Delta n \cdot R \cdot T \quad \text{Equation 3-1}$$

Where ΔP is the difference between the sample cylinder pressure before and after the sets of injections. R refers to the universal gas constant and T is the gas temperature in the sample cylinder which is assumed to be constant at room temperature. Z is the compressibility factor obtained from CoolProp for each gas at different pressures. V is the total volume of the sample cylinder and related installments/tubing which was measured using a micro motion mass flow sensor (EMERSON CMFS015M). To calculate the total volume of the system, the sample cylinder was filled with Ar at a certain pressure while the mass flow meter was used on the gas line to measure the total mass of the flowing gas. Using the mass obtained from the sensor, the total volume of the system was calculated using Equation 3-1. The uncertainty of the calculated volume with the mass flow meter described in section 3-3-1, is 1%.

For the static mass flow measurements, for each set of injections, the total pressure drop is measured which the is used to calculate the total mass flow rate. From

these calculations the total mass of the injected gas is obtained, and by dividing that to the total injection time, the average injection mass flow rate is calculated. The static mass flow rate obtained from this part for different gas types and injection pressures contribute to our knowledge about the jets momentum significantly and is used to calculate the nozzle exit momentum, total pressure in the nozzle, and nozzle pressure ratio as discussed in the following sections. The uncertainty in calculation of mass flow rate with Equation 3-1 is calculated as 5% that includes error in calculating P, V, and T.

3.4.4. Nozzle Pressure Ratio Calculations

Injection pressure significantly affects the gas jets properties and subsequent development of the jet on the downstream of the nozzle. Injection pressure is the pressure that is applied at the injector in the gas supply line. The nozzle pressure is the pressure at the nozzle that the jet feels as its upstream pressure. The ratio of the nozzle pressure to the ambient (in cylinder) pressure is called the nozzle pressure ratio (NPR) which has a significant effect on the gaseous jets' characteristics. In this project, in the injection system installment, shown in Figure 3-10 (it has also been discussed in section 3-2-1). The injector and the orifice in fact are two orifices on the flow. For a one-dimensional, steady flow with negligible effects of viscosity and gravity, when there is no heat transfer through the orifice, the flow can be assumed isentropic. In this application, isentropic assumption seems to be reasonable due to very short injection durations. In an isentropic flow over an orifice, the reference parameters for pressure and temperature can be assumed constant. These reference parameters are defined in Equation 3-2 [78].

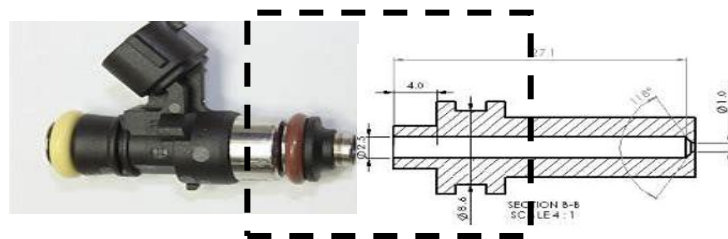


Figure 3-10- Injector and nozzle assembly

$$\frac{p_t}{p} = \left(\frac{T_t}{T}\right)^{\frac{\gamma}{\gamma-1}}, \quad \frac{T_t}{T} = 1 + \frac{\gamma-1}{2}$$

Equation 3-2

Since in choked flow conditions the velocity at the nozzle throat is limited to the speed of sound, the mass flow rate will remain constant and independent of the downstream conditions. There is an equation that relates the choked flow mass flow rate to the gas heat specific ratio, total upstream pressure, total upstream temperature, and the Mach number (Equation 3-3)[78]. In this equation, sonic condition is assumed at the nozzle exit, so the Mach number equals to 1. Using this equation, the total upstream pressure at the nozzle can be calculated using the mass flow rate (Equation 3-4).

$$\dot{m} = \frac{p_t A^*}{\sqrt{RT_t}} \sqrt{\gamma} \left(\frac{\gamma+1}{2} \right)^{(\gamma+1)/2(1-\gamma)} \quad \text{Equation 3-3}$$

$$P_t = \frac{\sqrt{RT_t} \times \dot{m}}{A^* \sqrt{\gamma} \left(\frac{\gamma+1}{2} \right)^{(\gamma+1)/2(1-\gamma)}} \quad \text{Equation 3-4}$$

Where P_t is the total upstream pressure in the nozzle, γ is the specific heat ratio, R is the individual gas constant, T_t is the upstream reference parameter for temperature, A^* is the surface area at the throat of the nozzle, and \dot{m} is the mass flow rate within the nozzle. After measuring the mass flow rate through the experimental approach, the P_t is calculated by using Equation 3. Having P_t allows calculating the NPR using the Equation 3-5.

$$NPR = \frac{P_t}{P_b} \quad \text{Equation 3-5}$$

Where P_b is the injection receiver pressure. In the experiments with no back pressure, P_b equals the ambient pressure and in the experiments with elevated back pressure, P_b equals 250 kPa(g).

To calculate the effective pressure on the nozzle upstream, an experimental approach has been taken as follows. The injection pressures for the sets of injection experiments are set at 100, 300, 500, and 800 KPa gauge pressure at ambient back pressure, and 500, 800, 1000, and 1200 kPa(g) for 250 kPa(g) back pressure. Under these circumstances, for Ar, He, H₂ and CH₄, the flow most likely will be choked (except for 100

kPa injection pressure). The uncertainty in calculating the total pressure approximately is equal to that of the mass flow rate which is calculated to be approximately 5%.

3.4.5. Velocity and Momentum Rate Calculations

As discussed in the literature review, axial penetration is one of the main characteristics in gaseous jets direct injection. In this project, schlieren visualization technique with a high-speed camera is used to measure and characterize the axial penetration of jets with different injection conditions versus time from the high-speed recordings. Also, with the assumption of choked flow at the exit of the nozzle and using the described approach to measure the mass flow rate, exit velocity, and exit momentum rate of the gas jets can be calculated. As mentioned in the literature review (Equation 2-5), the penetration rate of the gas jets has relationship with the gas momentum rate at the nozzle exit. This value is of great importance to characterize the under-expanded jets development rate. Injection pressures for the atmospheric tests are selected as 100, 300, 500, and 800 kPa, and for tests with increased back pressure, 500, 800, 1000, and 1200 kPa respectively. The range is limited to the pressure range that the injector can operate.

Momentum rate at the exit of the nozzle can be calculated as:

$$\dot{M}_n = \dot{m} \times U_e \quad \text{Equation 3-6}$$

Where the mass flow rate is calculated using the described approach and the exit velocity (U_e) is velocity of sound which is equal to:

$$U_e = \sqrt{\gamma RT} \quad \text{Equation 3-7}$$

Where γ is the ratio of specific heats, R is the individual ideal gas constant, and T is the gas temperature in the nozzle before injection. The total temperature over the flow within the orifice is assumed to be constant. To use the Equation 6 to calculate the exit velocity, it is required that the flow be choked, and the Mach number equals 1. This assumption is later checked using the calculated nozzle pressure ratio and its comparison to the critical pressure ratio for each gas at each injection pressure. If the NPR is greater than the critical pressure ratio, this assumption is correct. The uncertainty in calculating the momentum rate is approximately equal to that of the mass flow rate which is 2.5% (section 3-6).

3.5. Gas Blending Systems

The gas mixtures are being made based on partial pressure into a constant volume sample cylinder. The gas bottles are equipped with regulators that enables adjusting the pressure of the gas on the outlet. There are check valves on the gas lines to ensure one-way path of the gas flow from the cylinders. The gas lines from the two cylinders are connected to the sample cylinder having check valves and gate valves on their lines. To make the mixture composing of for example X% of gas A and Y% of gas B based on molar fractions, first the partial pressure of each gas required to make that composition is calculated. The compressibility factor (z factor) has also been considered for more accuracy. Based on the calculations, first the cylinder is filled with the gas with lower partial pressure and then the second gas is added to the cylinder to reach the total pressure. The properties of the mixture are calculated using the Equations 3-8 to 3-11:

$$P = \sum y_i P_i \quad \text{Equation 3-8}$$

$$\frac{P_i}{P} = y_i \quad \text{Equation 3-9}$$

$$PV = ZnRT \quad \text{Equation 3-10}$$

$$Z_m = \sum y_i Z_i \quad \text{Equation 3-11}$$

With the discussed approaches and experimental apparatus, the experiments are conducted using the described methodologies. The results are discussed in the next chapter.

3.6. Measurement Uncertainties

Table 3-3 summarizes the calculated uncertainties for the measured values. For penetration length, the uncertainty in the length measurement equals the pixel size of the images at the speed and conditions of the recordings because the lengths are directly measured using the camera software. For the penetration plots, each measurement has been repeated three times and the reported values are the average of the repeated experiments. The error bars on these plots refer to the sum of the standard deviation values and the measurement uncertainty. All the recordings are conducted at 25000 frame per second, so the measurement uncertainty for time equals to one frame length (0.04 ms). Mass flow rate of the injections are obtained using the experimental approach described in section 3-4-3 and using Equation 3-1 to obtain the number of moles. The number of moles times the molecular weight gives the mass flow rate for each injection experiments. For mass flow measurements also, each experiment has been repeated 3 times and the reported values are the average of the obtained amounts. The uncertainty for mass flow rate in Table 3-3 are the standard deviation values rounded up to 5%. The uncertainty in momentum rate equals the uncertainty in mass flow rate (Equation 3-6). The rail pressure uncertainty depending on the range varies between 0.5% to 5% because the sensor accuracy is 0.50% of full scale. For back pressure, the 0.50% BFSL accuracy results in 3% uncertainty for the back pressure used (250 kpa(g)). The uncertainty for NPR calculations (Equation 3-5) is the sum of the uncertainty on rail pressure and back pressure.

Table 3-3- summary of calculated uncertainties

<i>Measured parameter</i>	<i>Calculated uncertainty</i>
<i>Zt (penetration length)</i>	0.402 mm/pixel
<i>T (time)</i>	0.04 ms
<i>Mass flow rate</i>	5%
<i>Momentum rate</i>	5%
<i>Rail pressure</i>	0.5% - 5% depending on the range
<i>Back pressure</i>	3%
<i>NPR</i>	3.5% - 8%

Chapter 4. Results and Discussions

In this chapter injection and ignition characteristics of gaseous jets under various conditions are presented and discussed to show the effects of important variables on these characteristics. As mentioned in the methodology, inert gases of argon (Ar) and helium (He) are being characterized following by combustible gases of hydrogen (H₂) and methane (CH₄). For initial testing, inert gases (Ar and He and their -50% molar- blend) were used to ensure safe operation and to develop both measurement techniques and fundamental understanding. Combustible gases were then tested to investigate critical parameters on the injection characteristics of H₂, CH₄, and H₂-CH₄ blend (20% H₂ content based on energy and 46% based on mole fraction of H₂). Characterization of gas jets of various compositions sets the groundwork for ignition characteristics of the fuel jets including hydrogen, methane, and their blend later in the chapter.

From the relationships presented in the literature review (Equation 2-5), momentum rate of the gas jets at the exit of the nozzle is a critical parameter affecting the penetration properties of the jet. Having the mass flow rate will allow evaluating the momentum rate at the exit of the nozzle with the assumption of isentropic flow within the nozzle (Equation 3-6). Typically, gaseous jets due to the pressure ratio they undergo within the nozzle flow reach supersonic conditions at the nozzle throat. Thereby the flow at the nozzle will be choked flow and the velocity of the gas will be the speed of sound (Ma=1). This finding enables obtaining the gas velocity at the throat using Equation 3-7. The assumption of choked flow gets validated by calculating the nozzle pressure ratio (NPR) later in the presented results.

Nozzle pressure ratio (NPR), defined as the ratio of the nozzle total pressure to the ambient static pressure, has a significant effect on the characteristics of the gaseous jets. Gaseous jets are categorized according to their NPR to moderately under-expanded ($2 < \text{NPR} \leq 3.846$), and highly under-expanded ($3.85 \leq \text{NPR}$)[19]. In under-expanded jets, formation of oblique shock cells occur after the jet passes the nozzle exit and this pattern repeats to the end of the core area. In a highly under-expanded jet, the severity of these events such as the number of the shock cells are higher. The dimensions of the Mach disk and its location also are varied depending on the level of under-expansion.

Experimental approaches in this research are more focused on the far-field properties (discussed in section 2-2) of the gaseous jets including the axial penetration and spread angle, and the kinetic characteristics of the jets including velocity and momentum. Employing experimental approaches along with the analyses based on the theoretical relationships will allow characterizations of the jets with regard to their injection pressure, back pressure, NPR, and type and composition.

Having an injector following by a nozzle can be treated as two orifices on the path of the flow. However, more complexity in the injector structure imposes irrecoverable losses to the flow which is hard to quantify. Therefore, quantifying the mass flow rate of the jets on the downstream and calculating the total pressure on the upstream of the jet is an approach to determine the total (P_t) and static pressure (P_i) of the flow at the upstream of the nozzle orifice. The injector nozzle assembly used in these experiments were discussed previously in section 3-2-1 in chapter 3. In a schematic in Figure 4-1, the injector nozzle assembly is shown with regard to the pressures at different locations as important parameters in this study. Figure 4-1 shows the P_t , P_i , P_b and P_{inj} on the injector nozzle configuration where:

- P_t is the total pressure on the upstream of the nozzle
- P_i is the absolute static pressure on the upstream of the nozzle
- P_b is the pressure in the receiver where the gas jet is injected into
- P_{inj} is the absolute injection pressure

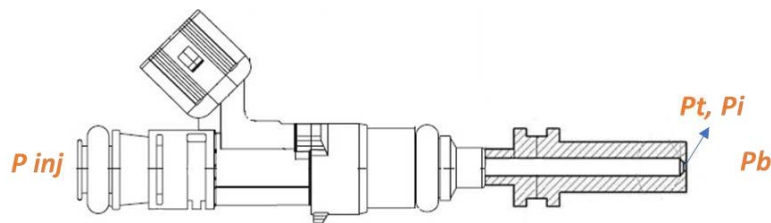


Figure 4-1- Drawing of injector nozzle assembly

It is worth reminding from section 3-4-4 that the mass flow rate of the choked flow is only dependent on the upstream conditions which in this case is the total pressure (P_t). T_t as of Equation 3-3 is a reference parameter that is assumed constant over an isentropic flow. The flow through the nozzle orifice is considered isentropic (it has been discussed in

section 3-4-4). In the following sections, first the injection characteristics of Ar and He are discussed following by the injection characteristics of H₂ and CH₄. In the last section of the chapter, ignition properties of the characterized combustible jets are discussed.

4.1. Argon-Helium injection Characteristics

For initial testing, inert gases (Ar and He and their 50% molar blend) were used to ensure safe operation of the experimental facility and to develop characterization methods to provide fundamental understanding of the process. In the following sections injection characterization of Ar and He are presented and discussed. The injection experiments in this section were conducted only in ambient pressure conditions (no back pressure).

4.1.1. Injection Flow Characteristics

Injection characteristics of Ar and He have been evaluated at 4 different injection pressures as listed in Table 4-1. Table 4-1 presents the specifications and calculated properties of Ar and He at injection pressures of 100, 300, 500, and 800 kPa(g). For isentropic flows, P_t and T_t have been shown to be useful reference parameters that remain constant throughout the flow. T_t is the constant reference parameter at room temperature (298 K) over the flow within the injector and the nozzle. This assumption comes with the isentropic assumption of the flow within the orifices as discussed earlier in the chapter and in the methodology in section 3-4-4. Specific heat ratio (γ) is calculated using CoolProp at different pressures. To evaluate the assumption of choked flow at the nozzle exit for the configuration used in these experiments, the critical pressure ratio (PR_{cr}) has been calculated to compare to NPR. If the NPR is greater than the PR_{cr} , the assumption is valid. PR_{cr} is obtained from Equation 4-1:

$$PR(cr) = \left(\frac{2}{\gamma+1}\right)^{\frac{\gamma}{\gamma-1}} \quad \text{Equation 4-1}$$

Where γ is the specific heat ratio of the gases.

Table 4-1- Gas properties at different injection pressures

No	Gas type	P_{inj} (kPag)	P_{inj} (kPa(g))	MW (g/mole)	T (K)	R (j/Kg.k)	γ	PR_{cr}
1	Ar	100	201.3	39.95	298	208	1.669	2.054
2	Ar	300	401.3				1.675	2.058
3	Ar	500	601.3				1.681	2.061
4	Ar	800	901.3				1.689	2.066
5	He	100	201.3	4.002		2080	1.666	2.052
6	He	300	401.3				1.666	2.052
7	He	500	601.3				1.666	2.052
8	He	800	901.3				1.665	2.052
9	50% blend	100	201.3	7.27		1909.81	1.667	2.052
10	50% blend	300	401.3				1.670	2.054
11	50% blend	500	601.325				1.673	2.056
12	50% blend	800	901.325				1.677	2.060

For each condition, the required parameters and gas properties are calculated using the experimental measurements and the fundamental fluid mechanic relationships. These properties include the mass flow rate, the exit velocity, the momentum rate, the exit temperature, the total pressure, the static upstream pressure, and the nozzle pressure ratio (NPR). The mass flow rate has been calculated using the described approach in chapter 3 (using Equation 3-1) based on the pressure drop measurements in the sample cylinder. The mass flow rate in the choked flow conditions has a relationship with the upstream pressure and temperature of the flow in the orifice (Equation 3-2). This equation leads to obtaining the total pressure on the upstream of the nozzle P_t (Equation 3-3-).

By having P_t , the static pressure at the throat (P_i) is calculated using Equation 3-4. Although T_t over the flow is constant, the temperature at the exit of the nozzle (T_e) at choked conditions is only dependent on γ and is calculated using Equation 3-4. Velocity (U_e) and momentum rate at the exit (\dot{M}_n) are calculated using Equation 3-6 and 3-7 respectively. Table 4-2 presents the results of calculated parameters at different conditions. In Table 4-2, the properties of the individual gases and the blend of them are presented. The gas blend of Ar-He is a non-reacting gas mixture that can be treated as a homogenous mixture with consistent properties throughout. Each gas's contribution to the properties of the mixture is related to its molar fraction in the blend. In this regard, the gas mixture is made in the sample cylinder with partial pressure consideration. The mass flow rate measurements have been conducted similar to the individual gases.

Table 4-2- Calculated parameters for different injection conditions

Gas type	P_{inj} (kPag)	\dot{m} (kg/s)	P_t (kPa)	p_i (kPa)	P_b (kPa)	T_e (K)	PR_{cr}	NPR	U_e (m/s)	\dot{M}_n (kg/m ² .s ²)	
1	Ar	100	0.000426	186.1	90.5	101.3	223.3	2.054	1.83	321.63	0.137
2	Ar	300	0.000842	367.2	178.4	101.3	222.8	2.058	3.62	322.21	0.271
3	Ar	500	0.001281	557.7	270.5	101.3	222.3	2.061	5.50	322.79	0.413
4	Ar	800	0.001824	793.1	383.9	101.3	221.6	2.066	7.82	323.56	0.590
5	He	100	0.000126	173.7	84.6	101.3	223.5	2.052	1.71	1016.19	0.128
6	He	300	0.000245	339.1	165.2	101.3	223.5	2.052	3.34	1016.19	0.249
7	He	500	0.000369	510.3	248.6	101.3	223.5	2.052	5.03	1016.19	0.375
8	He	800	0.000545	753.2	367.1	101.3	223.6	2.052	7.43	1015.89	0.554
10	B	300	0.000264	344.4	163.8	101.3	223.4	2.053	3.39	997.70	0.264
11	B	500	0.000410	534.1	254.1	101.3	223.6	2.055	5.27	997.70	0.409
12	B	800	0.000595	775.7	369.1	101.3	223.7	2.058	7.65	997.70	0.594

4.1.2. Formation of Jets and Penetration Rate (Z_t)

As described in the literature review, the penetration rate of gaseous jets is one of the important aspects of the gas jets determining their behaviour. As mentioned in the methodology, the penetration rates of gaseous jets in this research are obtained with visualization approach using high-speed imaging. In this section the axial penetration and spread angle of Ar and He in a range of injection pressures with atmospheric back pressure are presented and discussed.

The sequences of He jet development are displayed in Figure 4-2 for injection pressure of 800 kPa(g) over the first few milliseconds after injection. As the jet develops, it propagates in axial direction and grows in radial trajectory. Start of injection (SOI) has been defined as one frame before the first moment that the jet tip appears at the nozzle exit. The time intervals displayed on the images in Figure 4-2 are after the SOI. Using the approach described in chapter 3, the penetration at the axial direction has been measured and graphed versus time in Figures 4-3, 4-4, and 4-5 for Ar, He and Ar-He blend respectively. Each experiment has been repeated three times and the reported values are the average of the measured values. The error bars on the Y-axis (the penetration rate)

are the standard deviation of the data. On the X-axis, the error bar is the length of each frame in the high-speed imaging which is 0.04 ms (for 25000 frame per second speed). An increase in the injection pressure increases the penetration rate as expected owing to the fact that increasing the injection pressure, increases the exit momentum, thereby enhancing the penetration rate.

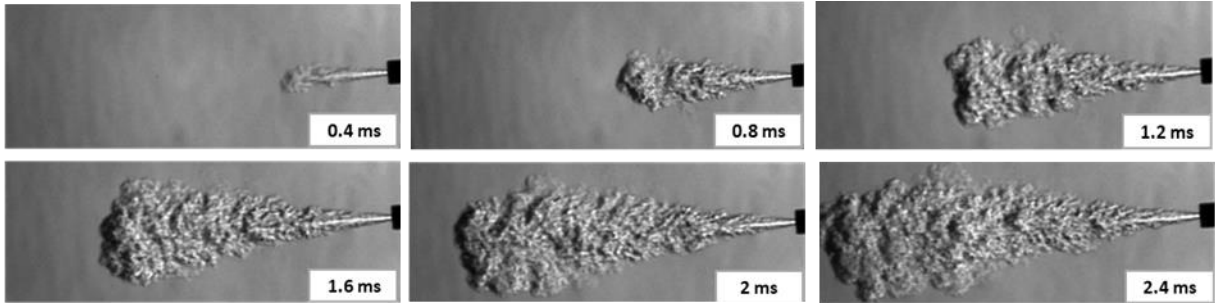


Figure 4-2- Development of He jet at 800 kPa(g) injection pressure

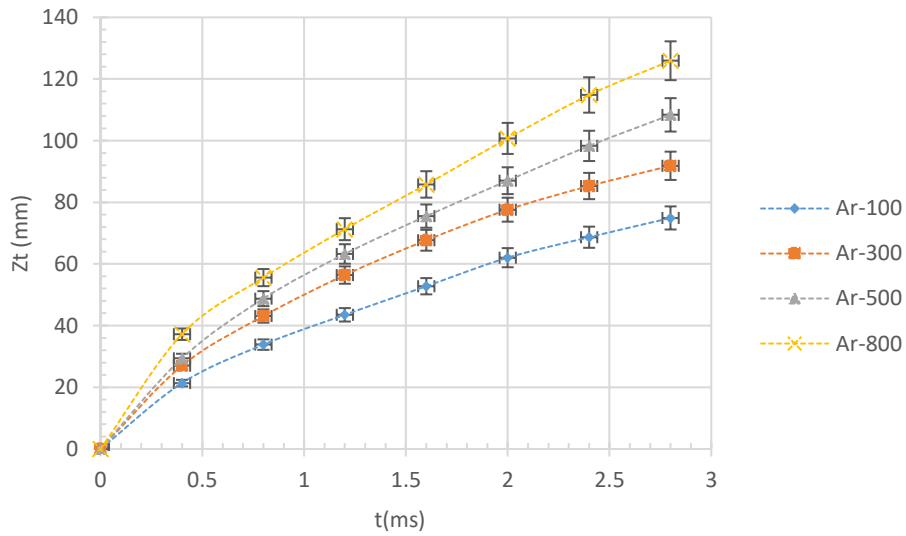


Figure 4-3- Ar penetration vs time (number represents the upstream injection pressure)

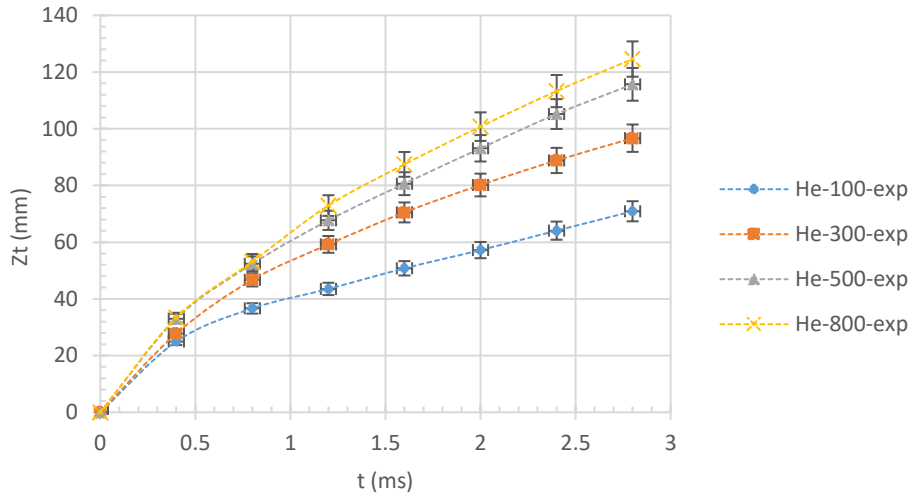


Figure 4-4- He penetration vs time (number represents the upstream injection pressure)

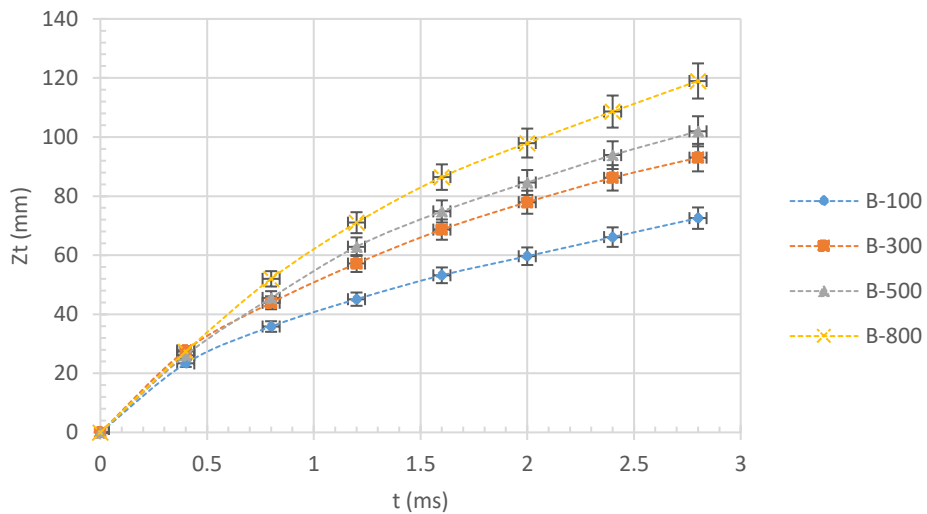


Figure 4-5- Ar-He blend (50% molar) penetration vs time (number represents the upstream injection pressure)

According to Figures 4-3, 4-4, and 4-5, the injection pressure has a significant effect on the penetration rate. However, the gas type, in this case, Ar, He and their blend does not show a sensible effect on the penetration rate at a constant injection pressure. Figure 4-6 shows the penetration rate of these gases at 800 kPa(g) injection pressure on the same plot which suggests that the penetration rate for them is not a strong function of

the gas type and composition. For other injection pressures the similar trend exists regarding the gas type and composition.

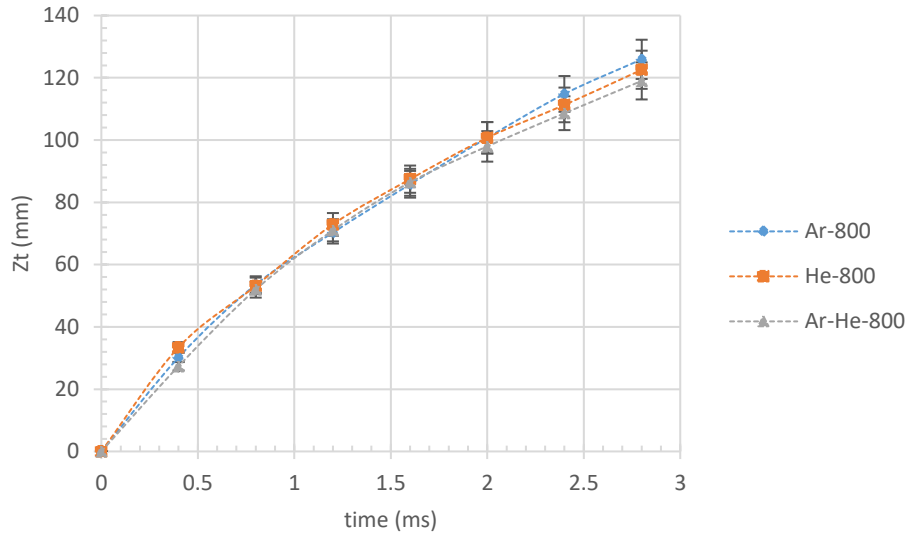


Figure 4-6- Penetration of Ar, He, and the 50% molar blend at 800 kPa (g) injection pressure (number represents the upstream injection pressure)

The reason that the gas composition doesn't affect penetration is that these gases have similar momentum rates at the nozzle exit at each injection pressure (refer to Table 2). Momentum rate is obtained by multiplication of the mass flow rate by the exit velocity (Equation 3-5). Ar, has a higher molecular weight, therefore having higher density and higher mass flow rate. On the other hand, He has lower mass flow rate compared to Ar, but has higher exit velocity. It is worth reminding that the exit velocity at the throat with choked flow is the speed of sound and is obtained from Equation 3-6. The reason the velocity of He is higher than Ar is that its individual gas constant (R) is higher (Table 4-1). In the momentum rate equation, the higher value of the mass flow rate compensates for the lower value of the velocity and vice versa, leading to similar values in terms of the momentum rate.

To exclude any factor related to the gas type in penetration rate, and to plot a normalized form of penetration rate, $z'_t / \left(\frac{M_n}{\rho_{ch}} \right)^{1/4}$ can be plotted against $t^{1/2}$ to exclude the momentum rate from the penetration equation (Equation 4-2). The slope of this plot is a constant according to Equation 2-5 which is in the range of 2.5 to 3.1 in the literature. This

plot is shown for Ar and He at 800 kPa(g) injection pressures as a representative of other injection pressures in Figure 4-7. The same justification exists for 300 kPa and 500 kPa injection pressures (The 100 kPa injection pressure is excluded from the calculations because the NPR at this pressure is lower than the critical pressure ratio and it is not choked flow (Table 4-2)).

$$\frac{z'_t}{\left(\frac{\dot{M}_n}{\rho_{ch}}\right)^{1/4}} = \Gamma \cdot t^{1/2} \quad \text{Equation 4-2}$$

Equation 4-2 is another form of the Equation 2-5. Figure 4-7 demonstrates that $z'_t/\left(\frac{\dot{M}_n}{\rho_{ch}}\right)^{1/4}$ has a linear relationship with $t^{1/2}$ and the slope for Ar and He under these circumstances are similar. This further indicates that the momentum rate of the gases has a significant effect on the penetration rate. If two gases have similar momentum rate, the penetration rate will most likely be similar for them. For Ar and He Γ is obtained 2.71 and 2.70 respectively. The deviation from the linear relationship is observed in the beginning of the jet development where the jet is approaching its fully developed state, the shock cells are being formed, and the pressure in the nozzle is being built up. The first two data points on the $t^{1/2}$ axis belong to 0.4 ms and 0.8 ms. Approximately after 1 ms the linear relationship is governed with higher certainty. If the irregularity in the first 10 frames (the first 0.4 ms after injection) are excluded from the plot, a better linear relationship fits the data with the slope of 3.2 and 3.4 for Ar, and He (Figure 4-8). When the developing phase is excluded, the slope is higher which is mainly because in the developing phase, the nozzle is still being filled up and the pressure on the upstream of the nozzle is not stabilized yet. The value for the slope of this graph, Γ , for gaseous jets is between 2.5 and 3.1 in the literature as discussed in the literature review.

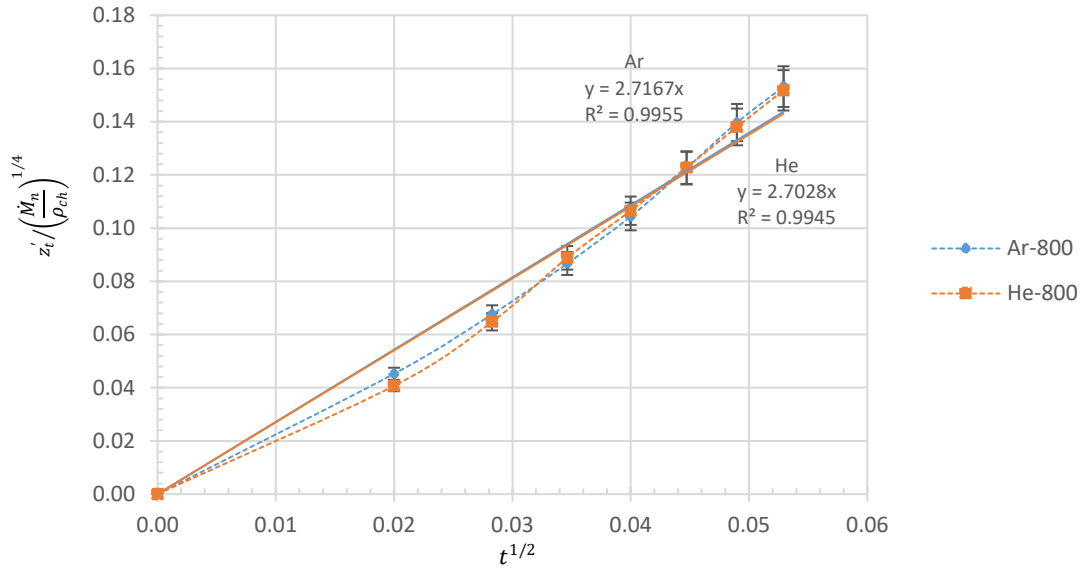


Figure 4-7- Plotting experimental data according to Equation 4-2 (Ar-He)(number represents the injection pressure in kPa(g))

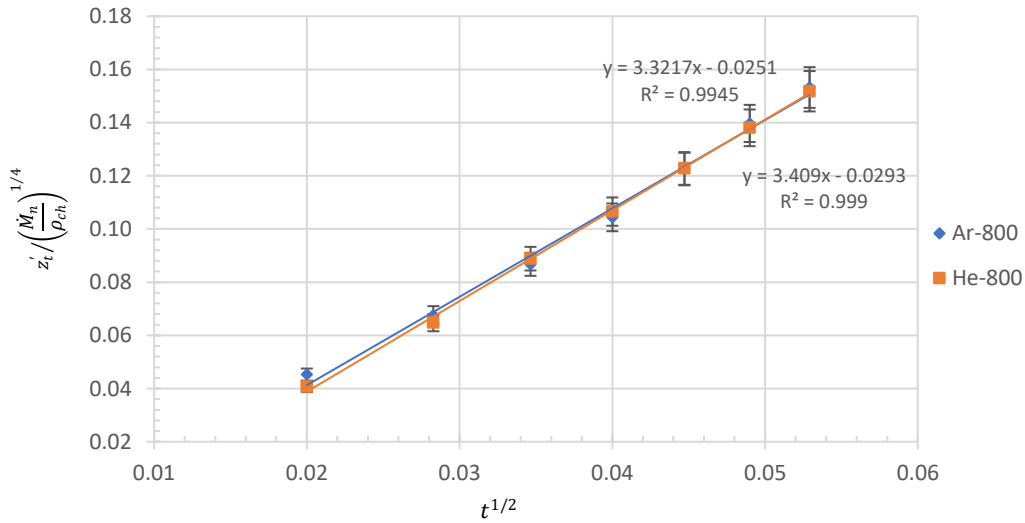


Figure 4-8- Excluding the developing phase, the first 0.4 ms, from the plotted data of Figure 4-7

4.1.3. Spread Angle

As it was observed from the images and from the fundamental understanding of the gas jet development, the jet grows in the radial direction as well as the axial direction due to conservation of momentum and energy in the gas jet. The jet is mixing and slowing down as it entrains air. This then causes the gas jet to widen. The radial direction

development in a three-dimensional view is referred as the volumetric growth. From a two-dimensional point of view, the spread angle is a quantified parameter that can be used to evaluate the radial development of gas jets. From the obtained images of Ar and He through the injection experiments, the spread angle of them is extracted and quantified using the camera software interface. Figure 4-9 shows this aspect of Ar, He and the 50% molar blend on the images (the full angle shown by the red lines) which suggests that He spreads with a wider angle compared to Ar. This is expected from the lower density of He which makes it take up more space as it expands. It seems that their blend is between them in terms of the spread angle.

The spread angles are a function of both injection pressure and gas composition, as shown in Figure 4-10. Figure 4-10 shows the estimated spread angle of these gases at different injection pressures. The data points are the average of three measurements and the error bars are based on the standard deviation. From the literature, it is expected that the jet becomes self similar after distances greater than 10-15 nozzle diameters and the ratio of the jet diameter to its length becomes constant. This means the spread angle of the jet does not change when it reaches the fully developed phase. For consistence of measurements, the spread angles presented in Figure 4-10 are taken at 70% of the axial distance from the nozzle when the jet tip is 90 mm away from the nozzle tip. At this point the jet is fully developed and the angle does not change in further distances. Helium jets seem to get wider as the injection pressure increases, however the spread angle for argon does not seem to be changing much with increasing injection pressure. The importance of spread angle in jets characteristics is related to the effect it can have on the mixing rate. Wider angles lead to larger volumetric growth which enhances the area of contact with the surrounding fluid. Since mixing happens on the edges of the jet, this leads to improved mixing which is of great importance when it comes to jets ignition. The discussed results are with non-reacting gases. It is important to understand the effects for combustible gases.

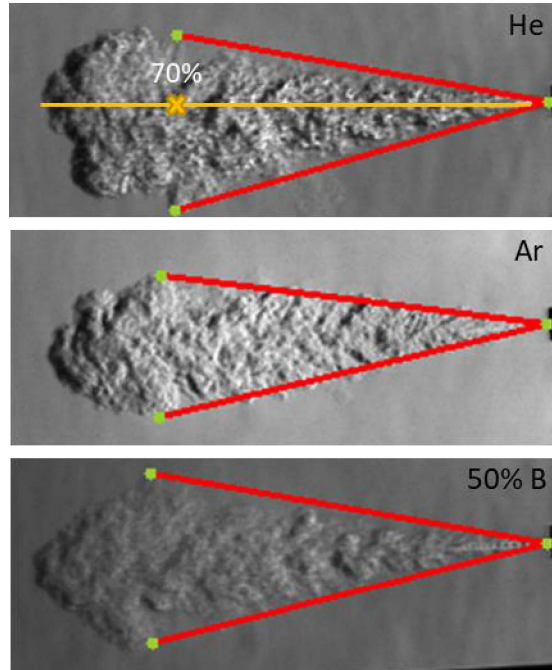


Figure 4-9- Spread angle of Ar, He and 50% on molar basis blend, obtained from the images

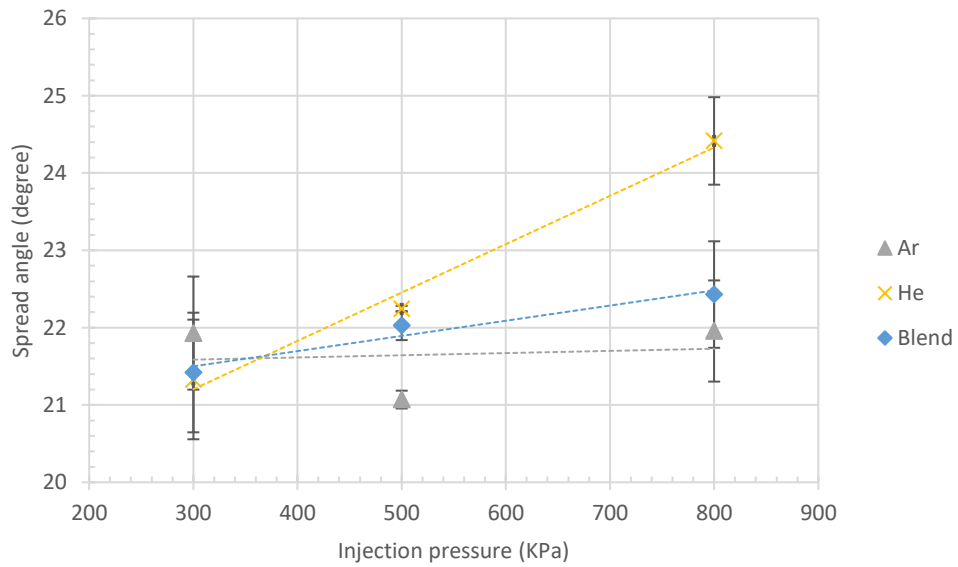


Figure 4-10- Spread angle of Ar, He and 50% molar blend at different injection pressures into the atmosphere at 90 mm penetration

4.2. Hydrogen-Methane Injection Characteristics

Injection characteristics of the inert gases of argon and helium were presented and discussed in the previous sections. In this section, the characterization of combustible gases of hydrogen and methane and their blend consisting of 46% hydrogen on a molar basis. This molar fraction of hydrogen equals 20% on the energy basis in the blend. Similar to the previous section, first the injection flow characteristics are discussed, following by the penetration and spread angle results. For combustible gases, there is also discussions around the ignition event which are discussed in section 4-5.

4.2.1. Injection Flow Characteristics

Similar to Ar and He, injection characteristics of H₂ and CH₄ have been conducted at 4 different injection pressures into the ambient pressure receiver. An additional variable to investigate for combustible gases would be the effect of increased back pressure on the injection and ignition characteristics of the gas jets. Table 4-3 presents the specifications and calculated properties of H₂, CH₄ and their blend (consisting of 46% on molar basis-20% on energy basis), at injection pressures of 100, 300, 500, and 800 kPa(g) at ambient receiver pressure and 500, 800, 1000, and 1200 kPa(g) at elevated back pressures. Again, here with isentropic assumption, P_t and T_t are being considered as useful reference parameters that remain constant throughout the nozzle flow. The specific heat ratio (γ) is calculated using CoolProp at different pressures. Again, to evaluate the assumption of choked flow at the nozzle exit for the configuration used in these experiments, the critical pressure ratio (PR_{cr}) is compared with NPR.

Table 4-3- specifications and calculated properties of H₂, CH₄ and 46% blend (based on molar fraction of hydrogen)

No	Gas type	P_{inj} (kPa(g))	P_{inj} (kPa (abs))	P_b (kPa(g))	MW (g/mole)	T (K)	R (j/Kg.k)	γ	PR_{cr}
1	H ₂	100	201	101	2.01	298	4124.2	1.669	2.054
2	H ₂	300	401	101				1.675	2.058
3	H ₂	500	601	101				1.681	2.061
4	H ₂	800	901	101				1.689	2.066
5	CH ₄	100	201	101	16.04		518.3	1.666	2.052
6	CH ₄	300	401	101				1.666	2.052
7	CH ₄	500	601	101				1.666	2.052
8	CH ₄	800	901	101				1.665	2.052
9	B	100	201	101	9.59		2177.3	1.667	2.052
10	B	300	401	101				1.670	2.054
11	B	500	601	101				1.673	2.056
12	B	800	901	101				1.677	2.060
1	H ₂	500	201	253	2.01		4124.2	1.681	2.054
2	H ₂	800	401	253				1.689	2.058
3	H ₂	1000	601	253				1.693	2.061
4	H ₂	1200	901	253				1.697	2.066
5	CH ₄	500	201	253	16.04		518.3	1.666	2.052
6	CH ₄	800	401	253				1.665	2.052
7	CH ₄	1000	601	253				1.664	2.052
8	CH ₄	1200	901	253				1.664	2.052
9	B	500	201	253	9.59		2177.3	1.673	2.052
10	B	800	401	253				1.677	2.054
11	B	1000	601	253				1.679	2.056
12	B	1200	901	253				1.683	2.060

*B refers to H₂-CH₄ blend (20% energy and 46% mole fraction of H₂)

For each condition, similar to the discussion on the experimental approach and calculations in section 4-1-1, Table 4-4 presents the results of calculated parameters at different conditions for the combustible gases.

Table 4-4- Calculated parameters for different injection conditions

Gas type	P_{inj} (kPa(g))	\dot{m} (kg/s)	P_t (kPa)	p_i (kPa)	P_b (kPa)	T_e (K)	PR_{cr}	NPR	U_e (m/s)	\dot{M}_n (kg/m ² .s ²)	
1	H ₂	100	0.000088	181.3	104.2	101	247.8	1.89	1.79	1314.1	0.116
2	H ₂	300	0.000167	342.9	180.8	101	247.7	1.89	3.38	1314.5	0.219
3	H ₂	500	0.000257	528.8	278.8	101	247.7	1.89	5.21	1314.5	0.338
4	H ₂	800	0.000379	779.7	411.1	101	247.7	1.89	7.69	1314.5	0.498
5	CH ₄	100	0.000247	185.2	103.8	101	258.4	1.83	1.82	449.1	0.111
6	CH ₄	300	0.000483	361.3	196.4	101	257.9	1.83	3.56	450	0.217
7	CH ₄	500	0.000721	538.5	292.2	101	257.2	1.84	5.31	451.01	0.325
8	CH ₄	800	0.001086	809.5	438.2	101	256.3	1.84	7.98	452.37	0.491
13	H ₂	500	0.000257	531.6	280.3	253	247.7	1.89	2.1	1314.5	0.338
14	H ₂	800	0.000379	772.2	407.2	253	247.7	1.89	3.05	1314.5	0.498
15	H ₂	1000	0.000474	976.2	514.8	253	247.7	1.89	3.85	1314.5	0.623
16	H ₂	1200	0.000538	1107.5	583.8	253	247.6	1.89	4.37	1314.5	0.707
17	CH ₄	500	0.000721	555.2	301.3	253	257.2	1.83	2.20	451	0.325
18	CH ₄	800	0.001086	820.9	444.3	253	256.3	1.83	3.24	452.3	0.491
19	CH ₄	1000	0.001338	995.9	538.2	253	255.9	1.84	3.93	453.2	0.606
20	CH ₄	1200	0.001552	1153.4	622.1	253	255.2	1.84	4.55	454.2	0.705
21	B	500	0.000376	530.8	258.1	253	253.2	1.89	2.09	1044.9	0.392
22	B	800	0.000563	793.7	385.4	253	253.1	1.89	3.12	1044.9	0.587
23	B	1000	0.000690	972.4	472.1	253	252.5	1.87	3.83	1044.9	0.710
24	B	1200	0.000798	112.4	545.2	253	251.3	1.86	4.43	1043.1	0.734

*B refers to H₂-CH₄ blend (20% energy and 46% mole fraction of H₂)

4.2.2. Formation of Jets and Penetration Rate (Z_t)

Evolution and formation of hydrogen and methane jets have been evaluated using the images obtained via visualization system and high-speed imaging. Penetration of hydrogen and methane jets have been extracted from these images to evaluate the development of fuel jets quantitatively and qualitatively. Figure 4-11 shows the sequences of H_2 jets development at 300, 500, and 800 kPa(g) injection pressure over the first few milliseconds after injection. These images are representative, and this sequence of development is observed in other injection pressures too. However, as the level of under-expansion increases by increasing the injection pressure, the number of the shock cells at the core of the jet at the nozzle exit seems to be increasing even though the exact number and characteristics of them are not achievable through these images. Within the first few frames (around 0.4 ms), the jet is approaching its developed phase and the shock cells are being created. The jet is growing in both axial and radial directions and the air starts to entrain to the jet from the edges. For H_2 jets, the volumetric growth gets noticeably greater at the same time intervals when the injection pressure increases. For these jets, higher injection pressure, not only increases the axial penetration rate, but also enhances the radial spread significantly (Figure 4-11).

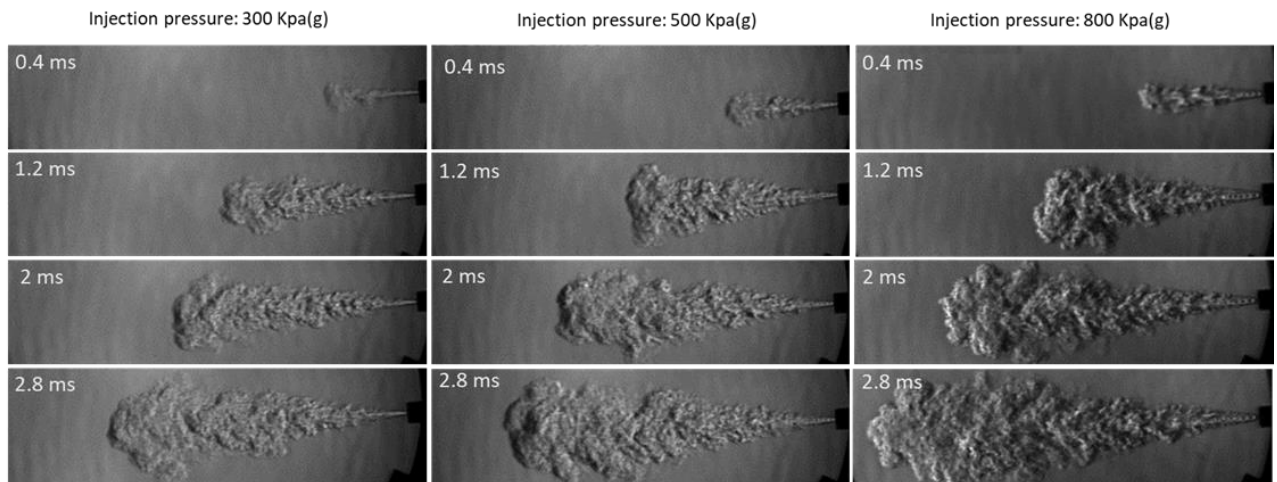


Figure 4-11- Development of H_2 jets at different injection pressures into the ambient pressure. The time intervals are after start of injection (ASOI)

Unlike hydrogen jets, the methane jets (Figure 4-12) show small differences in terms of volumetric growth in different injection pressures although the axial penetration is noticeably increased in higher injection pressures. To compare the hydrogen and

methane jets, Figure 4-13 shows the evolution of these jets under similar conditions. At 800 kPa(g) (the injection pressure of the images in Figure 12), the NPR for CH₄ and H₂ jets are 7.69, and 7.99 respectively. These values for NPR categorize these jets as extremely under-expanded. The creation of several shock cells is a result of decreasing the pressure to the ambient pressure in a series of steps. There seems to be a very clear difference between H₂ and CH₄ for this aspect. Specifically, the H₂ jets seem to start to expand right away, while the CH₄ stays very constrained until the end of the shock cells. Also, it is worth mentioning that the CH₄ jets are harder to see than the H₂ jets because of the smaller difference in the index of refraction and density gradient for CH₄-air compared to H₂-air.

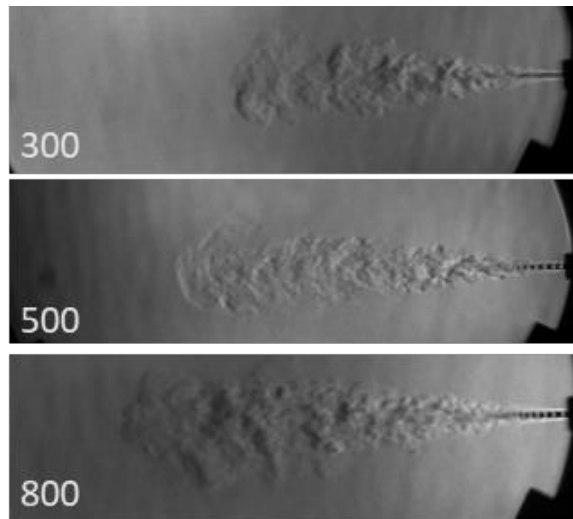


Figure 4-12- Methane jets at 2 ms after injection at 300, 500, and 800 kPa(g) injection pressure (numbers refer to the injection pressure)

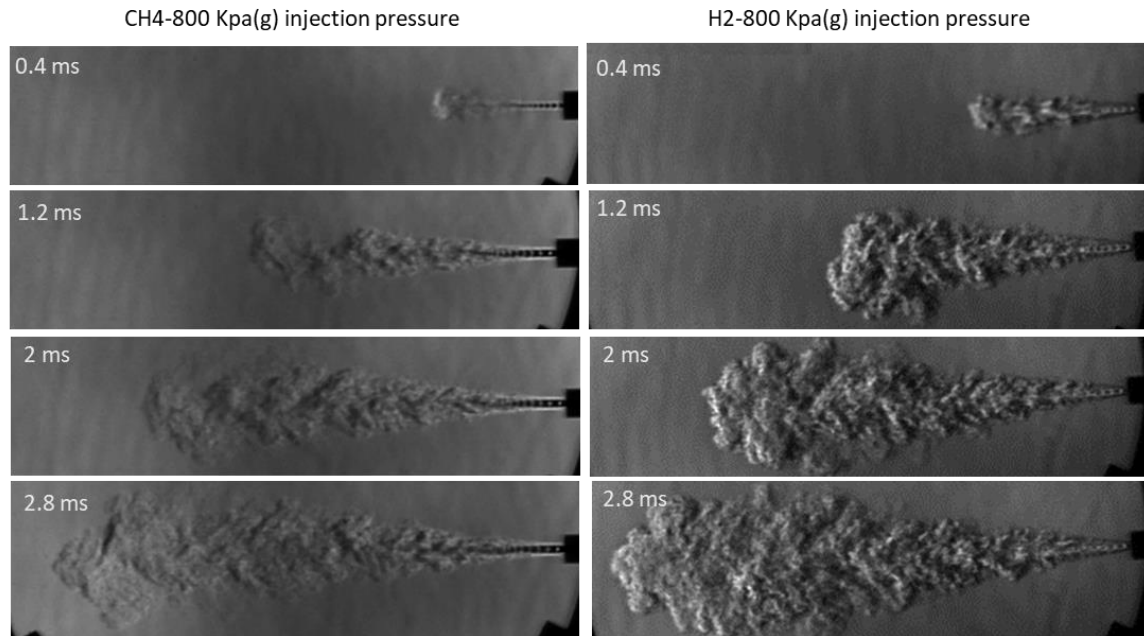


Figure 4-13- H₂ and CH₄ jets evolution at 800 kPa(g) injection pressure

At the same time intervals, although the axial penetration rates for them are close, the radial penetration rate are different. Hydrogen with high exit velocity at the nozzle throat, lower molecular weight and higher diffusivity tends to spread in the radial direction more than methane. As a result, hydrogen jets are noticeably bulkier than the methane jets. This behaviour brings about wider spread angle and larger volumetric growth for hydrogen jets (the spread angle is discussed more in the following sections). This property can be expected to affect the ignition properties of hydrogen jets as higher volumetric growth enhances the air entrainment and mixing. Moreover, the length of the core area of the methane jets seems longer compared to hydrogen jets and the core is continuing with a narrow angle from the beginning until the developed phase. This can also cause less air fuel mixing because the mixing does not occur within the core area.

Another noticeable point from the images is that the size of the shock cells increases to some point and then stays constant. From the literature review, we know that the Mack disk height has a correlation with the static pressure (P_i) at the nozzle (Equation 2-2). For the time that the pressure at the nozzle is being built up and reaches the P_i value, the Mack disk height (the shock cell size) increases and after the P_i is reached, the size of the Mack disk does not change. This is more visible in methane jet and is displayed in Figure 4-14.

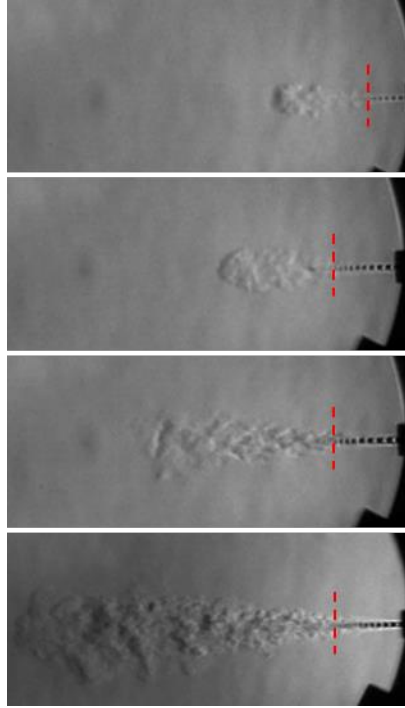


Figure 4-14- Size of the shock cells increasing in the developing phase (methane jets at 800 kPa(g) injection pressure)- the red labels show the observed length of expansion zone

To quantify the penetration rate and comparing H_2 , and CH_4 at different injection pressures, penetrations of these gases are plotted versus time in Figures 4-15 and 4-16. For each injection condition, the experiment has been repeated three times and the plotted values are the average of the obtained values. The error bars add up the percentage error from the standard deviation of the data and the percentage of the measurement uncertainty using the camera software (0.4029 mm/pixel). Similar to the discussion for inert gases, an increase in the injection pressure rises the penetration rate due to the fact that increasing the injection pressure, enhances the exit momentum, by this means increasing the penetration rate. The penetration rate of hydrogen and methane under the circumstances of the experiments do not show a distinctive difference at the same injection pressure which is related to the values of momentum rate at the nozzle exit which make the gases end up in similar penetration rate as long as the chamber density is constant.

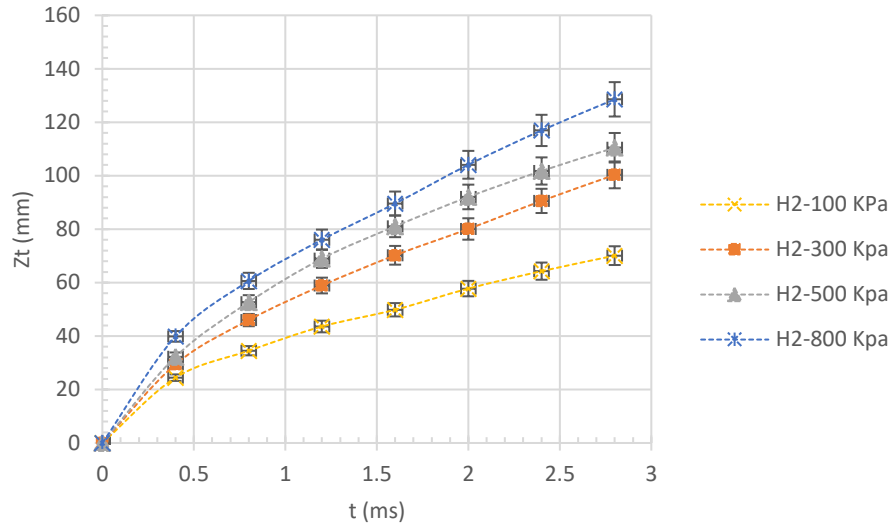


Figure 4-15- H₂ penetration vs time (the numbers represent the injection pressure in kPa(g))

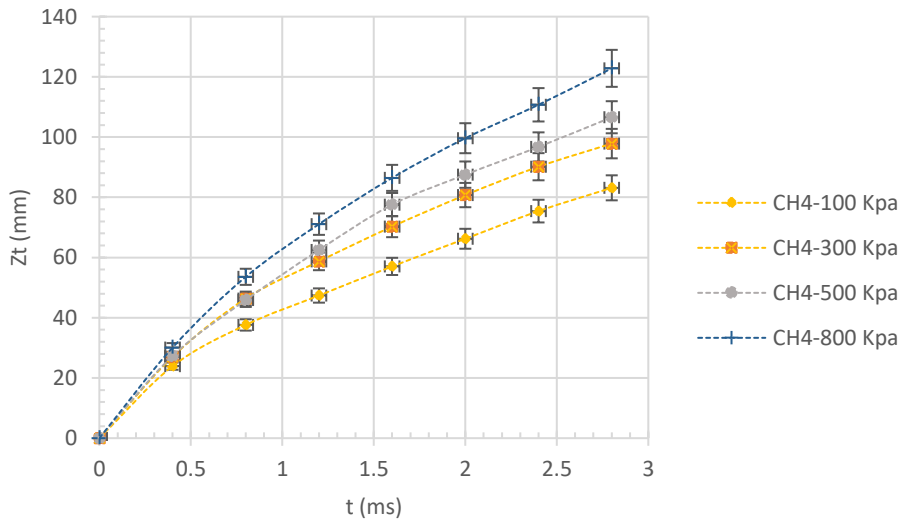


Figure 4-16- CH₄ penetration vs time (the numbers represent the injection pressure in kPa(g))

Similar to the discussions for inert gases, $z_t' / \left(\frac{\dot{M}_n}{\rho_{ch}} \right)^{1/4}$ is plotted against square root of time to exclude the momentum rate from the penetration rate equation (Figure 4-17). This relationship relates gas jet penetration to time, momentum and density based on theoretical predictions. The linear relationship is also observed for H₂ and methane jets with some deviations in the first millisecond after injection which is due to the pressure build up in the nozzle, initiation of the jet development and creation of shock cells in the

distances close to the nozzle tip while the jet is approaching its developed phase. The slope of this graph, which is known as Γ in the penetration rate equation, has values of 2.89 and 2.74 for H₂ and CH₄ respectively that are well within the expected range based on the literature. If the irregularity in the first 10 frames (the first 0.4 ms after injection) are excluded from the plot, a better linear relationship fits the data with the slope of 3.3 and 3.4 for H₂, and CH₄ (Figure 4-18). When the developing phase is excluded, the slope is higher which is mainly because in the developing phase, the nozzle is still being filled up and the pressure on the upstream of the nozzle is not stabilized yet.

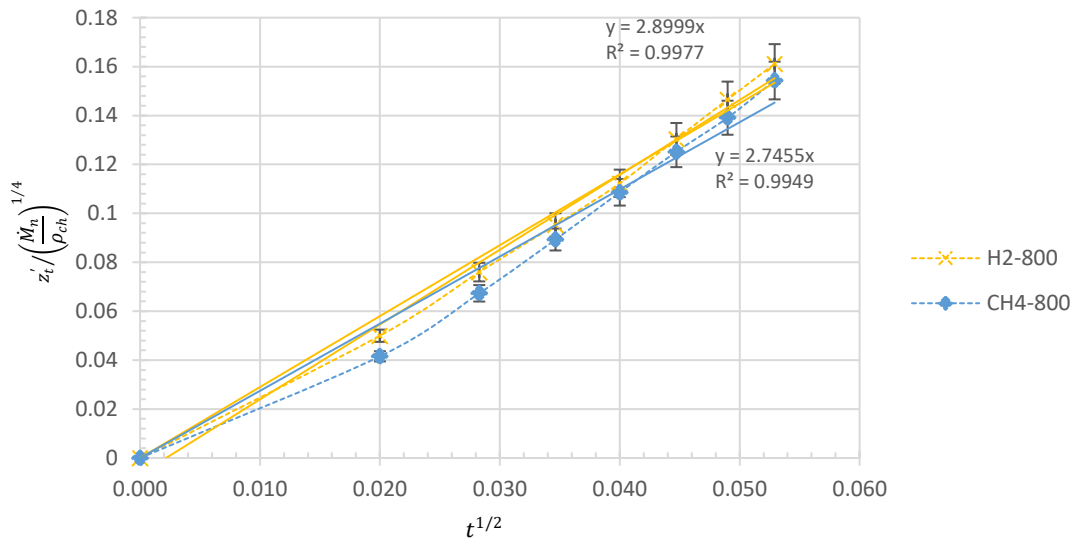


Figure 4-17- Plotting experimental data according to Equation 4-2 (H₂-CH₄)

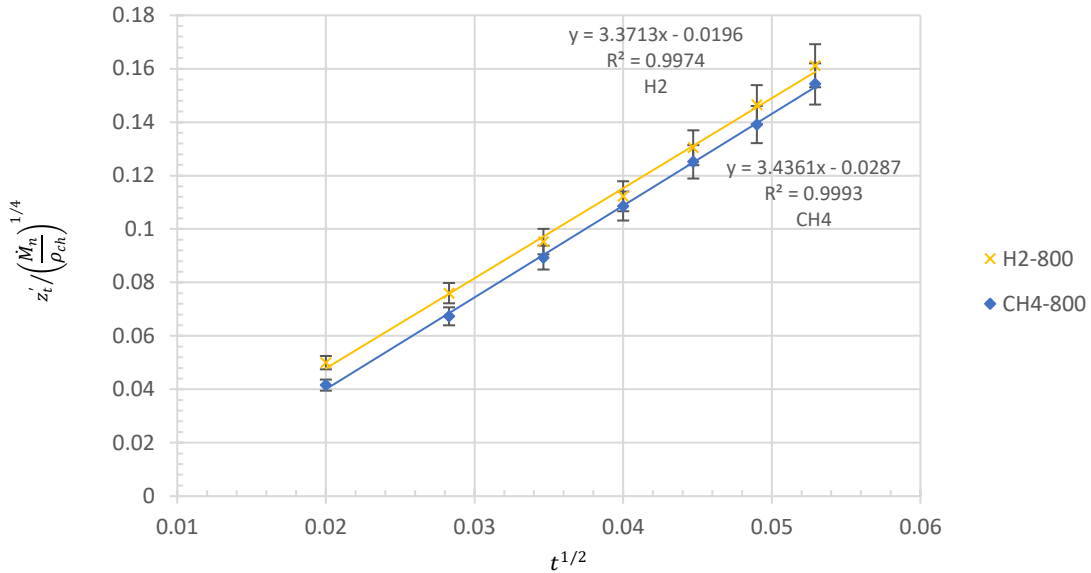


Figure 4-18- Excluding the irregularity in the first 10 frames from the experimental data

As a conclusion for penetration rate discussion at ambient receiver pressure, the Z_t of the gases of experiments are graphed in a single plot to make the comparison easier. As it is clear in Figure 4-19, the penetration of gases at the same injection pressure (800 kPa(g) for this graph) share similar values in atmospheric back pressure injections. As it was discussed earlier, the fact that these gases have similar momentum rate values under the same injection pressure, and the penetration rate has correlation with the fourth square root of the momentum rate, the penetration rate values are similar and are within the error range. The relation between the momentum rate and injection pressure are more discussed in the following sections. Next part discusses the role of back pressure on the axial penetration rate.

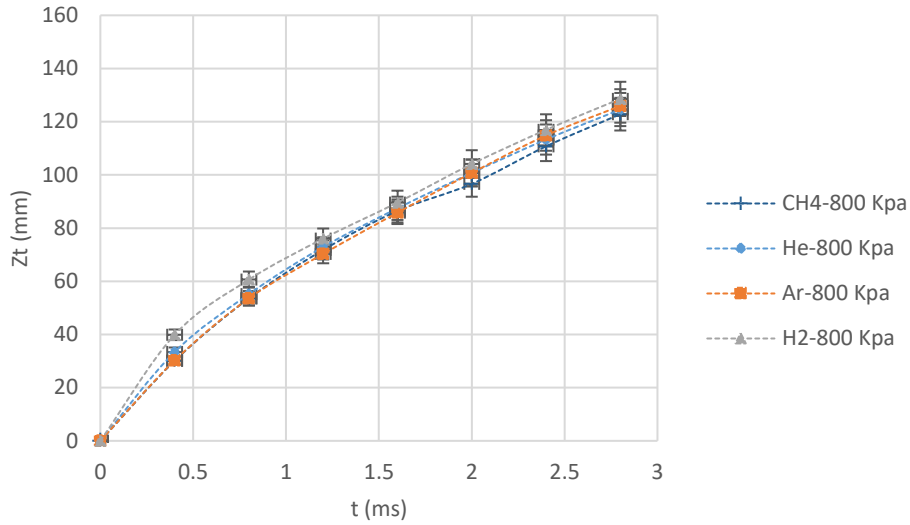


Figure 4-19- Ar, He, H₂, CH₄ penetration at 800 KPa(g) injection pressure at ambient receiver pressure

4.2.3. Effect of Back Pressure

In this section, the injection experiments have been conducted using the chamber with increased back pressure of 250 kPa(abs). The value of back pressure (BP) is constant in these experiments and every where within the text that is referring to the increased back pressure, it means 250 kPa(abs). While the injection pressure range was 100 – 800 kPa(g) for atmospheric tests, the range of injection pressures with back pressure is 500-1200 kPa(g) to maintain a similar range for pressure ratio. This range is defined considering that the maximum limit pressure on the injector used in these experiments is 1200 kPa(g). Having back pressure inside the chamber is a physical resistance against the generation and movement of the jet. The effect that is expected from this resistance is decreasing the penetration rate. Figure 4-20 displays the evolution of hydrogen jets under atmospheric and 250 kPa(g) back pressure with 500 kPa(g) injection pressure. According to this image, the jet under back pressure (the right column) is penetrating slower compared with atmospheric back pressure (the images on the left column).

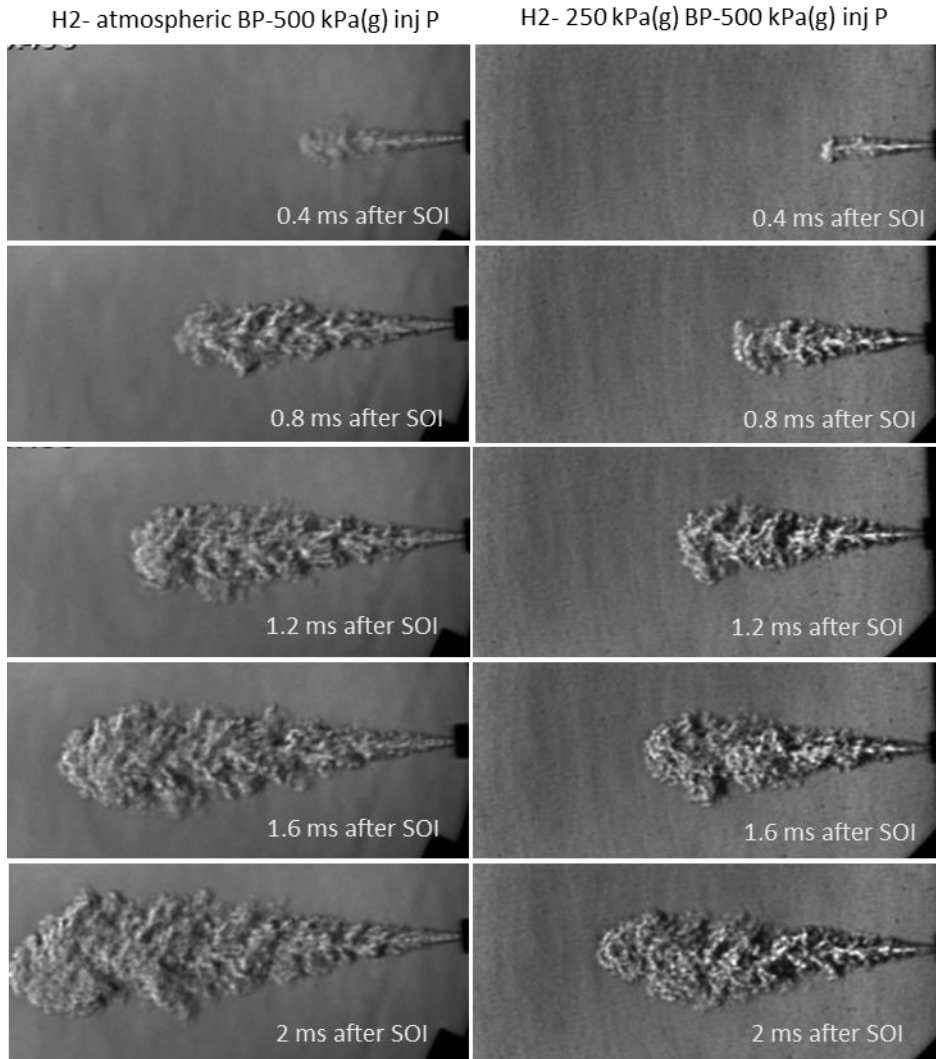


Figure 4-20- H₂ jet evolution with atmospheric, and increased back pressure

From the established equation of 2-5 for the jets penetration rate, it is also expected that the jets penetrate slower at the same injection pressure when there is back pressure in the chamber. Figure 4-21 shows the penetration rate of hydrogen jets with atmospheric and increased back pressure which confirms the effect of back pressure on reducing the penetration rate.

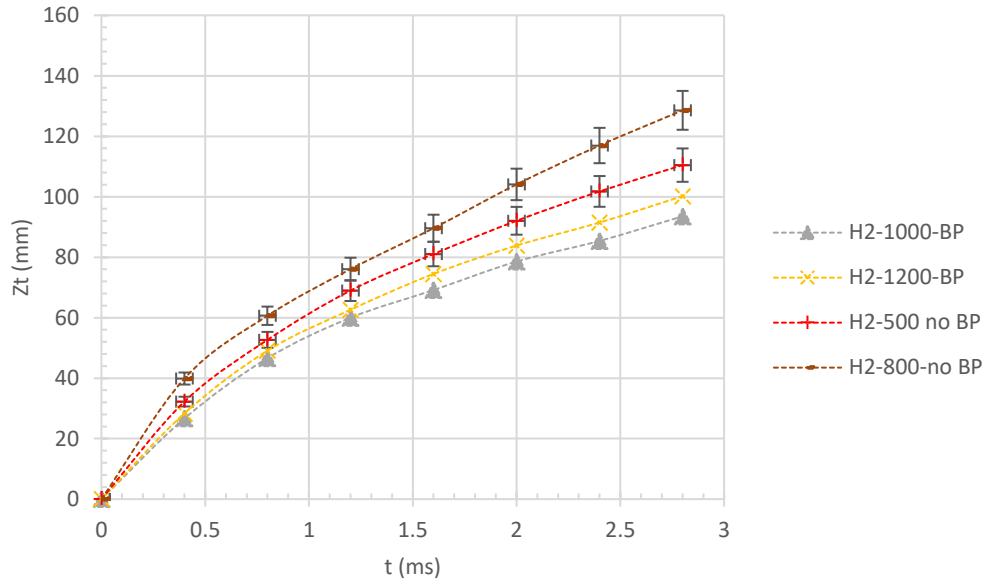


Figure 4-21- Penetration rate of H₂ at atmospheric and increased back pressure (250 kPa(abs))- the numbers represent the injection pressure in kPa(g)

Moreover, plotting $z'_t / \left(\frac{\dot{M}_n}{\rho_{ch}} \right)^{1/4}$ for hydrogen injection at 800, 1000, and 1200 kPa(g) versus the square root of time is shown in Figure 4-22. The slopes for these plots vary between 2.55 to 2.605. The reason that the slope of this plot with back pressure is lower than the similar graph for hydrogen with atmospheric back pressure is that the penetration rate and NPR are overall lower for injections with BP. Also, momentum rate is increased due to higher injection pressures which causes the value of $z'_t / \left(\frac{\dot{M}_n}{\rho_{ch}} \right)^{1/4}$ to decrease even though the chamber density is higher. If the first 10 frames of the jets' development (where the nozzle pressure is not stabilized and the gas is filling up the nozzle) from the experimental data plotted in Figure 4-22, the normalized penetration shows a better fitted linear relationship with the square root of time shown in Figure 4-23.

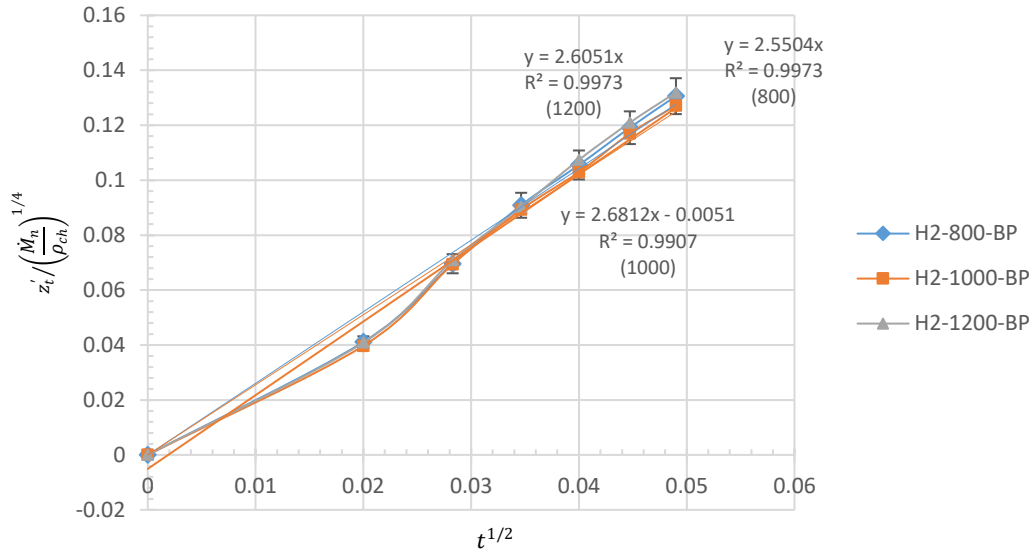


Figure 4-22- Plotting experimental data according to Equation 4-2 (H₂ with increased BP- 250 kPa(abs))- the numbers represent the injection pressure in kPa(g)

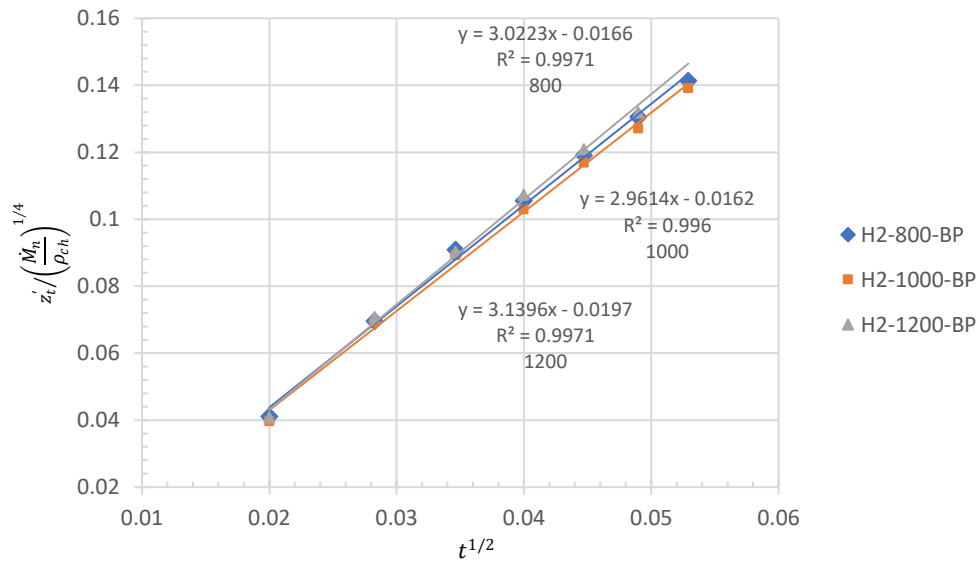


Figure 4-23- Excluding the irregularity in the first 10 frames of the jets' development from the Figure 4-22

4.2.4. Spread Angle

The spread angle is an important property of combustible gas jets because it affects the mixing and ignitability of the gas jets with regard to the location of the ignition source. The ignition source will likely be located in the periphery of the jet. The spread

angle defines the boundaries of the jet and if this is a function of gas composition, then the point at which ignition occurs is also dependent on the composition and injection properties. In this section, the spread angle of hydrogen and methane jets are presented and discussed. Earlier, for a qualitative comparison, images of hydrogen and methane jets were displayed in Figure 4-13 at the same time intervals and same injection pressure of 800 kPa(g). It was clear that the volumetric growth of hydrogen jets is sensibly greater than that of methane jets although the penetration rates, as it was suggested by Figures 4-15 and 4-16, have similar values at constant injection pressure. It was suggested Figure 4-13 that the spread angles of hydrogen jets are wider than the methane jets which is expected from the theory due to lower density of hydrogen and higher diffusivity of this gas. In this section, the spread angles are quantified for H₂, CH₄ and their blend jets (containing 20% H₂ by energy content and 46% H₂ by mole content) over a range of injection pressures (Figure 4-24 and 4-25). In Figure 4-24, the spread angles of hydrogen, methane and the blend of them with increased back pressure (250 kPa (abs)) are presented. The spread angle of hydrogen jets is between 4-6 degrees greater than those of methane jets. The blend behaves more toward the hydrogen behavior in terms of the angle. The values in all cases have an overall rising trend with increasing the injection pressure. This originates from higher mass and momentum in higher injection pressures considering the conservation of mass and momentum and entrainment of air into the jet.

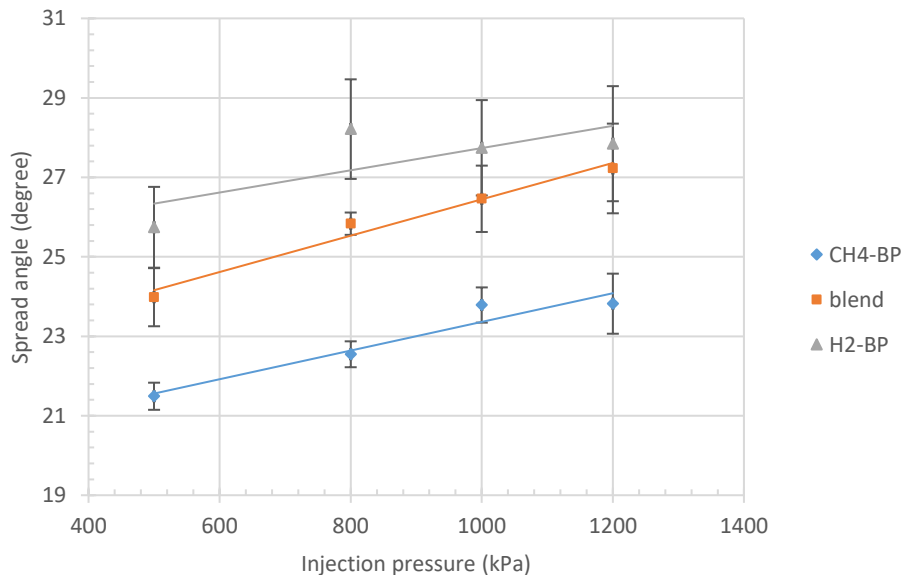


Figure 4-24- Spread angle of H₂, CH₄, and their blend with increased BP (250kPa(abs))

To highlight the role of back pressure on the spread angle, Figure 4-25 displays the spread angle of hydrogen and methane jets under atmospheric and increased BP conditions. This plot suggests that increasing back pressure enhances the angle due to the more resistance against the flow. For methane, although the angle does not change much in atmospheric BP, the jet tends to develop wider with increased BP. The reason that the back pressure overall rises the spread angle is that with the elevated back pressure reduces the penetration rate as it was discussed in the previous sections. As a result of reduced penetration rate, conservation of mass and momentum makes the gas to expand in the radial direction. Figure 4-26 shows a hydrogen jet spreading under atmospheric and increased back pressure (250 kPa(g)) with similar injection back pressure. As this figure suggests, increased back pressure makes the jet penetrating with a wider angle. This effect enhances the mixing properties in the gas jets penetrating in the environments with increased back pressures.

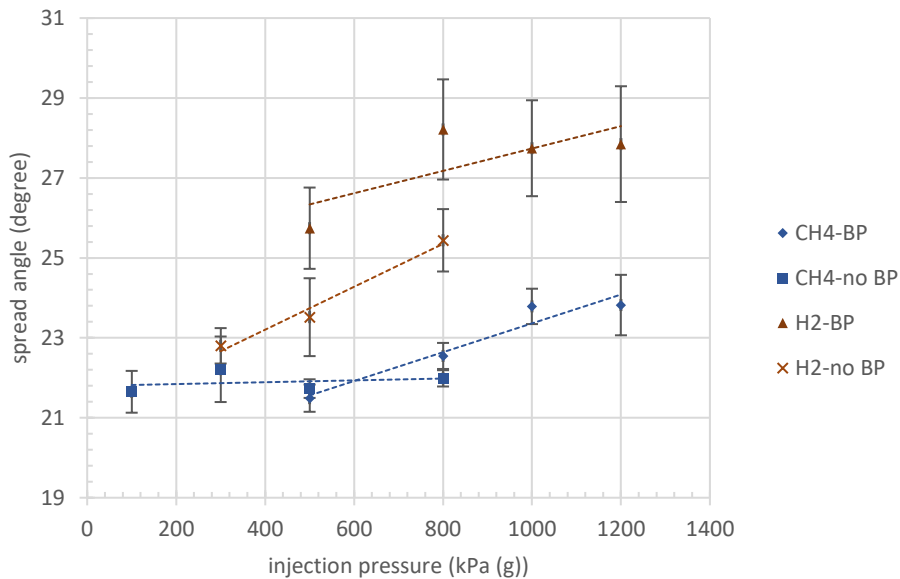


Figure 4-25- Spread angle of methane and hydrogen jets with (250 kPa(g)) and atmospheric BP

Overall, the spread angle of the gas jets is critical regarding the mixing and ignitability of the jets with different compositions and various injection conditions. Jets with wider spread angles tend to have improved mixing properties with the air due to higher surface contact area with the surrounding environment. Spread angle of the gas jet in relation to the gas type and composition and injection parameters should be considered when it comes to defining the location of the ignitors with regard to the jets.

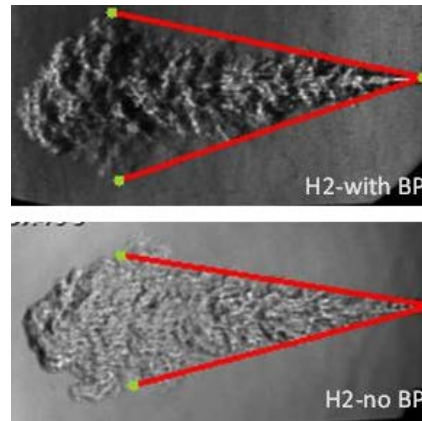


Figure 4-26- Effect of back pressure on the spread angle

4.3. Characteristics of Jets Regarding NPR

To find a correlation between all injection experiments and to exclude the injection pressure and back pressure from the variables, the penetration at a certain time after apparent start of injection can be plotted against the NPR. Nozzle pressure ratio is the driving force of the injection process, and it affects the jets properties significantly. In previous graphs, the role of NPR has been hidden in the form of the gas momentum rate and chamber density (which both affect the NPR). In fact, NPR has been existed in the Equation 2-5. Plotting the information versus NPR allows to see the effect of NPR in penetration rate highlighted. Figure 4-27 shows this plot with measured values of Z_t and calculated values of NPR at 2 ms after the start of the injection. The reason to plot the penetration length at 2 ms is that at this time it is past the point where the jet is fully developed but before the jet tip for any of the cases leave the viewing area. This Figure suggests that penetration of the gases under the experiments follow a similar trend with NPR although they have differences in terms of their type and composition, the injection pressure and back pressure. The effects of injection pressure and back pressure are hidden in NPR when the data are plotted this way. In fact, this graph suggests that the value of NPR (at least for the gases that have been characterized in this research) solely can define the penetration length of the gas at a certain time following this trend. It seems that the effect of the gas type and composition is minimized because the effects of composition on momentum rate have shown to be negligible.

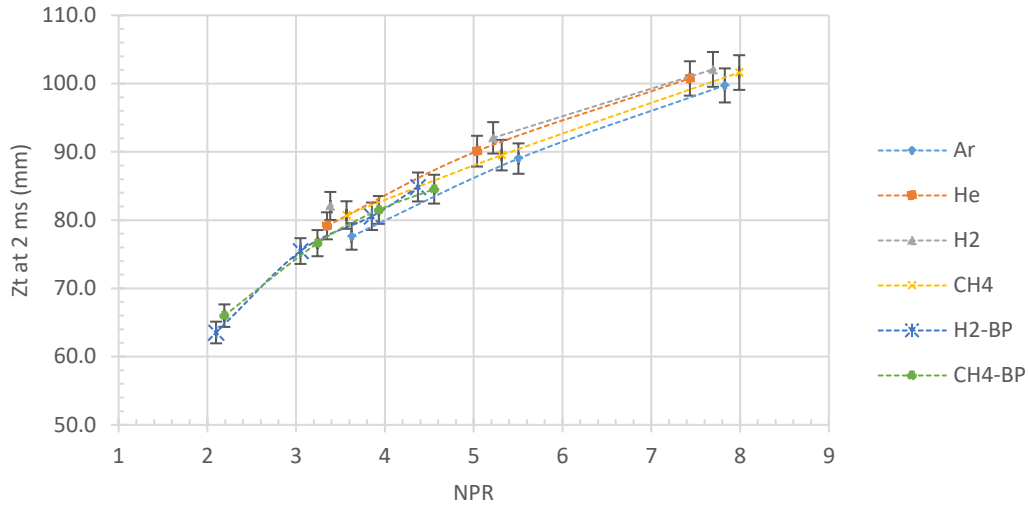


Figure 4-27- Zt at 2 ms for all injection experiments versus NPR

4.4. Gas Jets Momentum Rate Characteristics

As discussed in the previous sections, momentum rate of the gaseous jets is an important parameter to characterize the behaviour of the jets. In this section momentum rate of the jets normalized by the chamber density are characterized with respect to the NPR in Figure 4-28. The NPR values are characterized based on the properties of each individual gas after undergoing isentropic process within the nozzle. It is worth mentioning that the gases of experiments are all choked under these conditions. The ones that have not been choked (according to Table 4-2 and 4-4) are excluded from the rest of the characterizations because the calculations have been conducted with choked flow assumptions. The linear relationship between the momentum rate of the jet and the NPR allows extrapolation of momentum rate at any given combination of nozzle and chamber pressure. The lines for the momentum rate of hydrogen and methane follow each other in the back pressure and no back pressure conditions (the green line and the yellow line for methane and the blue and grey line for hydrogen). This is because the momentum rate value depends only on the upstream settings due to the choked flow conditions and is independent of the chamber pressure. In the theories discussed in the literature review and earlier in this chapter, the importance of the momentum rate was highlighted as the only characteristic from upstream of the jet that affects the penetration rate. The reason to divide the momentum rate by the chamber density on the ordinate axis is to consider the effects of the chamber density as well. Having the momentum rate at any injection pressure can be used in Equation 2-5 to estimate the penetration length of the jet. In

addition to the critical role of the gas momentum in injection characteristics, this property impacts the turbulence, mixing, and potentially the strain rate on the gas jet eventually affecting the ignitability of the fuel jets under different conditions.

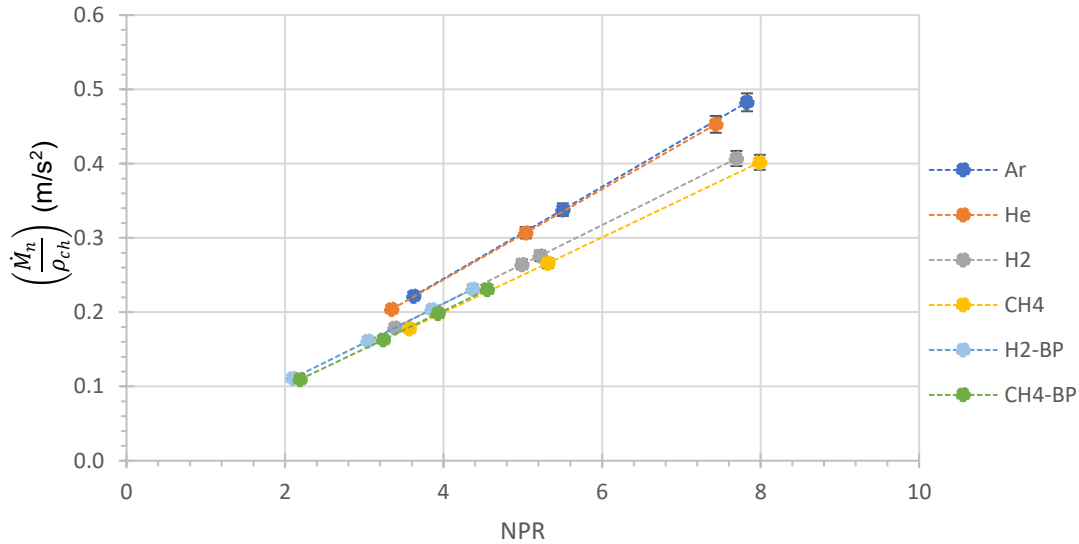


Figure 4-28- Exit momentum rate of gases vs NPR in atmospheric and increased BP (250 kPa(g))

4.5. Ignition Characteristics of Hydrogen and Methane Jets

Physical penetration and characteristics of the jets have been discussed earlier in the chapter. The discussions around the injection characterization including the penetration rate and spread angle are of great importance in conjunction with the ignition event. The timing of the jet's arrival on the ignitor surface and forming a combustible mixture with the air directly affect the timing and repeatability of the ignition and is crucial for a stable combustion in an engine. In this section, ignition characteristics of the jets of hydrogen, methane, and their blend (46% on a molar basis equal to 20% on an energy basis and 9.5% on a mass basis) in contact to a hot surface are discussed quantitatively and quantitatively. A hot surface (a commercial NGK CZ104 glow plug as presented in the methodology) is placed in contact with the jet with 44 mm distance from the tip of the nozzle. As the jet travels toward the ignitor, it mixes with the air and starts interacting with the ignitor as it reaches the hot surface. Mixing both happens during the free jet phase and as the jet impinges on the hot surface. Part of the ignition delay is associated with the traveling time and mixing that includes the physical aspects of ignition delay.

On the other hand, there are chemical delays attributed to developing necessary ignition precursors required to initiate combustion. If a combustible mixture has enough residence time in the vicinity of the ignitor to get enough energy to dissociate the molecules and initiate the exothermic reactions, then the ignition starts. Ignition delay, composed of physical and chemical delays, is defined as the time between the start of the injection (when the jet tip is appeared) and the start of the ignition and is quantified for the fuel jets injected at different conditions in this research. Figure 4-29 (a) shows the positioning of the glow plug against the nozzle and the traveling jet. As the jet impinges the surface, it creates eddies behind it, reducing velocity and mixing hot air into the jet. The impinging jet finds some residence time around the ignitor, the heat starts to transfer, and the hot air around the ignitor gets mixed with the jet (Figure 4-29 b). When all the physical and chemical requirements are present, the ignition starts. The start of ignition/combustion is interpreted from the images as the time that a propagating dark area appears on the image and spreads throughout the area (Figure 4-29 c and d). A few frames after that initial glow confirms that the dark area appeared on the image is the start of a propagating flame (Figure 4-29 d). Ignition characteristics including the ignition delay are examined by investigating the images obtained from the visualization approach as described earlier.

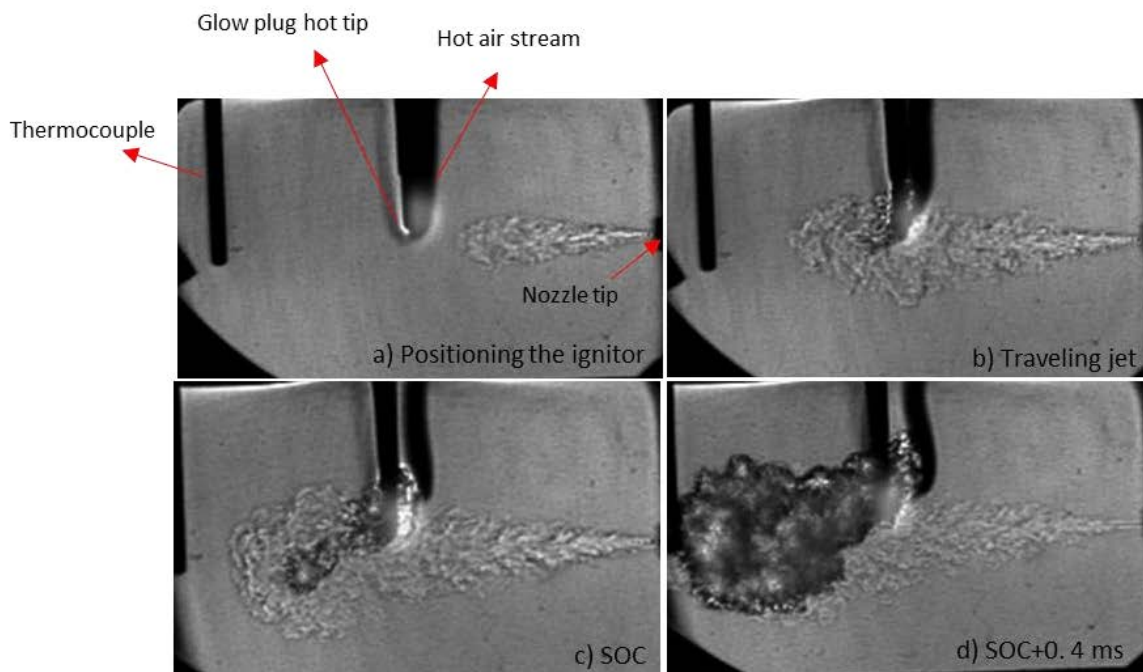


Figure 4-29- traveling jet and the position of the jet and the ignition source (a), traveling jet (b), start of combustion (c)- 10 frames after SOC (d)

4.5.1. Ignition of H₂ Jets

Hydrogen jets are injected at different injection pressures in atmospheric and increased back pressure (250 kPa(g)) conditions into the chamber. Ignition delay is quantified by the number of frames between the start of injection (SOI) and start of ignition/combustion (SOC). The tests are running at 25000 frame per second, so each frame equals 0.04 ms. The start of injection is referred to the moment where the first appearance of the jet is visible on the image. The SOC is defined on the basis of the appearance of the flame in the schlieren imaging. Chemical Reactions are occurring in advance, and an apparent energy release rate/increase in pressure might not align perfectly with this. But as we are looking at density gradients (and not light emissions) the thermal and chemical changes in the fluid are observed in the images before the SOC (Figure 4-30 a,b,c). When the darker appeared area starts to grow fast, the exothermic reactions are occurring (Figure 4-30 c). After the start of combustion, more mass and momentum of the jet gets involved in the ignition and the flame grows and propagates (Figure 4-30 e-l). Figure 4-30 belongs to H₂ injection at 1000 kPa(g) with 250 kPa(g) back pressure as a representative, and the pattern of the start of ignition and propagation is similar in other pressures.

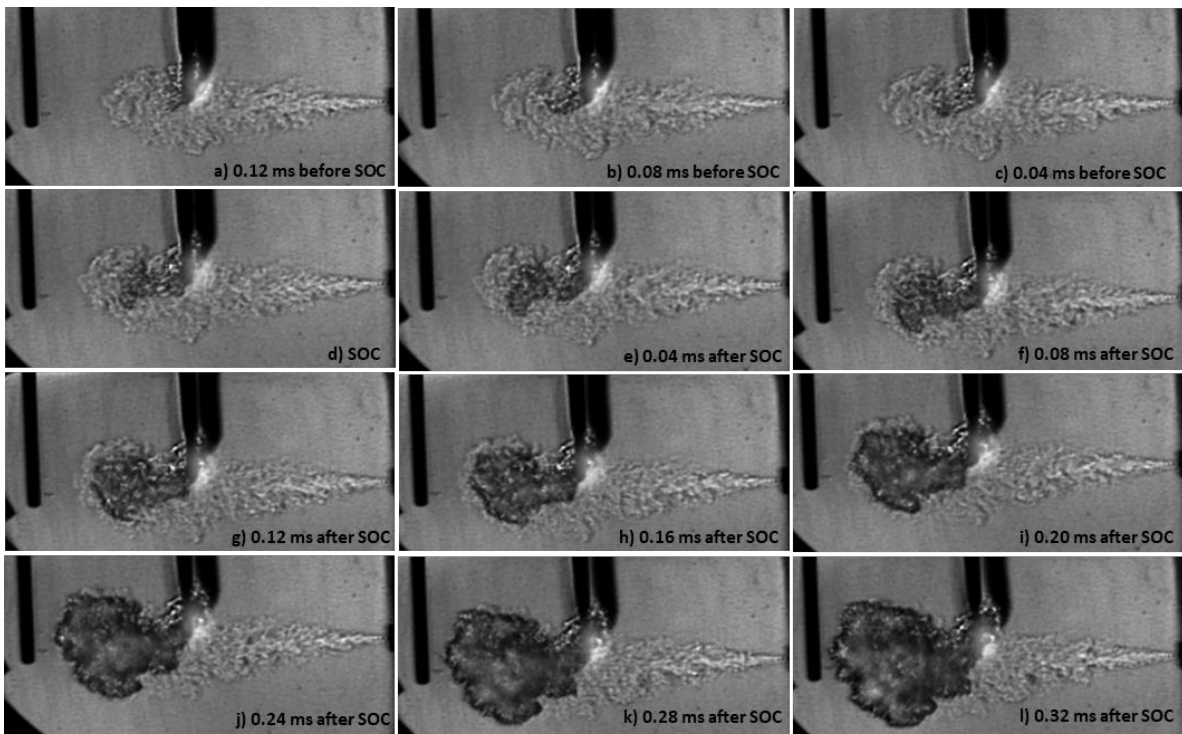


Figure 4-30- H₂ jet traveling to the hot surface and sequences of the jet behaviour before ignition, at the start of combustion (SOC), and after ignition, for a jet injecting at 1000 kPa(g) and 250 kPa(g) back pressure

While Figure 4-30 focuses on the frames right before and after the ignition event to evaluate the jets' behaviour with a closer look around the ignition moment, Figure 4-31 shows the start of the ignition and the flame propagation throughout the body of the jet at 1200 kPa(g) injection pressure in longer time frames. . As it can be seen in the images, the ignition kernel appears in the vicinity of the ignitor, where the gas gets enough thermal energy to start the chemical reactions associated with the ignition while the injection is still occurring. The ignition process involves several reactions that must occur and many of them are endothermic. So, when the gas gets enough thermal energy in the vicinity of the ignitor, the initial decomposition reactions start to happen leading to the further exothermic reactions. For H_2-O_2 reactions to occur, both H_2 and O_2 needs to be decomposed and form OH radicals before forming H_2O . Prior to that, 3-body reactions are present that drive the formation of HO_2 intermediate which has multiple pathways to OH and then H_2O [79]. According to Figure 4-31, the ignition seems to be starting on the back side of the ignitor where the gas has more residence time to get thermal energy with lower shear stress leading to less dissipation of the thermal energy.

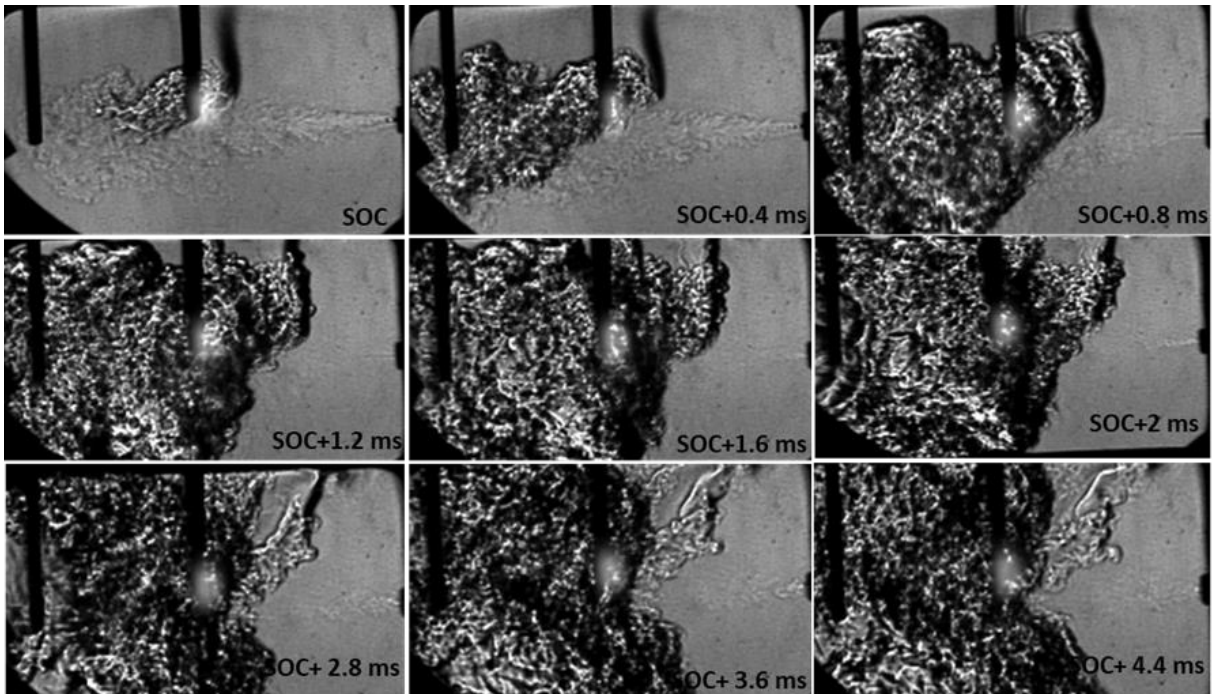


Figure 4-31- Ignition and flame propagation of hydrogen jets at 1200 kPa(g) injection pressure and atmospheric back pressure with 2.5 ms injection duration

After the initial start of the ignition reactions, the ignited gas propagates in the direction of the jet and spreads toward the edges to engage the unburned fuel. Images shown in Figure 4-32 to compare ignition of hydrogen in atmospheric and increased back pressure show that the flame movement is not only in the direction of the jet, but it also propagates back up the jet with increased back pressure. Having back pressure in the chamber not only affects the ignition delay (both the transport delay and chemical reactions), but it also affects the formation and propagation of the flame (Figure 4-32).

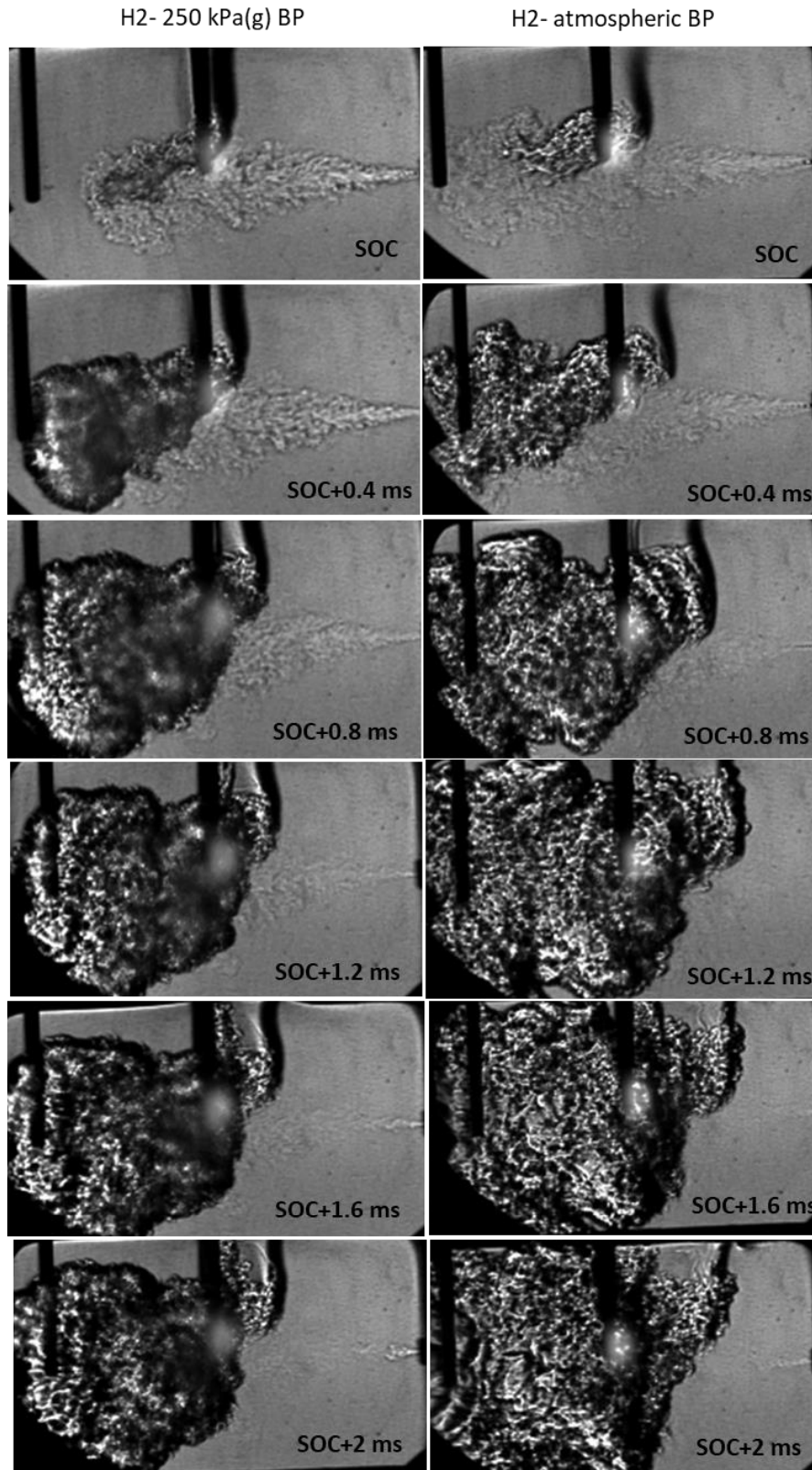


Figure 4-32-H₂ jet ignition with atmospheric and increased back pressure at 1200 kPa(g) injection pressure

In order to determine the effect of injection pressure on the ignition delay, this parameter has been quantified over a range of injection pressures in atmospheric and increased back pressure (Figure 4-33). For each condition, the experiment have been repeated five times and the reported values are the average of the obtained amounts. Ignition delay is composed of the physical transport and mixing time plus the chemical reactions' formations. The transport time decreases by increasing the injection pressure (as it was discussed in the injection characteristics). Also, by increasing the injection pressure, the gas kinetic energy (momentum) rises around the ignitor with greater kinetic energy at the edges of the jet. According to Figure 4-33, the overall trend for ignition delay is decreasing by increasing the injection pressure. The reason for that is probably related to the enhanced turbulent mixing as a result of higher injection pressure which also affects the spread angle that enhances the fuel contact with the air. However, the turbulent mixing cannot be quantified with schlieren imaging. Figure 43 also shows the ignition delay comparison of hydrogen at different injection pressure at atmospheric and increased back pressure. This plot suggests that overall, chamber pressure decreases the ignition delay which originates from the effect of pressure on the 3-body reactions that from the intermediates and are sensitive to pressure. Increased back pressure promotes these rate-limiting steps leading to reduced ignition delays.

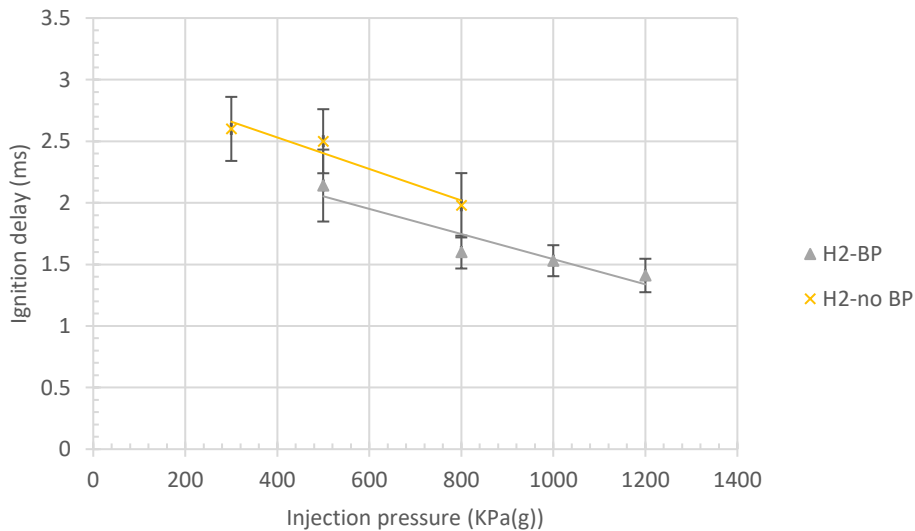


Figure 4-33- Ignition delay of hydrogen over a range of injection pressures-atmospheric back pressure

Also, from the injection characteristics, we know that the penetration rate increases as the injection pressure increases and decreases as the receiver pressure increases. If the traveling time is excluded from the overall ignition delay, the ignition delay related to the mixing and chemical reactions can be compared (Figure 4-34). This Figure shows that the chemical delay associated with injection of hydrogen at 300 and 500 (kPa(g)) are similar, although the decrease in the ignition delay at 800 kPa(g) is observed due to the higher mixing rate at this pressure. The values are the average of 5 ignition delay results.

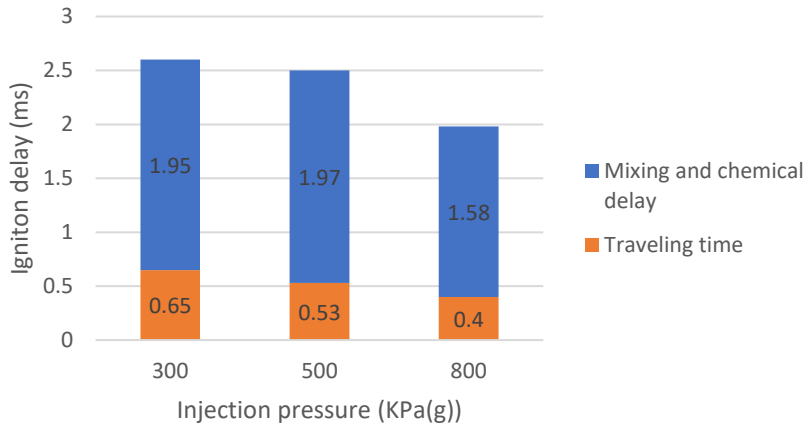


Figure 4-34- Traveling time and chemical delay share in total ignition delay for hydrogen injection with atmospheric BP

For hydrogen ignition with BP, again, the traveling time is excluded from the overall ignition delay for ignition of hydrogen with back pressure (Figure 4-35). This figure suggests that the higher injection pressures do not seem to have a significant effect on the mixing and chemical delay. In fact, the gas passing the hot surface is mixing and heating up at the same time, so there are significant interactions between physical and chemical processes that are hard to differentiate. Also, it seems that increased back pressure improves the physical and chemical interactions involved in the hydrogen ignition process independent of the injection pressure.

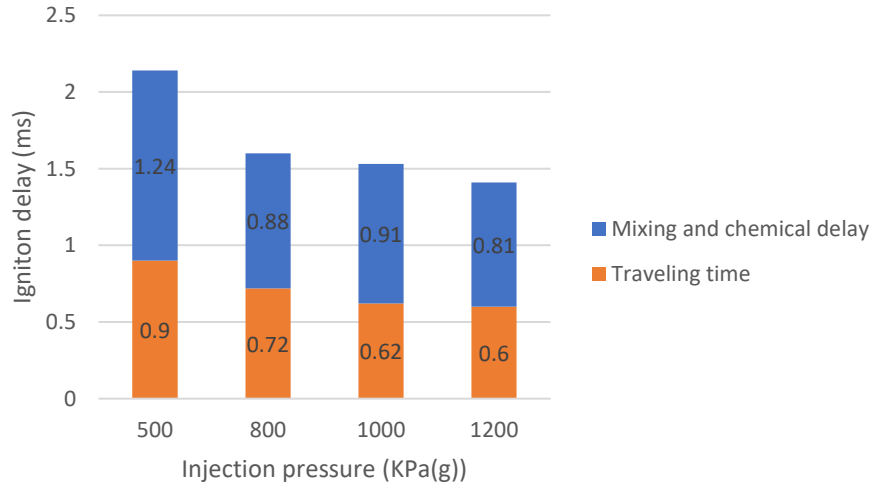


Figure 4-35- Traveling time and chemical delay share in total ignition delay for hydrogen injection with BP

4.5.2. Ignition of CH₄ Jets- Effect of Adding H₂ to Methane on Ignition

Although the ceramic glow plug used in these experiments successfully ignited hydrogen, its temperature is not sufficient for methane ignition. As discussed in the literature review, methane as a fuel is more difficult to ignite and a glow plug with higher surface temperature is required to provide the required ignition energy to ignite it. Typically, the minimum hot surface temperature to ignite methane is 1300 K and the conventional glow plugs normally run at lower temperature than this [51]. Methane jets as of Figure 4-36 impinging on the surface of the ignitor but do not ignite on a reasonable timescale.

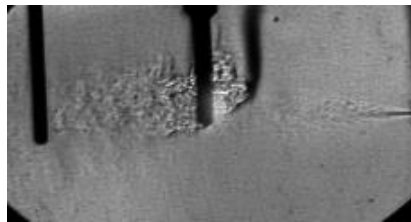


Figure 4-36- Methane jet impinging on the glow plug and not igniting

However, adding hydrogen to methane is proved to improve its ignitability and ignition properties of methane. In these experiments, hydrogen is added on the basis of 20% energy content which equals to 46% on a molar basis, and 9.5% on a mass basis.

Mixing gases are conducted based on the partial pressure approach described in the methodology.

Figure 4-37 plots the ignition delay of hydrogen and the blend over a range of injection pressures with increased back pressure. For each condition, the ignition test has been repeated three times and the average values have been plotted with standard deviation error bars. The error bars are large in some data points which originate from the stochastic nature of the ignition event. Variability is highest at the low injection pressure due to more uncertainty in mixing or ignition chemistry in lower pressures. The stochastic nature of the interactions between chemistry and turbulent jet flow in the vicinity of the ignitor makes this more variable. Figure 4-37 suggests that the ignition delay of hydrogen and the blend have similar values and confirm that the hydrogen dominated the ignition event and promotes the ignition of the blend very similar to pure hydrogen.

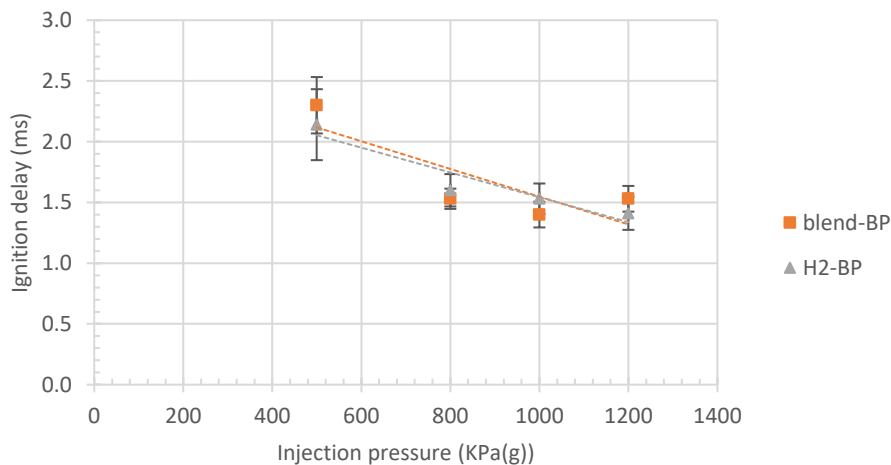


Figure 4-37- Ignition delay of hydrogen and the blend

Figure 4-38 demonstrates the effect of back pressure on the ignition delay for the H₂-CH₄ blend over a range of injection pressures. Similar to pure hydrogen, increased back pressure and increased injection pressure reduce the ignition delay of the blend.

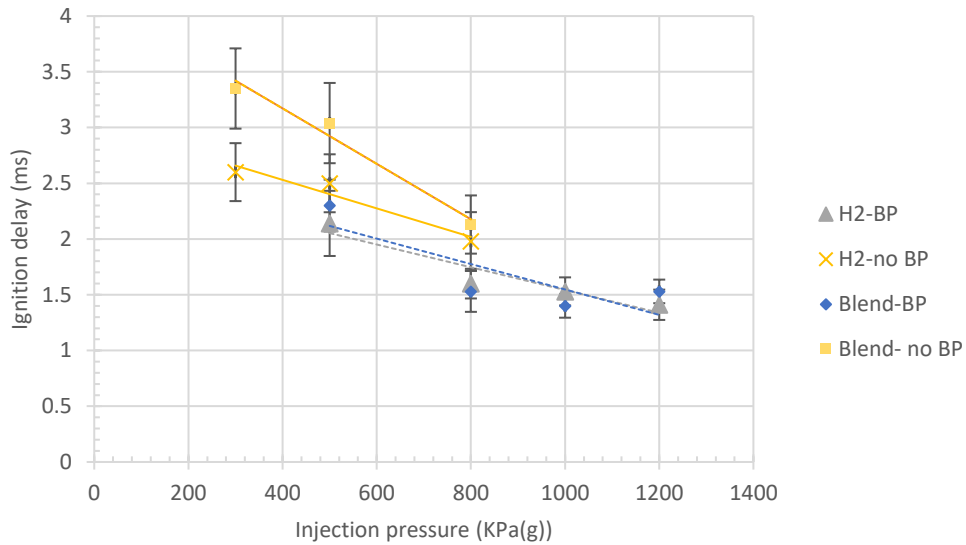


Figure 4-38- Ignition delay of the blend with and without BP

Excluding the travel time from the total ignition delay in ignition tests with atmospheric and increased back pressure, leaves the mixing and chemical delay to compare (Figure 4-39 and 4-40). This comparison shows that although the traveling time for increased back pressure is more, the mixing and chemical reaction time is significantly reduced compared to the cases with atmospheric back pressures.

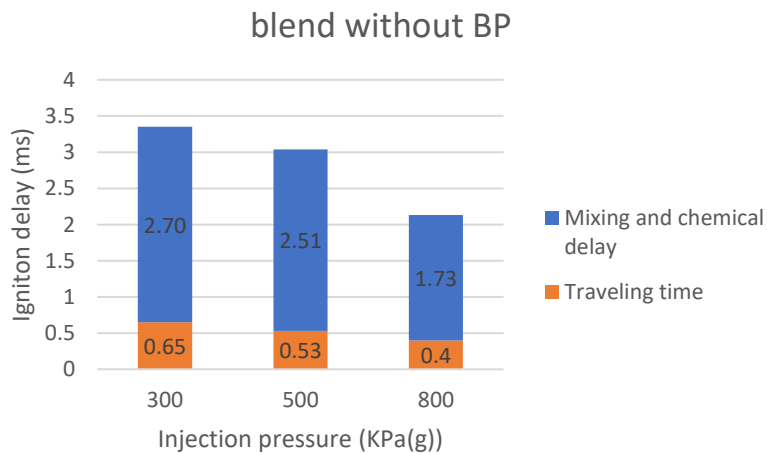


Figure 4-39- Traveling time and chemical delay share in total ignition delay for H₂-CH₄ blend injection with atmospheric BP

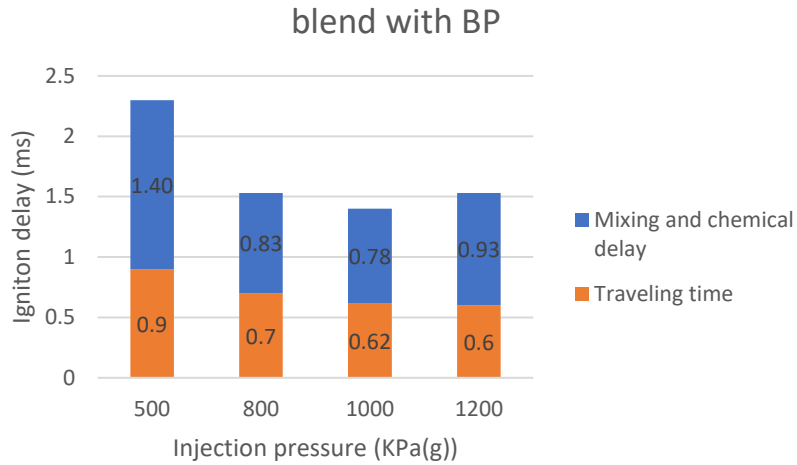


Figure 4-40- Traveling time and chemical delay share in total ignition delay for H₂-CH₄ blend injection with increased BP

Figure 4-41 shows the ignition event for the blend of hydrogen and methane at 1200 kPa(g) injection pressure and 250 kPa(abs) back pressure. The comparison of the ignition of hydrogen and the H₂-CH₄ (46% molar hydrogen content) blend suggest that under the same conditions, hydrogen dominates the ignition of the blend under the circumstances of the experiment. It is noticeable from Figure 4-41 that the formation of the kernel, the ignition timing, and the propagation of the flame seem to be similar in these two ignition events.

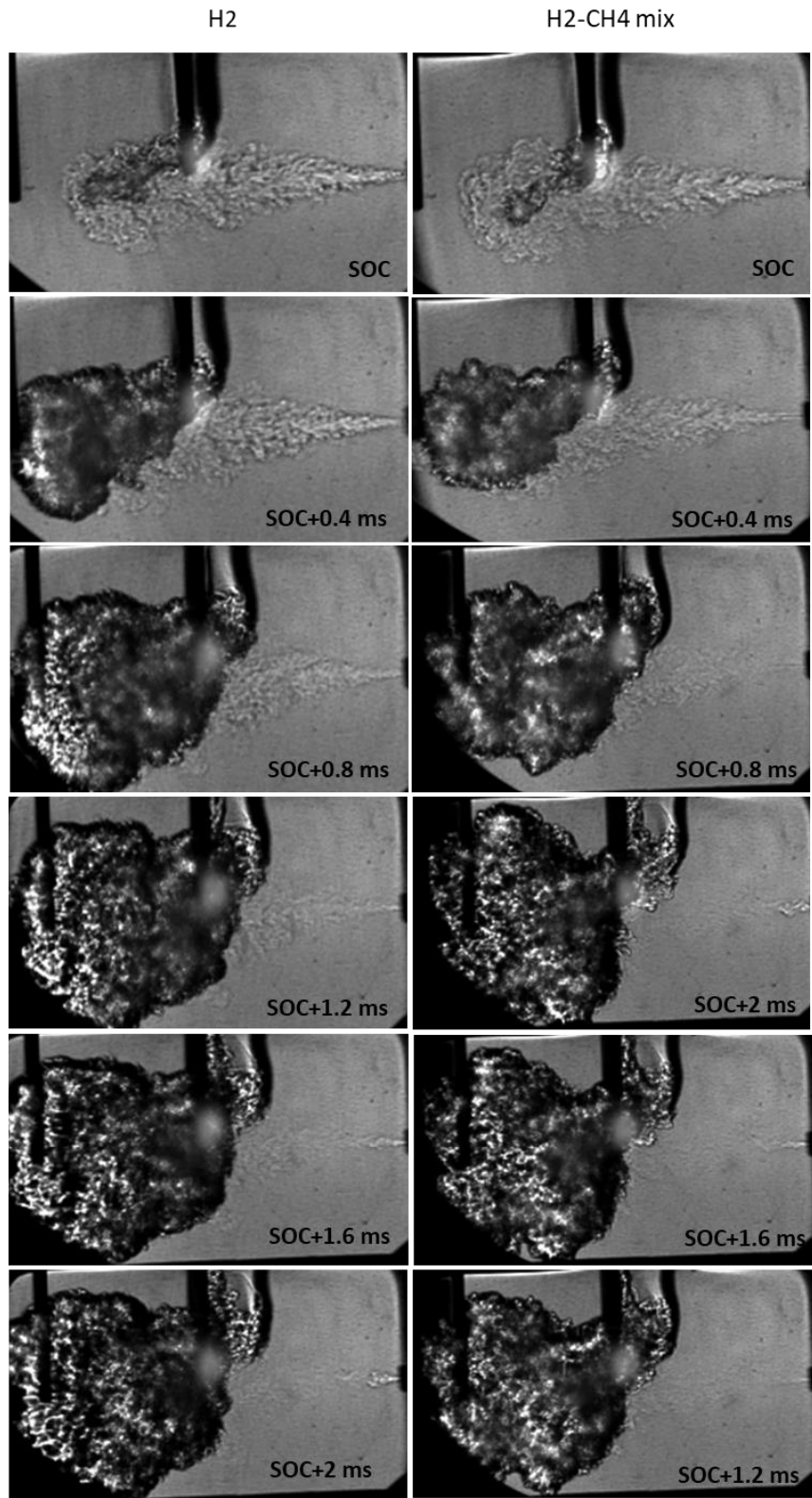


Figure 4-41- Ignition of the blend of hydrogen and methane with 1200 kPa(g) injection pressure and 250 kPa(g) back pressure

As a final conclusion from the ignition of H₂ and H₂-CH₄ blend, Figure 4-42 displays the delays including mixing and chemical delay of all cases (the traveling time has been excluded). This figure suggests that overall increasing the injection pressure has decreased the mixing and chemical delay share in the total ignition delay. This probably originates from enhanced turbulent mixing in higher injection pressures. However, it is important to note that this finding may not be true for increased injection pressure to higher values. Further increase in injection pressure may have an adverse effect on the ignition delay by limiting the residence time of the jet in the vicinity of the ignitor and by quenching the hot air around the ignitor due to excessive momentum of the jet. Another finding suggested by this plot is that increased back pressure has reduced the ignition delay related to mixing and chemical delays which is likely due to the positive effect that the increased pressure has on the formation of chemical substances that promote the ignition reactions.

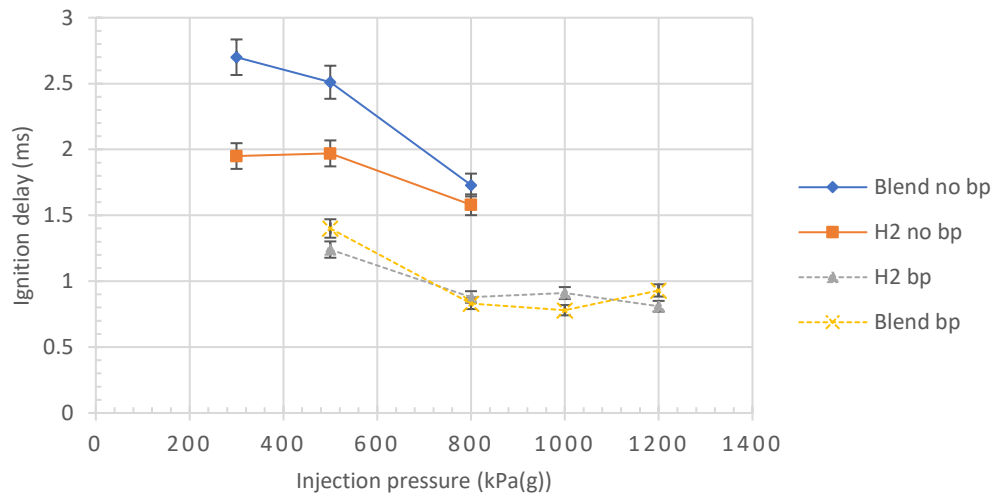


Figure 4-42- Mixing and chemical delay versus injection pressure for H₂ and H₂-CH₄ (20% E-46% molar) blend

A summary of the conclusions from the results chapter, the research limitations and future recommendations are discussed in the next chapter.

Chapter 5. Conclusions, Limitations, and Future Work Recommendations

5.1. Summary of the Research

The aim of this research to study the injection and ignition characteristics of gaseous fuel jets was fulfilled through experimental approaches supported by theoretical analysis. In this work the effects of injection parameters including the injection pressure, back pressure, and gas type and composition on the jets' properties including the axial and radial penetration rate, velocity, and momentum rate were examined through a set of designed experiments and theoretical evaluations. An experimental system composed of gas supply and mechanical components, data acquisition and control systems, schlieren visualization system and high-speed imaging was designed and set up for the purpose of this research. An optical chamber was designed and built for the experiments with increased back pressure and ignition tests. Argon and helium and a 50% (molar) mixture of them were chosen as the non-combustible gases to operate the system and analyse fundamentals of the gas injection through this structure. Combustible gases of hydrogen and methane and a 20% by energy H_2 in CH_4 (46% by moles) were then evaluated in terms of injection properties into the atmospheric and increased back pressure receiver. In addition to the jets axial and radial penetration obtained from the visual assessment, some of the jets' key fluid properties including the mass flow rate, momentum rate, and velocity were characterized using the supported theory and fundamentals of the jets flow. In connection with the assessed jets physical properties, the ignition characteristics of the combustible jets including the ignition delay of the jets issued under various injection pressure and back pressure was evaluated and quantified.

5.2. Conclusions and Implications

The key findings are discussed in two parts of injection and ignition. The implications in engine applications are also discussed in the following.

5.2.1. Conclusions on Injection Characteristics

- The axial penetration length of the gas jets that were experimented in this research show significant dependency on the injection pressure in atmospheric pressure receiver. By increasing the injection pressure, the penetration rate is increased accordingly. This trend is observed in all the tested gases and their mixtures.
- Increasing the injection pressure, increases the mass flow rate for a given injection duration and fuel blend, and consequently enhances the momentum rate associated with each injection condition. Momentum rate, as the single parameter representing the upstream flow in the established equation for the jets penetration length (Equation 2-5) is measured and characterized for each gas type and each injection condition. The momentum rate of gases shows linear relationship with the static pressure in the nozzle in all conditions.
- Nozzle pressure ratio (NPR) was found to correlate directly with jet penetration, independent of the fuel type/composition, injection pressure and back pressure. NPR is characterized for different gas types and injection conditions in atmospheric and increased back pressure. Plotting the penetration length of all injection cases versus NPR (Figure 20) suggests that penetration of these gases under the experiments follow a similar trend with NPR although the jets were different in terms of type and composition, injection pressure and back pressure. In fact, this graph suggests that the value of NPR (at least for the gases that have been characterized in this research) solely can define the penetration length of the gas at a certain time following this trend.
- Established under-expanded jet theory suggests that the normalized penetration $z'_t / \left(\frac{\dot{M}_n}{\rho_{ch}} \right)^{1/4}$ is expected to have a linear relationship with the square root of time, with an approximate slope of 3. During the developing phase, within the first 10 frames (the first 0.4 ms), this relationship is not linear which originate from the fact that the nozzle is being filled up in the first few moments, the static pressure in the nozzle is not stabilized yet, and the jet development is progressing. However, after the jet is fully developed, the linear dependency is governed with higher accuracy. The slope was on the order of 2.6-3 when

the initial development was included but increased to approximately 3.3 when considering only the fully developed phase of the jet. Another conclusion from this evaluation is that the normalized gas jets penetration follows a similar trend with the square root of time independent of the gas type and composition.

- The radial penetration is represented by the spread angle which is measured using the images obtained from the jets. The spread angle evaluation leads to this conclusion that the spread angles are a function of both injection pressure and gas composition, and overall, increasing the injection pressure enhances the spread angle and promotes the radial penetration (or volumetric growth). This originates from higher mass and momentum in higher injection pressures considering the conservation of mass and momentum and entrainment of air into the jet. This pattern is observed more for He and H₂ (compared to Ar and CH₄) due to their lower density and tendency to spread more in the radial direction as they eject. H₂ jets compared to methane jets, have wider spread angle and wider angles lead to larger volumetric growth which enhances the area of contact with the air. On the effects of back pressure on the spread angle, the results suggest that increasing back pressure enhances the spread angle. The reason for this is that the elevated back pressure reduces the penetration rate, as a result of reduced penetration rate, conservation of mass and momentum makes the gas to expand more in the radial direction.

5.2.2. Conclusions on Ignition Characteristics

- An important conclusion regarding the ignition characteristics is that although the increased back pressure impedes the physical transport of the gas jet to the surface of the ignitor, higher pressures are known to promote three-body reactions that can increase the intermediate reactions in the ignition reaction. Apart from the back pressure, increasing the injection pressure reduces the physical traveling delay of the jets and it would be expected to improve turbulent mixing by increasing the momentum. However, it does not show a consistent measurable effect on the thermo/chemical delay side of the ignition under different conditions.

- Although the methane gas jets are not ignitable (at least within a reasonable ignition delay) using the hot surface used in these experiments, addition of hydrogen is proved to make a combustible mixture with short ignition delay. The molar fraction of hydrogen for these tests is 46% which is equal to 20% on an energy basis. This mixture shows similar ignition delay time and similar ignition start and propagation pattern to pure hydrogen and it seems that the hydrogen is dominating the mixture in terms of ignition.

5.2.3. Implications for Engine Applications

- As it was demonstrated through the introduction and the literature review, the direct injection engines offer higher efficiency compared to premixed fueled engines, especially at part load where throttling can be avoided. Gaseous fuel DI engines need an ignition source for a consistent and reliable ignition in all conditions. Ignition of the jet depends on the right mixture fraction at the right location, as a result it depends on the jet's properties. In this research injection and ignition characterization of the jets are studied. Although the pressures and temperatures used in these characterizations differ from the engine like conditions, there are important findings that can be connected to real engine applications.
- The momentum rate has been proved to be an important factor to predict the penetration of the jet. The momentum rate characterization based on NPR can be extrapolated to the pressure ranges beyond the tests' conditions toward the engine like conditions. Subsequently, the momentum rate value can lead to obtaining the penetration length using the Equation 2-5. In addition to the critical role of the gas momentum in injection characteristics, this property impacts the turbulence, mixing, and potentially the strain rate on the gas jet eventually affecting the ignitability of the fuel jets under different conditions.
- NPR is proved to be an important factor affecting the jets properties. The NPR range in these characterizations can have similarities to the engine like NPR conditions. Both the injection pressure and cylinder pressures are higher in engine like conditions, but their ratio can have overlaps with the NPR range of these experiments. The jets' penetration has been characterized based on

NPR. The trend found in this regard is also useful for extrapolating data to estimate the penetration length beyond the experimental data points at any given NPR. Therefore, the effects of NPR can be scaled to higher pressures.

- The evaluation of the spread angle of the gaseous fuels showed wider volumetric growth for hydrogen jets compared to methane. Also, the spread angle increased with increased back pressure. Since mixing happens on the edges of the jet, this leads to improved mixing which is of great importance when it comes to jets ignition. This finding can be useful in designing the ignition assist configuration in DI engines with alternative fuels.
- Results are useful in developing understanding of the jets dynamics with regard to fuel composition, injection pressure, and back pressure. This understanding can be used to validate models that can be applied at higher loads.
- The dominant effect of hydrogen addition on the ignition behaviour of the H₂-CH₄ blend and the ignition delay dependence on the pressure are useful findings when it comes to engines operating on alternative fuels.

5.3. Research Limitations

Some of the limitations attributed to the conducted research include:

- The commercial injector that was used for the experiments is limited in terms of the injection pressure to the maximum pressure that was employed in the tests. Limitation on the injection pressure imposes constraints on the back pressure values to keep the NPR more than the critical pressure ratio to reach under-expansion and choked flow conditions at the nozzle throat.
- The blends were made based on partial pressure calculations in the sample cylinder which was calibrated based on the volume which can impose restrictions on controlling the concentration of the gas mixtures.

- The axial and radial penetration measurement was based on the user's visual inspection/ identification of the jet tip and the boundaries of the jet on the images using the camera software.
- The detection of ignition from the images was based on detecting the frame in which a visible darker area appears on the image as the kernel that starts the propagating flame.

5.4. Future Work Recommendations

The following additional work can be considered for the future:

- Increase pressure in the chamber to better represent engine conditions and verify the continued applicability of the NPR ratio (this will depend on having a higher-pressure injector as well)
- The concentration of the blends can be assessed with a gas chromatograph to ensure the concentration.
- An automated image processing can be employed to assess the penetration rate based on the images.
- A more automated method to identify the ignition can be employed that can work based on detecting a rise in the pressure in the chamber or detecting the start of ignition with image processing.
- Conducting CFD modelling for both cold and reacting flows to better understand gas jet mixing and interaction between the hot surface ignitor and the jet.
- A spark plug can be used as the ignition source to study the ignition of the jets
- Characterization the ignitability of the mixture based on the fraction of hydrogen is useful to study in future. Lower concentrations of hydrogen and its effect on the ignition of the hydrogen-methane blend can be studied.

References

- [1] Natural Gas Use, in Transportation, Implementation, and Committee, “Natural Gas Use in the Medium and Heavy-Duty Vehicle Transportation Sector, ROADMAP 2.0,” Canadian Natural Gas Vehicle Alliance, ISSN 978-0-660-29589-3, Jun. 2019.
- [2] D. Mumford, D. Goudie, and J. Saunders, “Potential and Challenges of HPDI,” presented at the 9th AVL International Commercial Powertrain Conference 2017, May 2017, pp. 2017-01–1928. doi: 10.4271/2017-01-1928.
- [3] M. Miller, “The feasibility of renewable natural gas as a large-scale, low carbon substitute,” p. 101.
- [4] M. Li, H. Wu, T. Zhang, B. Shen, Q. Zhang, and Z. Li, “A comprehensive review of pilot ignited high pressure direct injection natural gas engines: Factors affecting combustion, emissions and performance,” *Renewable & sustainable energy reviews*, vol. 119, pp. 109653–, 2020, doi: 10.1016/j.rser.2019.109653.
- [5] A. Thiruvengadam, M. Besch, V. Padmanaban, S. Pradhan, and B. Demirgok, “Natural gas vehicles in heavy-duty transportation-A review,” *Energy policy*, vol. 122, pp. 253–259, 2018, doi: 10.1016/j.enpol.2018.07.052.
- [6] “Alternative Fuels Data Center: Natural Gas Vehicles.” https://afdc.energy.gov/vehicles/natural_gas.html (accessed Sep. 23, 2022).
- [7] P. Dimitriou, T. Tsujimura, and Y. Suzuki, “Low-load hydrogen-diesel dual-fuel engine operation – A combustion efficiency improvement approach,” *International journal of hydrogen energy*, vol. 44, no. 31, pp. 17048–17060, 2019, doi: 10.1016/j.ijhydene.2019.04.203.
- [8] Z. Qin, Z. Yang, C. Jia, J. Duan, and L. Wang, “Experimental study on combustion characteristics of diesel–hydrogen dual-fuel engine,” *Journal of thermal analysis and calorimetry*, vol. 142, no. 4, pp. 1483–1491, 2020, doi: 10.1007/s10973-019-09147-y.
- [9] T. Tsujimura and Y. Suzuki, “The utilization of hydrogen in hydrogen/diesel dual fuel engine,” *International journal of hydrogen energy*, vol. 42, no. 19, pp. 14019–14029, 2017, doi: 10.1016/j.ijhydene.2017.01.152.
- [10] S. Imran, T. Korakianitis, R. Shaukat, M. Farooq, S. Condoor, and S. Jayaram, “Experimentally tested performance and emissions advantages of using natural-gas and hydrogen fuel mixture with diesel and rapeseed methyl ester as pilot fuels,” *Applied energy*, vol. 229, pp. 1260–1268, 2018, doi: 10.1016/j.apenergy.2018.08.052.
- [11] T. Gatts, S. Liu, C. Liew, B. Ralston, C. Bell, and H. Li, “An experimental investigation of incomplete combustion of gaseous fuels of a heavy-duty diesel engine supplemented with hydrogen and natural gas,” *International Journal of Hydrogen Energy*, vol. 37, no. 9, pp. 7848–7859, May 2012, doi: 10.1016/j.ijhydene.2012.01.088.
- [12] F. Yan, L. Xu, and Y. Wang, “Application of hydrogen enriched natural gas in spark ignition IC engines: from fundamental fuel properties to engine performances and emissions,” *Renewable & sustainable energy reviews*, vol. 82, pp. 1457–1488, 2018, doi: 10.1016/j.rser.2017.05.227.
- [13] S. Verhelst and T. Wallner, “Hydrogen-fueled internal combustion engines,” *Progress in energy and combustion science*, vol. 35, no. 6, pp. 490–527, 2009, doi: 10.1016/j.pecs.2009.08.001.

- [14] M. Li *et al.*, “Numerical investigations on pilot ignited high pressure direct injection natural gas engines: A review,” *Renewable & sustainable energy reviews*, vol. 150, pp. 111390–, 2021, doi: 10.1016/j.rser.2021.111390.
- [15] D. Sankesh and P. Lappas, “An experimental and numerical study of natural gas jets for direct injection internal combustion engines,” *Fuel (Guildford)*, vol. 263, pp. 116745–, 2020, doi: 10.1016/j.fuel.2019.116745.
- [16] I. Chitsaz, M. H. Saidi, A. A. Mozafari, and A. Hajjalimohammadi, “Experimental and numerical investigation on the jet characteristics of spark ignition direct injection gaseous injector,” *Applied energy*, vol. 105, pp. 8–16, 2013, doi: 10.1016/j.apenergy.2012.11.023.
- [17] H. L. Yip *et al.*, “A Review of Hydrogen Direct Injection for Internal Combustion Engines: Towards Carbon-Free Combustion,” *Applied Sciences*, vol. 9, no. 22, p. 4842, Nov. 2019, doi: 10.3390/app9224842.
- [18] A. Hamzehloo and P. G. Aleiferis, “Gas dynamics and flow characteristics of highly turbulent under-expanded hydrogen and methane jets under various nozzle pressure ratios and ambient pressures,” *International journal of hydrogen energy*, vol. 41, no. 15, pp. 6544–6566, 2016, doi: 10.1016/j.ijhydene.2016.02.017.
- [19] L. Allocca, A. Montanaro, G. Meccariello, F. Duronio, S. Ranieri, and A. D. Vita, “Under-Expanded Gaseous Jets Characterization for Application in Direct Injection Engines: Experimental and Numerical Approach,” SAE International, Warrendale, PA, SAE Technical Paper 2020-01–0325, Apr. 2020. doi: 10.4271/2020-01-0325.
- [20] . S. and R. A. Bakar, “A Technical Review of Compressed Natural Gas as an Alternative Fuel for Internal Combustion Engines,” *American J. of Engineering and Applied Sciences*, vol. 1, no. 4, pp. 302–311, Apr. 2008, doi: 10.3844/ajeassp.2008.302.311.
- [21] L. Wei and P. Geng, “A review on natural gas/diesel dual fuel combustion, emissions and performance,” *Fuel processing technology*, vol. 142, pp. 264–278, 2016, doi: 10.1016/j.fuproc.2015.09.018.
- [22] Q. Dong, Y. Li, E. Song, C. Yao, L. Fan, and J. Sun, “The characteristic analysis of high-pressure gas jets for natural gas engine based on shock wave structure,” *Energy conversion and management*, vol. 149, pp. 26–38, 2017, doi: 10.1016/j.enconman.2017.06.015.
- [23] T. Rogers, P. Petersen, L. Koopmans, P. Lappas, and A. Boretti, “Structural characteristics of hydrogen and compressed natural gas fuel jets,” *International Journal of Hydrogen Energy*, vol. 40, no. 3, pp. 1584–1597, Jan. 2015, doi: 10.1016/j.ijhydene.2014.10.140.
- [24] W. Vera-Tudela, P. Kyrtatos, B. Schneider, K. Boulouchos, and M. Willmann, “An experimental study on the effects of needle dynamics on the penetration of a high-pressure methane jet,” *Fuel (Guildford)*, vol. 253, pp. 79–89, 2019, doi: 10.1016/j.fuel.2019.04.171.
- [25] E. Faghani, P. Kheirkhah, C. W. J. Mabson, G. McTaggart-Cowan, P. Kirchen, and S. Rogak, “Effect of Injection Strategies on Emissions from a Pilot-Ignited Direct-Injection Natural-Gas Engine- Part I: Late Post Injection,” presented at the WCX™ 17: SAE World Congress Experience, Mar. 2017, pp. 2017-01–0774. doi: 10.4271/2017-01-0774.
- [26] G. McTaggart-Cowan *et al.*, “Direct Injection of Natural Gas at up to 600 Bar in a Pilot-Ignited Heavy-Duty Engine,” *SAE International Journal of Engines*, vol. 8, Jan. 2015, doi: 10.4271/2015-01-0865.
- [27] X. Li, R. Zhou, W. Yao, and X. Fan, “Flow characteristic of highly underexpanded jets from various nozzle geometries,” *Applied thermal engineering*, vol. 125, pp. 240–253, 2017, doi: 10.1016/j.applthermaleng.2017.07.002.

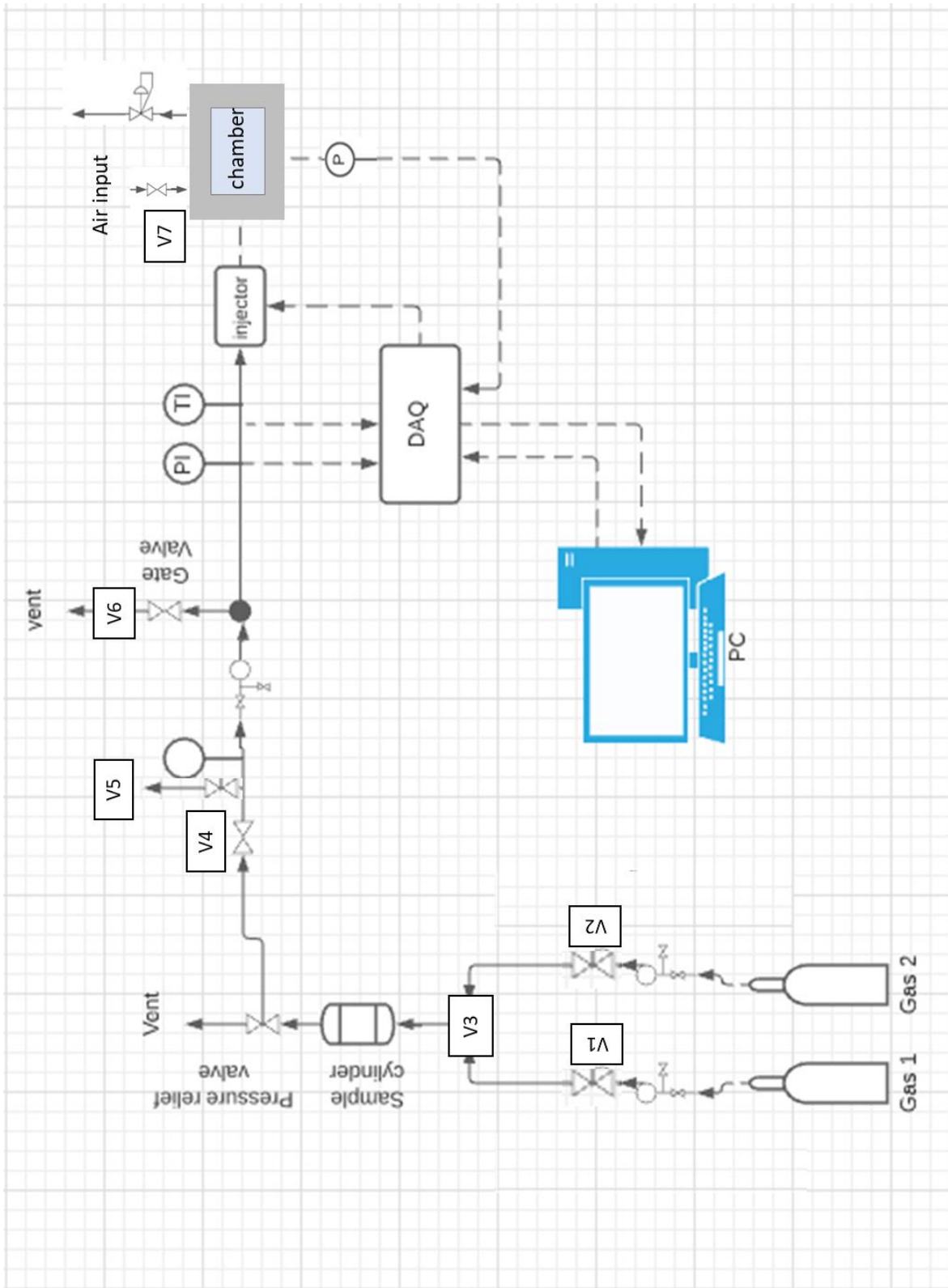
- [28] M. Banholzer, W. Vera-Tudela, C. Traxinger, M. Pfitzner, Y. Wright, and K. Boulouchos, "Numerical investigation of the flow characteristics of underexpanded methane jets," *Physics of Fluids*, vol. 31, no. 5, p. 056105, May 2019, doi: 10.1063/1.5092776.
- [29] A. Velikorodny and S. Kudriakov, "Numerical study of the near-field of highly underexpanded turbulent gas jets," *International Journal of Hydrogen Energy*, vol. 37, no. 22, pp. 17390–17399, Nov. 2012, doi: 10.1016/j.ijhydene.2012.05.142.
- [30] J. Yu, V. Vuorinen, O. Kaario, T. Sarjovaara, and M. Larmi, "Visualization and analysis of the characteristics of transitional underexpanded jets," *International Journal of Heat and Fluid Flow*, vol. 44, pp. 140–154, Dec. 2013, doi: 10.1016/j.ijheatfluidflow.2013.05.015.
- [31] A. Hamzehloo and P. G. Aleiferis, "Large eddy simulation of highly turbulent under-expanded hydrogen and methane jets for gaseous-fuelled internal combustion engines," *International Journal of Hydrogen Energy*, vol. 39, no. 36, pp. 21275–21296, Dec. 2014, doi: 10.1016/j.ijhydene.2014.10.016.
- [32] J. S. Turner, "The 'starting plume' in neutral surroundings," *J. Fluid Mech.*, vol. 13, no. 3, pp. 356–368, Jul. 1962, doi: 10.1017/S0022112062000762.
- [33] P. Ouellette and P. G. Hill, "Turbulent Transient Gas Injections," *Journal of fluids engineering*, vol. 122, no. 4, pp. 743–752, 2000, doi: 10.1115/1.1319845.
- [34] Ouellette, P, "Direct Injection of Natural Gas for Diesel Engine Fueling," Ph.D. Dissertation, University of British Columbia, Vancouver, BC, Canada, 1996.
- [35] P. G. Hill and P. Ouellette, "Transient Turbulent Gaseous Fuel Jets for Diesel Engines," *Journal of Fluids Engineering*, vol. 121, no. 1, pp. 93–101, Mar. 1999, doi: 10.1115/1.2822018.
- [36] J. Zhao, "Experimental investigation on the microscopic characteristics of underexpanded transient hydrogen jets," *international journal of hydrogen energy*, p. 9.
- [37] I. Erfan, I. Chitsaz, M. Ziabasharhagh, A. Hajjalimohammadi, and B. Fleck, "Injection characteristics of gaseous jet injected by a single-hole nozzle direct injector," *Fuel*, vol. 160, pp. 24–34, Nov. 2015, doi: 10.1016/j.fuel.2015.07.037.
- [38] M. R. A. Mansor, S. Nakao, K. Nakagami, M. Shioji, and A. Kato, "Ignition Characteristics of Hydrogen Jets in an Argon-Oxygen Atmosphere," presented at the SAE 2012 World Congress & Exhibition, Apr. 2012, pp. 2012-01–1312. doi: 10.4271/2012-01-1312.
- [39] A. Hajjalimohammadi, A. Abdullah, M. AghaMirsalim, and I. Chitsaz, "Experimental and Numerical Investigation on the macroscopic characteristics of the jet discharging from gaseous direct injector," *Journal of mechanical science and technology*, vol. 28, no. 2, pp. 773–781, 2014, doi: 10.1007/s12206-013-1142-3.
- [40] K. Pan and J. Wallace, "Numerical studies of the ignition characteristics of a high-pressure gas jet in compression-ignition engines with glow plug ignition assist: Part 1—Operating condition study," *International Journal of Engine Research*, vol. 18, p. 146808741769975, Apr. 2017, doi: 10.1177/1468087417699753.
- [41] G. HORN and M. W. THRING, "Angle of Spread of Free Jets," *Nature (London)*, vol. 178, no. 4526, pp. 205–206, 1956, doi: 10.1038/178205a0.
- [42] N. Kawaharada, L. Thimm, T. Dageförde, K. Gröger, H. Hansen, and F. Dinkelacker, "Approaches for Detailed Investigations on Transient Flow and Spray Characteristics during High Pressure Fuel Injection," *Applied sciences*, vol. 10, no. 12, pp. 4410–, 2020, doi: 10.3390/app10124410.
- [43] A. Hamzehloo and P. G. Aleiferis, "Numerical modelling of transient under-expanded jets under different ambient thermodynamic conditions with adaptive mesh

- refinement,” *The International journal of heat and fluid flow*, vol. 61, pp. 711–729, 2016, doi: 10.1016/j.ijheatfluidflow.2016.07.015.
- [44] J. Deng, H. Zhong, Y. Gong, X. Gong, and L. Li, “Studies on injection and mixing characteristics of high pressure hydrogen and oxygen jet in argon atmosphere,” *Fuel*, vol. 226, pp. 454–461, Aug. 2018, doi: 10.1016/j.fuel.2018.04.038.
- [45] T. Korakianitis, A. M. Namasivayam, and R. J. Crookes, “Natural-gas fueled spark-ignition (SI) and compression-ignition (CI) engine performance and emissions,” *Progress in Energy and Combustion Science*, vol. 37, no. 1, pp. 89–112, Feb. 2011, doi: 10.1016/j.pecs.2010.04.002.
- [46] G. A. Karim, “Combustion in Gas Fueled Compression: Ignition Engines of the Dual Fuel Type,” *Journal of Engineering for Gas Turbines and Power*, vol. 125, no. 3, pp. 827–836, Aug. 2003, doi: 10.1115/1.1581894.
- [47] H. Guo, B. Liko, L. Luque, and J. Littlejohns, “Combustion Performance and Unburned Hydrocarbon Emissions of a Natural Gas–Diesel Dual Fuel Engine at a Low Load Condition,” *Journal of Engineering for Gas Turbines and Power*, vol. 140, no. 11, p. 112801, Nov. 2018, doi: 10.1115/1.4039758.
- [48] G. McTaggart-Cowan, H. Jones, S. Rogak, W. Bushe, P. Hill, and S. Munshi, “The Effects of High-Pressure Injection on a Compression-Ignition, Direct Injection of Natural Gas Engine,” presented at the Journal of Engineering for Gas Turbines and Power, Jan. 2005, vol. 129. doi: 10.1115/ICEF2005-1213.
- [49] I. M. Gogolev and J. S. Wallace, “Performance and emissions of a compression-ignition direct-injected natural gas engine with shielded glow plug ignition assist,” *Energy Conversion and Management*, vol. 164, pp. 70–82, May 2018, doi: 10.1016/j.enconman.2018.02.071.
- [50] K. Pan and J. S. Wallace, “Influences of a new glow plug shield on natural gas combustion characteristics in direct-injection engines,” *Fuel*, vol. 294, p. 120401, Jun. 2021, doi: 10.1016/j.fuel.2021.120401.
- [51] G. McTaggart-Cowan, J. Huang, M. Turcios, A. Singh, and S. Munshi, “Evaluation of a Hot-Surface Ignition System for a Direct-Injection of Natural Gas Engine,” presented at the ASME 2018 Internal Combustion Engine Division Fall Technical Conference, Jan. 2019. doi: 10.1115/ICEF2018-9734.
- [52] G. P. McTaggart-Cowan, S. N. Rogak, S. R. Munshi, P. G. Hill, and W. K. Bushe, “The influence of fuel composition on a heavy-duty, natural-gas direct-injection engine,” *Fuel*, vol. 89, no. 3, pp. 752–759, Mar. 2010, doi: 10.1016/j.fuel.2009.10.007.
- [53] G. P. McTaggart-Cowan, H. L. Jones, S. N. Rogak, W. K. Bushe, P. G. Hill, and S. R. Munshi, “Direct-Injected Hydrogen-Methane Mixtures in a Heavy-Duty Compression Ignition Engine,” SAE International, Warrendale, PA, SAE Technical Paper 2006-01–0653, Apr. 2006. doi: 10.4271/2006-01-0653.
- [54] N. K. Frhan and A. B. Sapit, “Effect of Hydrogen Addition and Equivalence Ratio on Swirl Motion of Direct Ignition Engine,” *Indian journal of science and technology*, vol. 11, no. 46, pp. 1–9, 2017, doi: 10.17485/ijst/2018/v11i46/139328.
- [55] D. Nguyen Ngoc, H. Ishida, and M. Shioji, “Ignition Delay and Combustion Characteristics of Gaseous Fuel Jets,” *Journal of Engineering for Gas Turbines and Power-transactions of The Asme - J ENG GAS TURB POWER-T ASME*, vol. 132, Apr. 2010, doi: 10.1115/1.4000115.
- [56] R. Mével, J. Melguizo-Gavilanes, L. R. Boeck, and J. E. Shepherd, “Experimental and numerical study of the ignition of hydrogen-air mixtures by a localized stationary hot surface,” *The International journal of heat and fluid flow*, vol. 76, pp. 154–169, 2019, doi: 10.1016/j.ijheatfluidflow.2019.02.005.

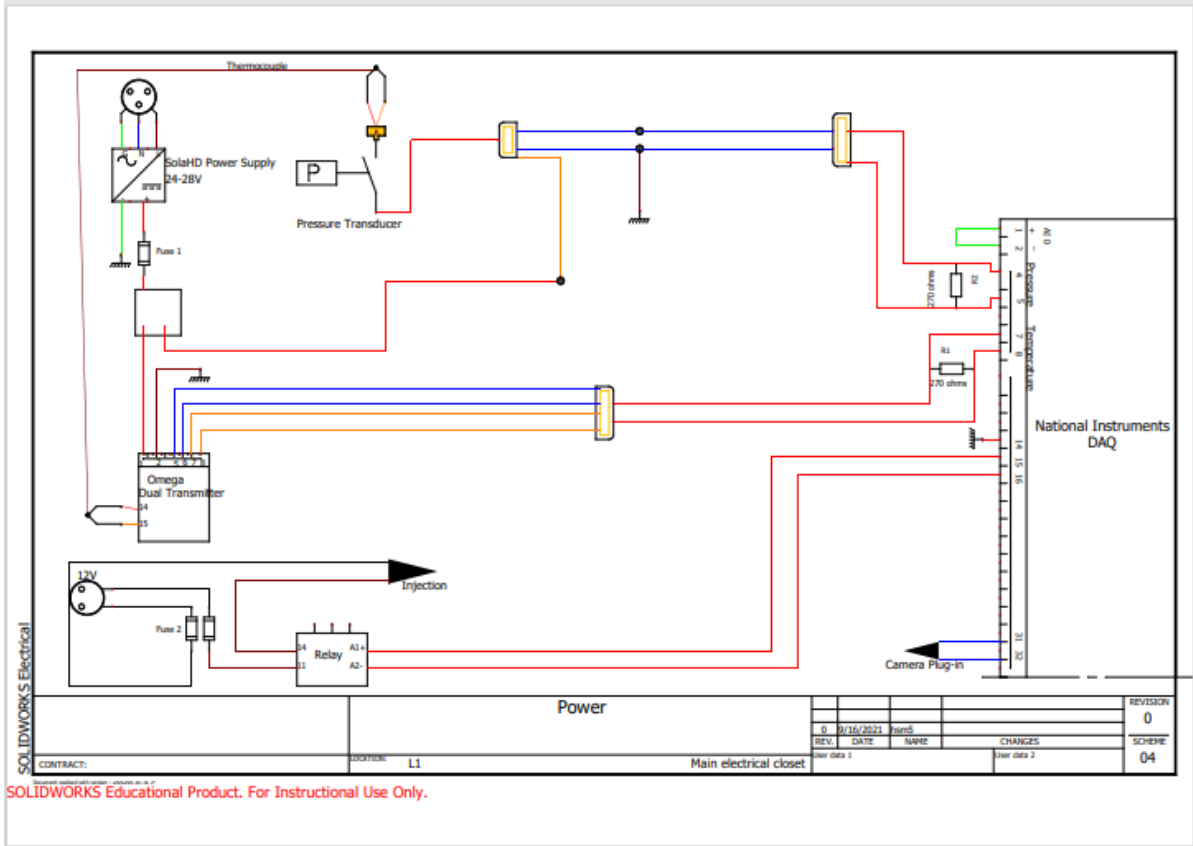
- [57] N. Wu, G. McTaggart-Cowan, W. K. Bushe, and M. H. Davy, "Effects of Hydrogen Addition on High-Pressure Nonpremixed Natural Gas Combustion," *Combustion Science and Technology*, vol. 183, pp. 20–42, 2010.
- [58] I. Gogolev and J. Wallace, "Study of Assisted Compression Ignition in a Direct Injected Natural Gas Engine," *Journal of Engineering for Gas Turbines and Power*, vol. 139, Jun. 2017, doi: 10.1115/1.4036968.
- [59] "Degradation of Silicon Nitride Glow Plugs in Various Environments Part 3: NGDI Engine - Oprea - 2012 - International Journal of Applied Ceramic Technology - Wiley Online Library." <https://ceramics.onlinelibrary.wiley.com/doi/abs/10.1111/j.1744-7402.2011.0202724.x> (accessed Sep. 09, 2022).
- [60] L. Allocca, A. Montanaro, G. Meccariello, and F. Duronio, "Under-Expanded Gaseous Jets Characterization for Application in Direct Injection Engines: Experimental and Numerical Approach," *SAE Technical Paper Series*, 4AD, doi: 10.4271/2020-01-0325.
- [61] D. Sankesh and P. Lappas, "An experimental and numerical study of natural gas jets for direct injection internal combustion engines," *Fuel*, vol. 263, p. 116745, 2020, doi: <https://doi.org/10.1016/j.fuel.2019.116745>.
- [62] J. Tian, Z. Cui, Z. Ren, H. Tian, and W. Long, "Experimental study on jet ignition and combustion processes of natural gas," *Fuel*, vol. 262, p. 116467, 2020, doi: <https://doi.org/10.1016/j.fuel.2019.116467>.
- [63] A. Hamzehloo and P. G. Aleiferis, "LES and RANS modelling of under-expanded jets with application to gaseous fuel direct injection for advanced propulsion systems," *International Journal of Heat and Fluid Flow*, vol. 76, pp. 309–334, 2019, doi: <https://doi.org/10.1016/j.ijheatfluidflow.2019.01.017>.
- [64] M. Banholzer, W. Vera-Tudela, C. Traxinger, M. Pfitzner, Y. Wright, and K. Boulouchos, "Numerical investigation of the flow characteristics of underexpanded methane jets," *Physics of Fluids*, vol. 31, no. 5, p. 56105, May 2019, doi: 10.1063/1.5092776.
- [65] M. Banholzer, M. Banholzer, W. Vera-Tudela, C. Traxinger, and M. Pfitzner, "Numerical investigation of the flow characteristics of underexpanded methane jets," *Physics of fluids (1994)*, vol. 31, no. 5, Jan. 5AD, doi: 10.1063/1.5092776.
- [66] M. E. Feyz, M. R. Nalim, V. R. Hasti, and J. P. Gore, "Modeling and Analytical Solution of Near-Field Entrainment in Suddenly Started Turbulent Jets," *AIAA Journal*, vol. 57, no. 5, pp. 1877–1884, Feb. 2019, doi: 10.2514/1.J057612.
- [67] W. Vera-Tudela, W. Vera-Tudela, P. Kyrtatos, B. Schneider, and K. Boulouchos, "An experimental study on the effects of needle dynamics on the penetration of a high-pressure methane jet," *Fuel (Guildford)*, vol. 253, pp. 79–89, Jan. 10AD, doi: 10.1016/j.fuel.2019.04.171.
- [68] D. Sankesh, P. Petersen, and P. Lappas, "Flow characteristics of natural-gas from an outward-opening nozzle for direct injection engines," *Fuel*, vol. 218, Jan. 2018, doi: 10.1016/j.fuel.2018.01.009.
- [69] A. Hamzehloo and P. G. Aleiferis, "Gas dynamics and flow characteristics of highly turbulent under-expanded hydrogen and methane jets under various nozzle pressure ratios and ambient pressures," *International Journal of Hydrogen Energy*, vol. 41, no. 15, pp. 6544–6566, 2016, doi: <https://doi.org/10.1016/j.ijhydene.2016.02.017>.
- [70] A. Hamzehloo, A. Hamzehloo, and P. G. Aleiferis, "Numerical modelling of transient under-expanded jets under different ambient thermodynamic conditions with adaptive mesh refinement," *The International journal of heat and fluid flow*, vol. 61, pp. 711–729, Jan. 10AD, doi: 10.1016/j.ijheatfluidflow.2016.07.015.
- [71] A. Twellmeyer, A. TWELLMAYER, F. KÖPPEL, and B. WEIGAND, "A NOVEL CFD APPROACH FOR MODELLING THE HIGH-PRESSURE DIRECT INJECTION AND

- MIXTURE FORMATION IN A SPARK-IGNITED CNG ENGINE,” *International journal of computational methods and experimental measurements*, vol. 4, no. 4, pp. 424–433, 11AD, doi: 10.2495/CMEM-V4-N4-424-433.
- [72] E. Franquet, V. Perrier, S. Gibout, and P. Bruel, “Free underexpanded jets in a quiescent medium: A review,” *Progress in Aerospace Sciences*, vol. 77, pp. 25–53, 2015, doi: <https://doi.org/10.1016/j.paerosci.2015.06.006>.
- [73] V. Vuorinen, V. Vuorinen, A. Wehrfritz, C. Duwig, and B. J. Boersma, “Large-eddy simulation on the effect of injection pressure and density on fuel jet mixing in gas engines,” *Fuel (Guildford)*, vol. 130, pp. 241–250, 8AD, doi: 10.1016/j.fuel.2014.04.045.
- [74] V. Vuorinen *et al.*, “Large-eddy simulation of highly underexpanded transient gas jets,” *Physics of Fluids*, vol. 25, no. 1, p. 16101, Jan. 2013, doi: 10.1063/1.4772192.
- [75] J. Yu, V. Vuorinen, O. Kaario, and T. Sarjojaara, “Visualization and analysis of the characteristics of transitional underexpanded jets,” *The International journal of heat and fluid flow*, vol. 44, pp. 140–154, Jan. 12AD, doi: 10.1016/j.ijheatfluidflow.2013.05.015.
- [76] R. Sierens, S. Verhelst, R. Scarcelli, and N. S. Matthias, “Update on the Progress of Hydrogen-Fueled Internal Combustion Engines,” *Renewable Hydrogen Technologies: Production, Purification, Storage, Applications and Safety*. Elsevier Science [Imprint], pp. 381–400, Jan. 1AD.
- [77] G. S. Settles, *Schlieren and Shadowgraph Techniques*. Berlin, Heidelberg: Springer, 2001. doi: 10.1007/978-3-642-56640-0.
- [78] R.-H. Chen, Ed., “Steady One-Dimensional Flows in Channels,” in *Foundations of Gas Dynamics*, Cambridge: Cambridge University Press, 2017, pp. 132–154. doi: 10.1017/9781316014288.006.
- [79] U. Maas and J. Warnatz, “Ignition processes in hydrogen–oxygen mixtures,” *Combustion and Flame*, vol. 74, no. 1, pp. 53–69, Oct. 1988, doi: 10.1016/0010-2180(88)90086-7.

Appendix A: P&ID of the system



Appendix B: Electrical Drawing



SOLIDWORKS Educational Product. For Instructional Use Only.

Appendix C: MATLAB Code

```
clear all;clc; close all;
%initialization;
dq = daq("ni");

addoutput(dq, "Dev1", "ao0", "Voltage");
addoutput(dq, "Dev1", "ao1", "Voltage");

ch_out = dq.Channels(1:2);
ch_out(1).Name = "Dev1_1_out";
ch_out(2).Name = "Dev1_2_out";

addinput(dq, 'Dev1', 'ai0', 'Voltage');
addinput(dq, 'Dev1', 'ai1', 'Voltage');
addinput(dq, 'Dev1', 'ai2', 'Voltage');
addinput(dq, 'Dev1', 'ai3', 'Voltage');
addinput(dq, 'Dev1', 'ai4', 'Voltage');
addinput(dq, 'Dev1', 'ai5', 'Voltage');

ch_in = dq.Channels(3:8);
ch_in(1).Name = "Dev1_1_in";
ch_in(2).Name = "Dev1_2_in";
ch_in(3).Name = "Dev1_3_in";
ch_in(4).Name = "Dev1_4_in";
ch_in(5).Name = "Dev1_5_in";
ch_in(6).Name = "Dev1_6_in";

ch_in(1).TerminalConfig = 'Differential';
ch_in(2).TerminalConfig = 'Differential';
ch_in(3).TerminalConfig = 'Differential';
ch_in(4).TerminalConfig = 'Differential';
ch_in(5).TerminalConfig = 'Differential';
ch_in(6).TerminalConfig = 'Differential';

fig = uifigure;
uialert(fig,'Make sure the valve 4 is closed'," .', ...
        'Program Information','Icon','info','CloseFcn','uiresume(fig)')

uiwait(fig)
close (fig)
%% Parameteres definitions

% DAQ parameters
rate = 100000;
dq.Rate = rate;
Camera_ON = 1; % 0 camera OFF, 1 camera ON
% Measurements parameters
Number_of_Measurements = 1; % total number of time injection
happens and sensor data capture
Pause_between_each_Measurements= 15; % in millisecond
Measurement_Data=cell(Number_of_Measurements,2);
```

```

Injection_Duration= 0.0025;           % in second
Sensor_read_Duration= 0.1;           % in second
Injection_delay = 0.1; %in seconds, delay from start of run to
injection trigger

Dwell = 0; %in \second
PulseTwo = Injection_Duration*0; % in millisecond

%Measurement_Duration=
max(Injection_Duration,Sensor_read_Duration)+0.1;
Measurement_Duration= max(Injection_Duration,Sensor_read_Duration)+0.1;
DAQ_sensor_injector_output = zeros(Measurement_Duration*rate,1);
DAQ_sensor_injector_output(Injection_delay*rate:Injection_Duration*rate
+Injection_delay*rate,1)=5.01;
%DAQ_sensor_injector_output(end-500:end,1)=0;
DAQ_sensor_injector_output(Injection_Duration*rate+Injection_delay*rate
:Injection_Duration*rate+Injection_delay*rate+Dwell*rate,1)=0;
DAQ_sensor_injector_output(Injection_Duration*rate+Injection_delay*rate
+Dwell*rate:Injection_Duration*rate+Injection_delay*rate+Dwell*rate+Pul
seTwo*rate,1)=5.01;
DAQ_sensor_injector_output(Injection_Duration*rate+Injection_delay*rate
+Dwell*rate+PulseTwo*rate:end-1,1)=0;
DAQ_sensor_injector_output(end-1:end,1)=0;

if (Camera_ON == 1)
    DAQ_Camera_output = DAQ_sensor_injector_output;
else
    DAQ_Camera_output = zeros(Measurement_Duration*rate,1);
end

for M=1:Number_of_Measurements

    Measurement_Data{M,1}= readwrite(dq, [DAQ_sensor_injector_output
DAQ_Camera_output]);

    Measurement_Data{M,1}.Dev1_1_in =
Measurement_Data{M,1}.Dev1_1_in*1.8618;
    Measurement_Data{M,1}.Dev1_2_in =
Measurement_Data{M,1}.Dev1_2_in*34.722-37.5;
    Measurement_Data{M,1}.Dev1_3_in =
Measurement_Data{M,1}.Dev1_3_in*23.163 - 25.124;
    Measurement_Data{M,1}.Dev1_4_in =
Measurement_Data{M,1}.Dev1_4_in*347.22-375;
    Measurement_Data{M,1}.Dev1_5_in =
Measurement_Data{M,1}.Dev1_5_in*139.2-150;
    Measurement_Data{M,1}.Dev1_6_in =
Measurement_Data{M,1}.Dev1_6_in*0.2175;

    pause(Pause_between_each_Measurements/1000); % in s
end

%%file_name = sprintf('Capture_Data_%s.mat',datestr(now));
%%save (file_name, 'Measurement_Data')

```

```

for i=1: Number_of_Measurements
    figure
    subplot(6,1,1);
    plot(Measurement_Data{i,1}.Time,Measurement_Data{i,1}.Dev1_1_in);
    title("Measurement No. " +i+ " Force Sensor");
    xlabel('Time');
    ylabel('Force (psi)');

    subplot(6,1,2);
    plot(Measurement_Data{i,1}.Time,Measurement_Data{i,1}.Dev1_2_in);
    xL=xlim;
    yL=ylim;
    hold on
    yline(mean(Measurement_Data{i,1}.Dev1_2_in), 'r', 'LineWidth', 2);
    str=["Mean = " num2str(mean(Measurement_Data{i,1}.Dev1_2_in))];

text(0.99*xL(2),0.99*yL(2),str, 'HorizontalAlignment', 'right', 'VerticalA
lignment', 'top');
    title("Measurement No. " +i+ " Rail Pressure Sensor");
    xlabel('Time');
    ylabel('Pressure (psi)');

    subplot(6,1,3);
    plot(Measurement_Data{i,1}.Time,Measurement_Data{i,1}.Dev1_3_in);
    hold on
    xL=xlim;
    yL=ylim;
    yline(mean(Measurement_Data{i,1}.Dev1_3_in), 'r', 'LineWidth', 2);
    str=["Mean = " num2str(mean(Measurement_Data{i,1}.Dev1_3_in))];

text(0.99*xL(2),0.99*yL(2),str, 'HorizontalAlignment', 'right', 'VerticalA
lignment', 'top');
    title("Measurement No. " +i+ " Temprature Sensor");
    xlabel('Time');
    ylabel('Temprature (C)');

    subplot(6,1,4);
    plot (Measurement_Data{i,1}.Time,Measurement_Data{i,1}.Dev1_4_in);
    hold on
    xL=xlim;
    yL=ylim;
    yline(mean(Measurement_Data{i,1}.Dev1_4_in), 'r', 'LineWidth', 2);
    str=["Mean = " num2str(mean(Measurement_Data{i,1}.Dev1_4_in))];

text(0.99*xL(2),0.99*yL(2),str, 'HorizontalAlignment', 'right', 'VerticalA
lignment', 'top');
    title("Measurement No. " +i+ " 4th Sensor");
    xlabel('Time');
    ylabel('Temprature (C)');

    subplot(6,1,5);
    plot (Measurement_Data{i,1}.Time,Measurement_Data{i,1}.Dev1_5_in);
    hold on
    xL=xlim;
    yL=ylim;
    yline(mean(Measurement_Data{i,1}.Dev1_6_in), 'r', 'LineWidth', 2);

```

```

    str=["Mean = " num2str(mean(Measurement_Data{i,1}.Dev1_5_in))];
text(0.99*xL(2),0.99*yL(2),str,'HorizontalAlignment','right','VerticalA
lignment','top');
    title("Measurment No. " +i+ " 5th Sensor");
    xlabel('Time');
    ylabel('Temprature (C)');

hold on
subplot(6,1,6);

plot (Measurement_Data{i,1}.Time,Measurement_Data{i,1}.Dev1_6_in);
xL=xlim;
yL=yylim;
yline(mean(Measurement_Data{i,1}.Dev1_6_in),'r','LineWidth',2);
str=["Mean = " num2str(mean(Measurement_Data{i,1}.Dev1_6_in))];

text(0.99*xL(2),0.99*yL(2),str,'HorizontalAlignment','right','VerticalA
lignment','top');
    title("Measurment No. " +i+ " flow meter");
    xlabel('Time');
    ylabel('idk');

end
autoArrangeFigures();

```